encl. to 10/7/86 ltr.
rec'd 10/10/86 to
Johnson from Prestholt

THE EFFECTS OF WELDING AND CASTING PROCESS VARIABLES ON THE MICROSTRUCTURE AND PROPERTIES OF HIGH LEVEL NUCLEAR WASTE OVERPACK CONTAINERS

by

Thomas R. Muth

Department of Metallurgical Engineering
Colorado School of Mines
Golden, Colorado 80401

T-3270

THE EFFECTS OF WELDING AND CASTING PROCESS VARIABLES ON THE MICROSTRUCTURE AND PROPERTIES OF HIGH LEVEL NUCLEAR WASTE OVERPACK CONTAINERS

by

Thomas R. Muth

T-3270

A thesis sumbitted to the Faculty and the Board of Trustees of the Colorado School of Mines in partial fulfillment of the requirements for the degree of Master of Science (Metallurgical Engineering).

Golden, Colorado

Date: _____

Signed: _____

Thomas R. Muth

Student

Approved: _____

Dr. Robert H. Frost

Thesis Advisor

Golden, Colorado

Date: _____

_____

Dr. William D. Copeland

Department Head

Metallurgical Engineering

ABSTRACT

The objective of this research was to investigate the influence of manufacturing processes on the mechanical and corrosion behavior of high level nuclear waste overpack containers. Since microstructure determines the mechanical and corrosive response of the container, the brunt of this investigation is directed toward microstructural control through processing.

Primary production techniques; wrought processing, centrifugal casting, and static casting, were evaluated through literature with the conclusion that centrifugal casting was the best available manufacturing technique to produce cylindrical, heavy walled, steel overpack containers. The material chosen for this investigation fell within the ASTM A216 grade WCA specification, (1) cast steel suitable for welding. The casting process variables that affected the steel's microstructure were; cleanliness of the molten metal, alloy content, tapping temperature, pouring temperatures, deoxidation practice, furnace and ladle conditions, and solidification time. Submerged arc welding of cast steel with alloy and cleanliness variations within the above specification showed significant microstructural differences dependent

on initial casting variables. Submerged arc weld heat affected zone simulation studies showed that the Gleeble 1500 thermomechanical testing unit could be used as a tool to generate specimens that duplicate the microstructure of specific regions in the heat affected zone. Through Gleeble simulation and actual weld, sectioning, it was determined that the casting process variables only play a significant role in final microstructure when peak temperatures reach above 1100°C in the weld heat affected zone. The influence these variables had in controlling austenite decomposition products showed that high manganese to oxygen ratios led to bainite in the heat affected zone where peak temperatures exceeded 1100°C and that low manganese to oxygen ratios led to ferrite/pearlite in the same heat affected zone region. The increase in nucleation sites was determined to be the reason for these microstructural differences and the initial melting and casting processes variables were directly attributed to controlling the nucleation sites for austenite decomposition.

The final austenite decomposition products control the mechanical and corrosion performance of the overpack containers and thus must be controlled and predicted to insure against premature failure. This thesis is a

document that demonstrates how initial casting processing can control final overpack microstructure through alloy content and cleanliness variations using both analytical and experimental techniques.

TABLE OF CONTENTS

LIST OF FIGURES

LIST OF TABLES

ACKNOWLEDGEMENTS

This thesis was made possible by a number of individuals and organizations, whose assistance and support will not be forgotten, as it was through their help that I had the opportunity to expand my knowledge.

I would like to thank the Nuclear Regulatory Commission and Manufacturing Sciences Corporation for financial and technical support to the CSM Center for Welding Research.

I would like to thank my thesis advisor, Dr. Robert H. Frost, for his continual support and guidance. I would also like to thank the other members of my committee, Dr. David L. Olson and Dr. Alan L. Liby for their support and contributions.

Thanks go to undergraduates Phillip Glynn, Stewart Robertson, Jeff Epstein, and Christopher Roll who assisted me in photography, metallography, welding and casting.

I would like to thank all the Metallurgy graduate students and staff, especially Joel Self, Shing Ho Wang, Tim Vaughn, Andy Hunt, Bob Yorgason, Diane Magner, and Mark Nordin as well as Dr. G. P. Martins, Dr. D. K.

Matlock, Dr. G. R. Edwards, Dr. W. D. Copeland, and Dr. Elliot Brown. Their knowledge, understanding and assistance was outstanding.

I would like to thank my parents, Jim and Ellen, as well as my brother Jim, and sister Mary for being a part of my education. Their financial support, inspiration, sacrifice, and companionship allowed me the opportunity to better myself.

I would like to express my deepest gratitude to my wife, Andrea, whose sacrifices, companionship and emotional support cannot be put to paper, but are with me always.

1. INTRODUCTION

This research was designed to provide the Nuclear Regulatory Commission (NRC) with data useful for the purpose of evaluating options available to the Department of Energy (DOE) for manufacturing high level nuclear waste containers. The material chosen, through verbal communication with the NRC was cast steel within the ASTM-A216 grade WCA specification (1). This steel can be expected to show a wide variation in microstructure as a result of differences in alloy chemistry and cleanliness, initial solidification processing, welding, and thermal processing during fabrication. Changes in manufacturing processes will have a marked effect on the mechanical and corrosion behavior of the waste containers. Each manufacturing process will yield a unique microstructure and this microstructure will be the key to container performance. This research provides both an analytical and experimental evaluation of the casting and welding process variables involved in waste container fabrication.

1.1 BACKGROUND ON MANUFACTURING TECHNIQUES

An evaluation of possible manufacturing processes to produce heavy walled steel overpack containers was completed prior to any experimental work. The various overpack container designs are shown in Appendix A. The cylindrical cask was deemed the most likely candidate, and as such wrought processing, static casting and centrifugal casting were chosen as the most likely fabrication means. The overpack containers must be remotely sealed by weld closure after placement of the waste to avoid human radiation exposure. An evaluation of the possible weld closure techniques: flux cored arc welding (FCAW); gas metal arc welding (GMAW); submerged arc welding (SAW); and electroslag welding (ESW) as well as the aforementioned fabrication techniques were evaluated to determine the best manufacturing technique to produce cylindrical, heavy walled, steel overpack containers.

Forging, ring rolling, an piercing are viable wrought processes that are capable of producing heavy walled cylinders; however, they require a large ingot or casting for starting material (2). The initial survey of

possible manufacturing methods concluded that wrought processing would be costly and that there was some question as to the forging capacity in the continental United States. For these reasons, wrought processing was not considered in the present study.

The processes available for cast overpack container production include static casting in sand or metal molds and centrifugal casting.

A static casting of the dimensions of the overpack container must be pit molded. This technique will yield several significant alterations in microstructure compared to a wrought product of the same dimensions. The solidification time is long and may be as much as 30 hours (3). This solidifaction time will yield a secondary dendrite arm spacing of 1000 microns which will be detrimental to mechanical performance because of the large amounts of microsegregation and macrosegregation associated with coarse, slowly solidified structures.

The process variables for the static casting of large heavy walled cylinders include: feeding, risering, core bouyancy, shake-out time, molding time and clean-up procedure. For large chunky steel castings it can be expected that 40 to 50 percent of the total tonnage cast

will be gates, runners and risers (4). This low yield is a tremendous expense. The casting must be bottom poured to prevent oxidation, splashing and cold shuts (5) and the feeding systems must be pressurized to insure uniform feeding and short pouring times. A riser calculation for a cylinder of the design specifications taken from Woldauer (3) is shown in Appendix B. Figure 1 shows the casting as it should look in the as-cast condition.

Corebouyancy will be a major factor in determining the reinforcement of the central core and the type of sand binder used to achieve the required core strengths. The force on the core is 16000 pounds (6) and requires the use of reinforcing bars to prevent core distortion, and the welding of the reinforcing bars to an external structure to prevent core shift. These procedures are time consuming with the result that pit molding is labor intensive. In addition to long molding times, the shake out times can be as long as several weeks. The cleaning procedures after shake-out become costly as the risers shown in Figure 1 must be removed, and the surface must be cleaned by shot blasting or grinding. Weld repair to take care of blow hole porosity or shrinkage porosity and

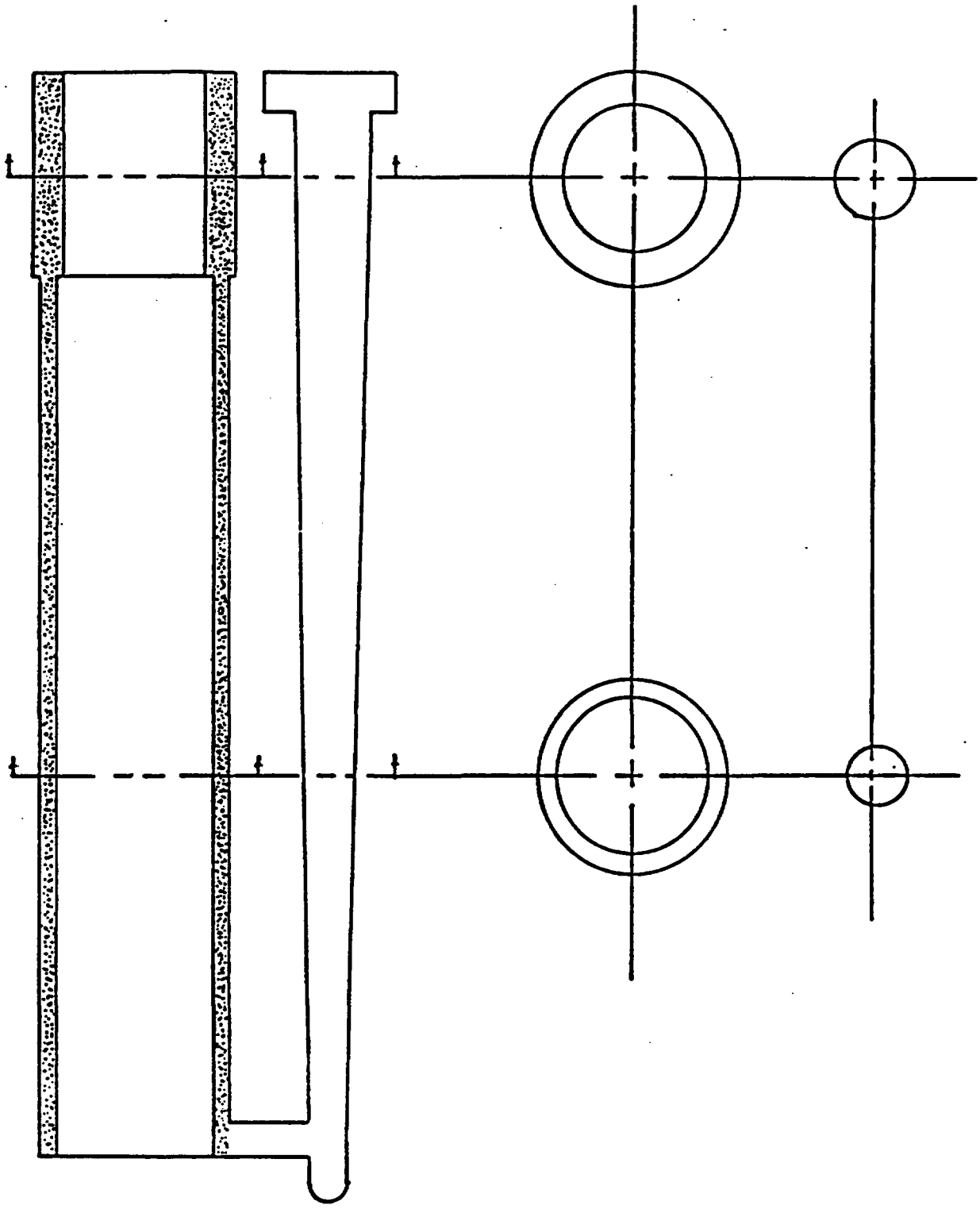

Figure 1. A typical static casting of the dimensions of the overpack container showing the riser.

non-destructive testing to provide radiographic quality is expected to be costly as well.

Centrifugal casting offers significant benefits for the production of cast overpack containers. The metal is poured into a cylindrical metal mold which is rotating at speeds of up to 2,000 rpm. The centrifugal force holds the metal against the wall while solidification proceeds. This enhances thermal contact between the surface of the casting and the mold wall, and provides a significant feeding force to prevent the development of porosity (7). Short castings are poured with the axis of the mold vertical. In this case the centrifugal force causes the molten metal to flow up along the mold wall. Long castings are poured with the mold axis horizontal, with one of the following techniques: the Watertown method, the Delavaud method, or the German process (8).

The Watertown method uses a heavy cast iron chill mold which is coated with a refractory mold wash and spun at 1300 to 2000 rpm. When the mold is at speed, a weighed amount of metal is poured into a pouring basin equipped with a short spout at the near end of the mold. The rate of entry into the mold is synchronized with spinning speed by regulating the spout diameter so that

molten metal will be distributed evenly and without tearing the solidified, but hot, shell. Pressure is applied to the far end shortly after solidification to prevent mold restraint, and consequently tearing as the tube contracts lengthwise in the mold (8). See Figure 2 for diagram.

The Delavaud method uses a thin walled, water cooled metal mold which is mounted on tracks and inclined at a slight angle to the horizontal. A pouring trough is extended into the spinning mold and metal is deposited in a helix from the farthest end of the trough as the spinning mold is retracted (8).

The German process, instead of using a mold wash, uses a fine sand deposited from a long trough over the mold surface. The mold is cast iron and spray cooled. The thermal barrier provided by the sand reduces heat shock, lessens checking of the mold surface, and prevents surface laps on castings caused by premature freezing (8).

The advantages of centrifugal casting for the production of ferrous tubular products include: a large increase in yield as compared with static casting techniques which require a riser, the elimination of

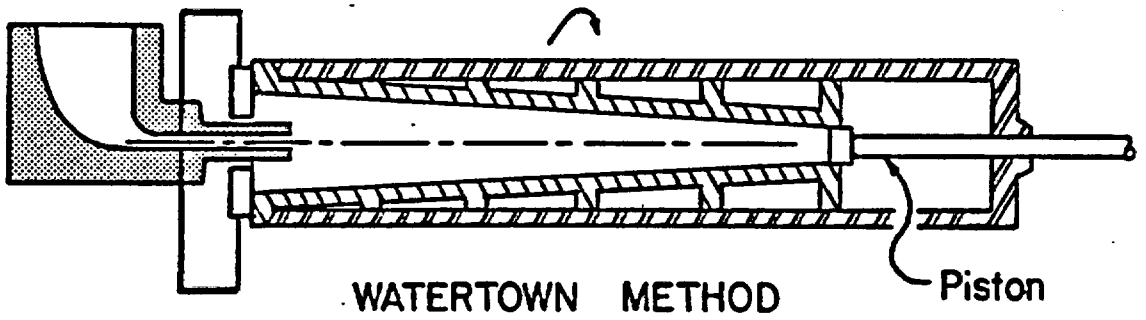

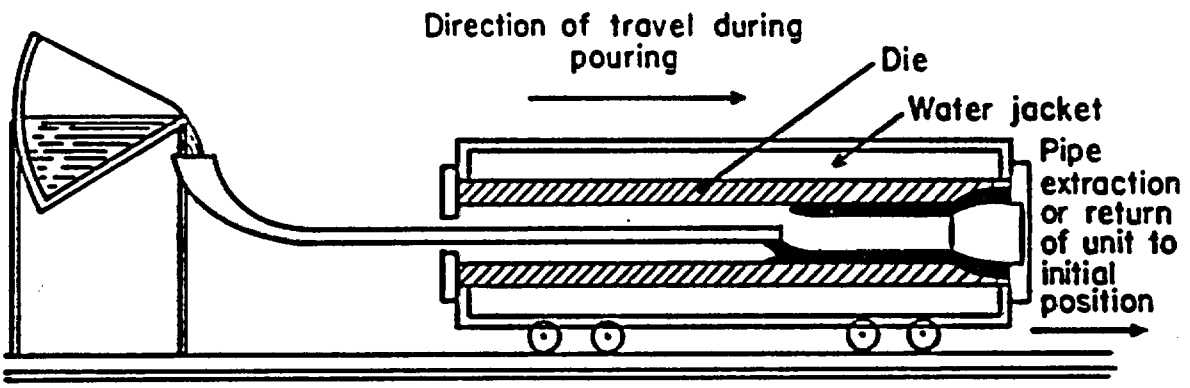

DeLAVAUD METHOD

Figure 2. Schematic representation of the Watertown and Delavoud methods for centrifugal casting in the horizontal position (8).

cores and the requirement of costly and time consuming pit molding techniques, the segregation of nonmetallic inclusions and slag to the inside surface of the casting, the development of a hollow cavity along the axis of the casting, and refinement of the solidifacation structure. The metal is forced out against the mold with a force of up to 200 g's (7). This provides an increase in the feeding force of two orders of magnitude over static castings; slag and non-metallic inclusions are forced to the center by the centrifuging action; the nucleation of gas bubbles and blow holes is suppressed by the high pressures; and a hole is left down the center of the casting.

The solidification structure in centrifugally cast steels is significantly more refined than a steel of the same section thickness which is statically cast. All of the commercially available centrifugal casting techniques involve a metal (grey iron, steel or copper) mold which may be water cooled. This significantly decreases the solidification time over statically cast cylinders. With the highly conductive mold metal interface more nuclei become active as sites for primary solidification. Since the number of grains depends on a competition between the

rate of nucleation and the rate of growth a centrifugally cast vessel will have a smaller grain size than the statically cast vessel (9).

After analysis of the various casting and forging processes, it is concluded that centrifugal casting is the technique best suited for the production of cylindrical high level nuclear waste overpack containers.

1.2 MELTING CONSIDERATIONS

In any manufacturing process which requires molten metal as an initial material, melting procedures are critical to the reproducibility of the steel. Melt logs and charge calculations must be detailed enough to trouble shoot any problems, or to duplicate successful heats. The critical documentation includes: the type and composition of scrap, melting stock and alloy additions; a melt log which includes the times and temperatures at which alloys were added and melting operations carried out; furnace and ladle conditions; the tapping time and temperature; and any irregular conditions that exist during the progress of the heat.

Appendix C provides the standard practice for the melting of carbon and low alloy steels by air induction melting.

In order to be able to reproduce a successful heat the charge calculation must have the expected losses incorporated into it. To keep those losses consistent, all additions must be made at the same temperature, and tapping intervals and pouring times must be documented.

The cleanliness of a steel can be controlled by knowing the scrap and bar analysis, and by using an appropriate slag or ladle refining technique (e.g. AOD). Tramp elements that are rarely analyzed for are cobalt, tin, antimony, lead, and arsenic. These elements are detrimental to mechanical and corrosive performance of steel and can be avoided by monitoring scrap and bar.

The influence of alloy composition and cleanliness was studied using three alloy compositions within the ASTM A-216 grade WCA specification for carbon steel castings which are suitable for welding. The target alloys, A, B and C are shown in Table I. The manganese, silicon and oxygen contents were varied to change the hardenability, cleanliness, and nature of the deoxidation product.

Table I. Target chemical compositions (weight percent) of alloys used to study the effects of alloy content and cleanliness.

Alloy	%C	%Si	%Mn	%O	%S	%P	%Al	Mn/O
A	0.18	0.10	0.50	0.020	0.01	0.02	0.05	25
B	0.18	0.25	1.00	0.007	0.01	0.02	0.05	145
C	0.18	0.25	1.00	0.007	0.045	0.02	0.05	145

The silicon and manganese levels influence the state of deoxidation, and the ratio of silicon to manganese determines the nature of the deoxidation product. The ratio of the manganese to oxygen content influences hardenability through alloy content and cleanliness (2). Figure 3 shows the influence of silicon and manganese additions on the dissolved oxygen content for a steel with an initial oxygen content of 0.1 weight percent (1000 ppm). Additions of 0.1 weight percent silicon and 0.50 weight percent manganese reduce the oxygen level to 0.02 weight percent (200 ppm), and leave 0.05 weight percent silicon and 0.4 weight percent manganese in solution after deoxidation. The additions of 0.25 weight percent silicon and 1.00 weight percent manganese reduce the dissolved oxygen content to about 0.008 weight percent (80 ppm) and leave 0.2 weight percent silicon and 0.9 weight percent manganese in solution after deoxidation. Figure 4 shows the influence of the silicon to manganese ratio on the nature of the deoxidation product (2). For the silicon and manganese charges given in Table I the deoxidation product is molten manganese silicate at steel making temperatures of 1600°C.

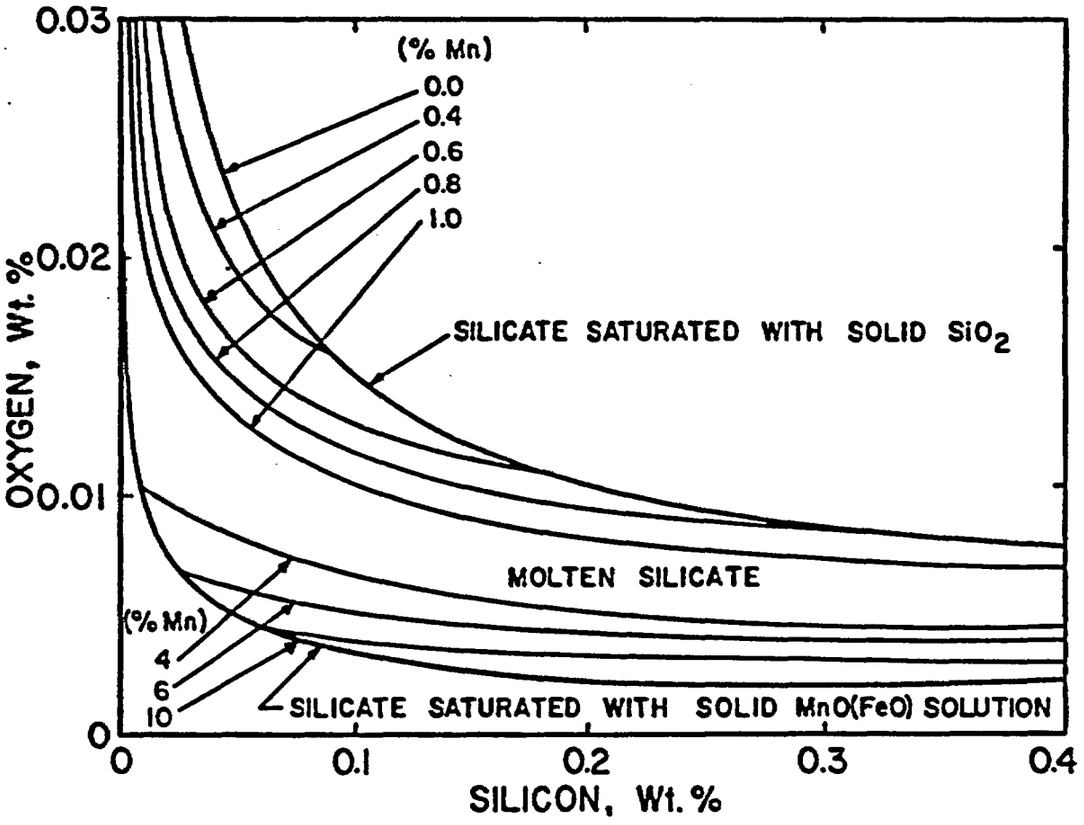

Figure 3. Residual oxygen in iron at 1600°C related to the percent silicon and percent manganese added to deoxidize steel containing initially 0.10 weight percent oxygen (2).

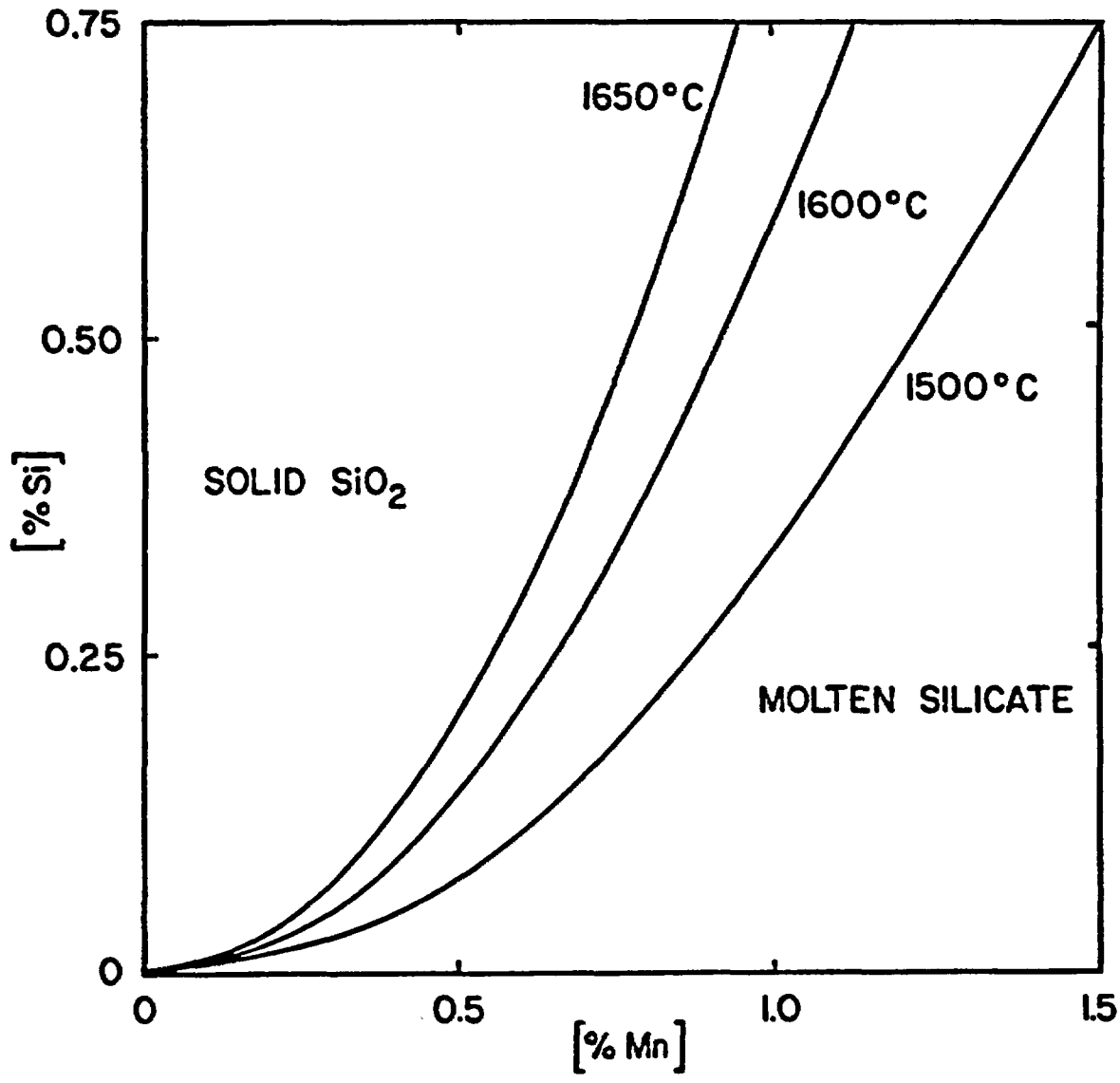

Figure 4. Concentrations of silicon and manganese in iron in equilibrium with silica-saturated manganese silicate melts (2).

Alloy A of Table I has a low manganese to oxygen ratio to reduce hardenability and increase the oxide inclusion content. Alloy B has a high manganese to oxygen ratio to provide high hardenability and limit the oxide inclusion content. Alloy C has the same high manganese to oxygen ratio as Alloy B plus the addition of 0.045 weight percent sulfur to investigate the influence of sulfide inclusions on alloy microstructure. The ASTM A-216 grade WCA specification for carbon steel castings allows for some residual elements, but these were kept to trace amounts to eliminate any secondary effects that may be caused by residual impurities.

1.3 WELDING BACKGROUND

The overpack containers, by design, will have a top and bottom welded on, to seal them for transportation and burial. The bottom of the overpack can be welded on by any of the following techniques: submerged arc welding, gas metal arc welding, electroslag welding, or flux cored arc welding. Nuclear waste will be placed into the container after the bottom is welded on. At that point,

handling must be remote, and an automatic welding apparatus must be employed to seal the top.

Each of the aforementioned welding processes has a different energy input and, as such, they generate a different heat affected zone (HAZ) thermal experience, resulting in a unique microstructure.

Several options are available for the joint design of the top and bottom closure. The AWS structural welding code designates these possibilities (11). Edge preparation should also be considered when choosing a joint design and a welding process.

Submerged arc welding is a process noted for use of high welding currents and high deposition rates. The process uses a bare metal electrode covered by a blanket of granular, fuseable flux. Filler metal is obtained from the electrode and/or supplementary welding rod. The electrode is advanced in the direction of welding and mechanically fed into the arc while flux is steadily added. Steady state welding requires that the electrode is melted at the same rate it is being fed into the arc. Electrode melting is current related and arc length is voltage related. Therefore the welding system is capable

of continuously correcting a voltage change with either a current or a feed rate change (12).

The welding current is between 400 and 1500 amperes for submerged arc processes, and optimum deposition rates have a current density greater than 40,000 A/in2 (620 A/mm2). The deposition rates for submerged arc welding range between 27 and 45 kg/hr. The welding variables are 1) welding amperage, 2) type of flux and particle distribution, 3) voltage, 4) travel speed, 5) electrode size, 6) electrode stick out, 7) type of electrode, 8) width and depth of flux layer (12). The process can be highly automated and easily adapted to a robotic remote welding situation. Its drawbacks are flux must be removed between weld passes, and it cannot be used out of position. Flux removal can be overcome by pneumatic chiseling or brushing between passes. The fact that out of position welding is not possible dictates that the welding head must be stationary and the cylinder rotated to keep the weld pool in the horizontal position at all times.

Gas metal arc welding (GMAW) is a high current density, bare wire, gas shielded welding process where an arc is established between the bare wire and the

workpiece, and the molten pool that forms is protected by an inert, reactive, or combination inert-reactive gas. This gas also provides a highly ionized electrical path for the deposition of electrode to the plate by either: short circuiting transfer, globular transfer or spray transfer (13).

GMAW is considered a lower heat input welding process when compared with submerged arc welding, with deposition rates between 0.5 and 13 kg/hr. The short circuiting transfer mechanism has the lowest welding currents and smallest electrode diameter and is used for thin sheet or out-of-position welding. This mode of transfer is characterized in the following way: At the end of the electrode, wire melts into a small golbule of liquid metal, the molten metal moves toward the workpiece, taking an "hour glass" form. Where, upon contact, it creats a short circuit. Metal transfer is by gravity and surface tension. The molten metal is broken by a pinch force common to current carrying media. The amount of suddenness of pinch is controlled by the power supply (13). This phenomena occurs between 20 and 200 times per second according to welding variables.

Globular transfer has a higher current density than short circuiting. It is characterized by a large drop forming at the end of the electrode. The drop forms at the end of the electrode until the force of gravity overcomes the surface tension of the molten metal, at which time the drop falls into the molten weld pool. The drop transfer rate is between 100 and 500 drops/sec (12), and gives a higher deposition rate and allows for a higher wire speed than short circuiting modes.

Spray transfer occurs at high current density and results in a high heat input and high deposition rate. This type of transfer is characterized by small droplets emanating from the tip of the electrode (13). This mode is generally limited to the horizontal position and produces very little spatter.

The shielding gas changes the transfer mechanism and can be adjusted depending on application. The common shielding gases are helium, argon, carbon dioxide, and assorted mixtures of them (12).

This process is highly automatic and easily adapted to robotic remote operation. There is no need for interpass flux removal and multiple pass welding is easy. Out of position welding is not a problem which allows the

welding head to travel circumferentially around the cylinder to seal the top. This is a desirable feature as heavy machinery is not needed to rotate the cylinder. The only drawback is the deposition rate is lower than SAW so more time is needed for welding.

Electroslag welding (ESW) is the highest heat input welding process, and has a deposition rate of 7 to 60 kg/hr. Typical power supplies are 600 to 2000 amperes direct current and are fairly expensive (12).

In ESW, an arc is used to initiate welding by melting a granular slag. This slag is conductive in the molten state and acts as a weld metal atmospheric shield. After the slag is molten the arc is extinguished and welding proceeds by the heat produced by the resistance of this slag to current flow. The heat keeps the slag molten and above the liquidus temperature of the base plate and electrode. ESW is most commonly done in the vertical position and therefore must utilize water cooled copper shoes to keep molten metal from leaking out of the joint.

There are two common techniques in ESW, the conventional method and the consumable guide method. The conventional method uses a beryllium copper alloy guide

tube which moves upward with the welding head as the weld is filled, remaining at 50 to 75 mm above the molten bath. The consumable guide method uses a stationary guide which becomes part of the filler metal as welding proceeds. The welding head stays stationary and the guide tube melts and adds five to ten percent of the filler material (12). ESW has a bath temperature of 1925°C and a surface temperature of 1650°C, compared to conventional arc welds this is very low (12).

Electroslag welding is not a feasible process for welding overpack containers. To remotely weld by ESW the copper shoes would have to be manipulated into place and inspected for leaks. Flux additions would have to be made at intervals predetermined, as visual inspection would be impractical during remote welding. The process is designed to weld in the vertical position, and a modification would have to be made if a circumferential weld was to be produced.

Flux cored arc welding (FCAW) is merely a slight modification of GMAW. A tubular electrode filled with atmospheric protecting flux and/or alloying elements is used either with a protective cover gas or without. The material transfer and equipment are the same as in GMAW.

The advantage of FCAW is that alloy additions can be made through the powder additions inside the tubular electrode, however flux must be removed between passes which may cause difficulty in a remote welding situation.

Each one of the aforementioned welding processes will have different energy input with GMAW being the lowest (0.5-3 MJ/m) followed by SAW (1.0-10 MJ/m). ESW has the highest energy input (50.5-MJ/m) and as such will have the widest heat affected zone. Figure 5 schematically represents the grain size as a function of distance from the fusion line (14). As expected, this grain growth region becomes wider with higher energy input. More base metal is heated to critical temperatures, and cooling is slower as energy input increases.

The large grains next to the fusion line are detrimental to impact toughness and tensile properties. These grains also have increased hardenability due to their size and will transform on cooling to lower austenite decomposition products (bainite and martensite), which again is detrimental to impact properties (15). The steels used in this investigation are low carbon, low alloy, and martensite will not occur

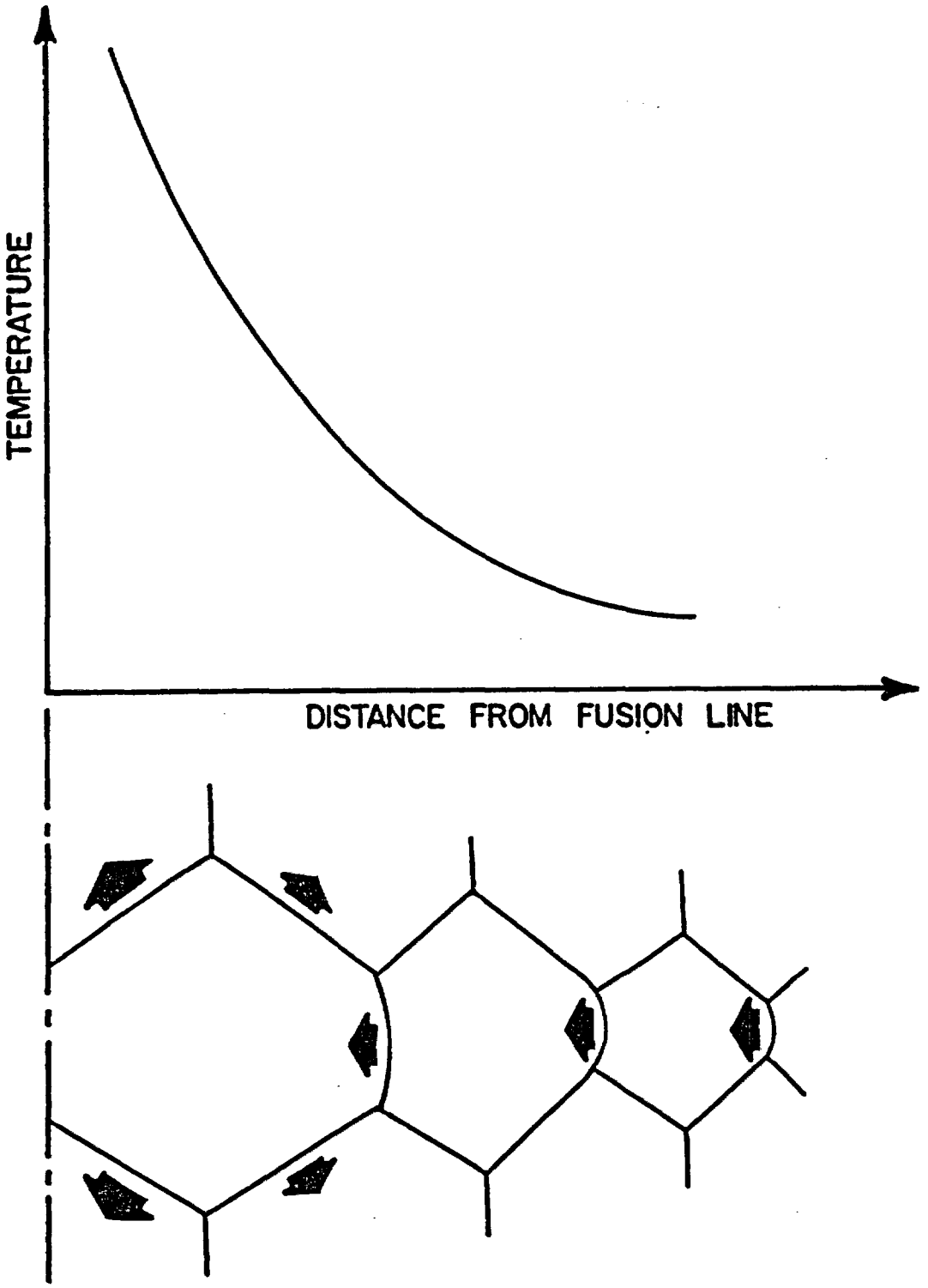

Figure 5. Grain size in the heat affected zone as a function of peak temperature and distance from the fusion line (14).

as cooling rates necessary to get martensite are higher than the cooling rates of the welding process. An in-depth discussion of the factors involved in determining heat affected zone microstructure is discussed later in this thesis.

After evaluating the manufacturing processes it was found that centrifugal casting and closing the ends by SAW or GMAW would be the best commercially available manufacturing technique for the overpack containers. For this investigation submerged arc welding was the preferred technique and gas metal arc welding will be the subject of a future investigation.

1.4 HEAT TRANSPORT

A modification of the Rosenthal equation (16) can be used to model three dimensional heat transport in the welds in order to predict time-temperature profiles in the heat affected zone. Figure 6 illustrates the difference between one, two, and three dimensional forms of the equation.

The Rosenthal equation for three dimensional heat transport in a thick section weld is:

$$T - To = \frac{q/v}{2\pi\lambda t} \exp\left(\frac{-r^2}{4at}\right) \quad \text{(EQ 1)} \qquad (14)$$

where:

To	=	initial temperature prior to welding ($200^{o}C$)
q	=	ηVI
η	=	arc efficiency (0.90 to 0.99 for SAW)(17)
V	=	weld voltage
I	=	weld amperage
v	=	weld travel speed in m/s (5.08×10^{-3}m/s)
λ	=	thermal conductivity in $Jm^{-1}s^{-1}k^{-1}$
r	=	$(\S^2 + y^2 + Z^2)^{\frac{1}{2}}$
$\S$	=	x-vt
x	=	x-coordinate at the point of interest (m).
t	=	time (sec.)
y	=	y-coordinate at the point of interest (m).
Z	=	Z-coordinate at the point of interest (m).
a	=	$\lambda/\rho C$
ρ	=	density of material (kg/m^3)
C	=	specific heat ($m^2\ sec^{-2}\ K^{o-1}$)
ρC	=	has units of $Jm^{-3}k^{-1}$

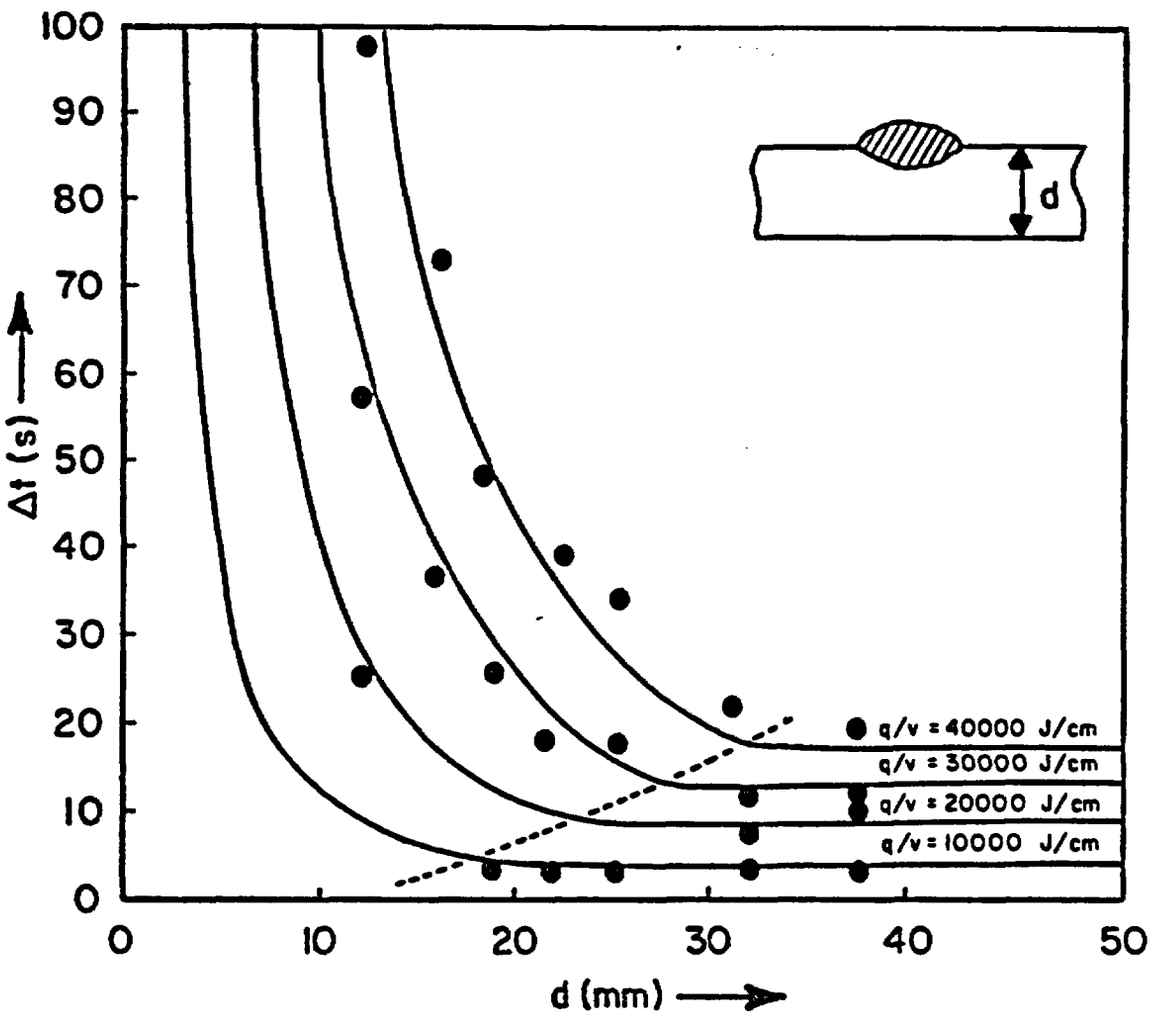

Figure 6. Calculated and measured values of Δt vs plate thickness for various heat inputs (14).

This equation describes a moving point heat-source which moves at a constant velocity as shown in Figure 7 (14). The important assumptions made in developing equation 1 are significant when using it as a theoretical model, and they are: constant physical properties such as thermal conductivity, a point source of heat, and neglect of surface heat losses and joule heating (16).

Each casting and welding process described will yield a unique final overpack microstructure. Controlling and predicting this microstructure through an understanding of the manufacturing process variables will assist the Nuclear Regulatory Commission in evaluating ASTM A-216 grade WCA steel as a viable option for containing high level nuclear waste. The experimental program undertaken to accomplish the aforementioned task follows.

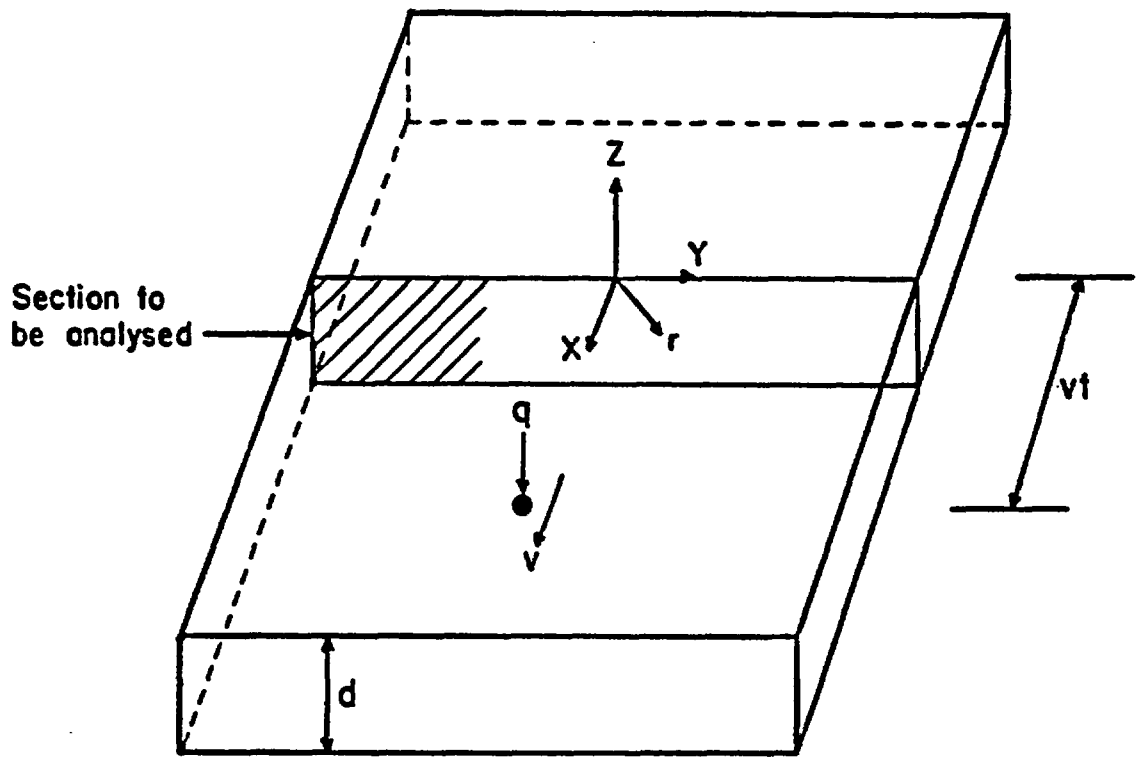

Figure 7. Welding coordinates in terms of a point source q and a velocity v (14).

2.0 EXPERIMENTAL PROCEDURE

The experimental objective was to investigate the influence of melting, casting, and welding process variables on the microstructure of ASTM A-216 grade WCA carbon steel castings. Three compositions within the specification were selected to provide high and low manganese/oxygen ratios, and the addition of sulfur, to investigate the influence of sulfide inclusions. The three design compositions are shown in Table I.

Steel making was carried out in a coreless induction furnace using the melting and quality assurance procedures specified in Appendix C. Static castings and chill castings were poured and heat treated by normalizing. Submerged arc welding was carried out on all three alloys using a semi-automatic welding unit. Finally, thermo-mechanical simulation (Gleeble) of the heat affected zone as a result of this welding process was completed in order to generate samples suitable for mechanical testing.

2.1 STATIC CASTING

The furnace crucible used to model static casting is shown in Figure 8. A number 4 graphite susceptor was placed on top of refractory brick, inside an Inductotherm 30, 50 pound (23 kg) coreless induction furnace. The susceptor was lined with asbestos paper and rammed with Al_2O_3 castable refractory. One inch (25.4 mm) AlSl 1018 steel bar stock was placed in the Al_2O_3 crucible and the susceptor and crucible were covered with a two hole graphite lid. An Al_2O_3 protected type R thermocouple was placed in one hole and a hollow Al_2O_3 tube connected to argon shielding gas was in the other. A numatron digital thermocouple monitor was connected to the type R thermocouple, and 30 cfh (850 l/hr) argon was used to shield the melt.

The power on the induction furnace was turned on and the AlSl 1018 steel bar was brought up to 1550°C. The molten charge was slowly cooled by turning the reostat down on the power supply. The thermocouple monitored the cooling rate resulting in the time-temperature data shown in Figure 9. After cooling to room temperature the Al_2O_3 crucible was removed with the now solidified nugget of

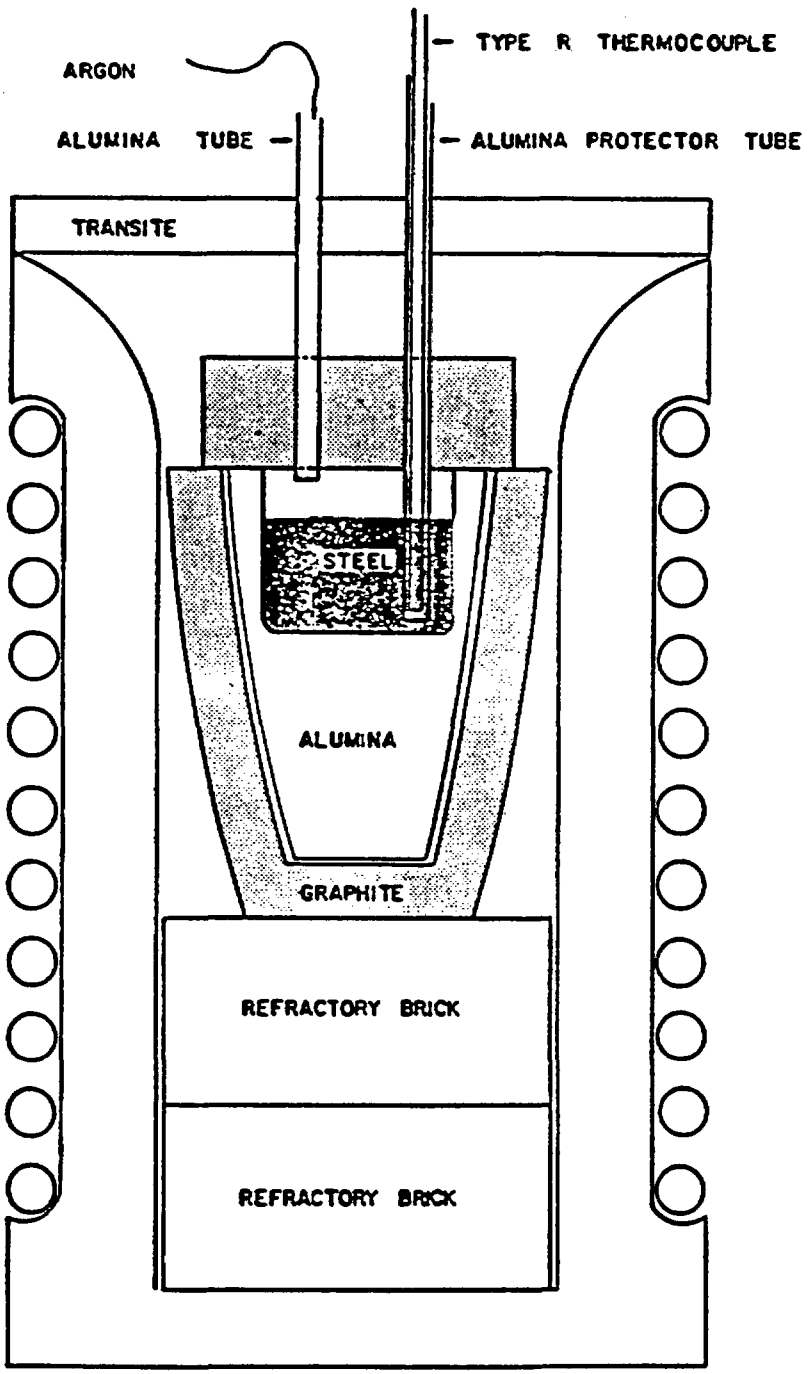

Figure 8. A schematic diagram of the furnace solidifying equipment used to model static casting.

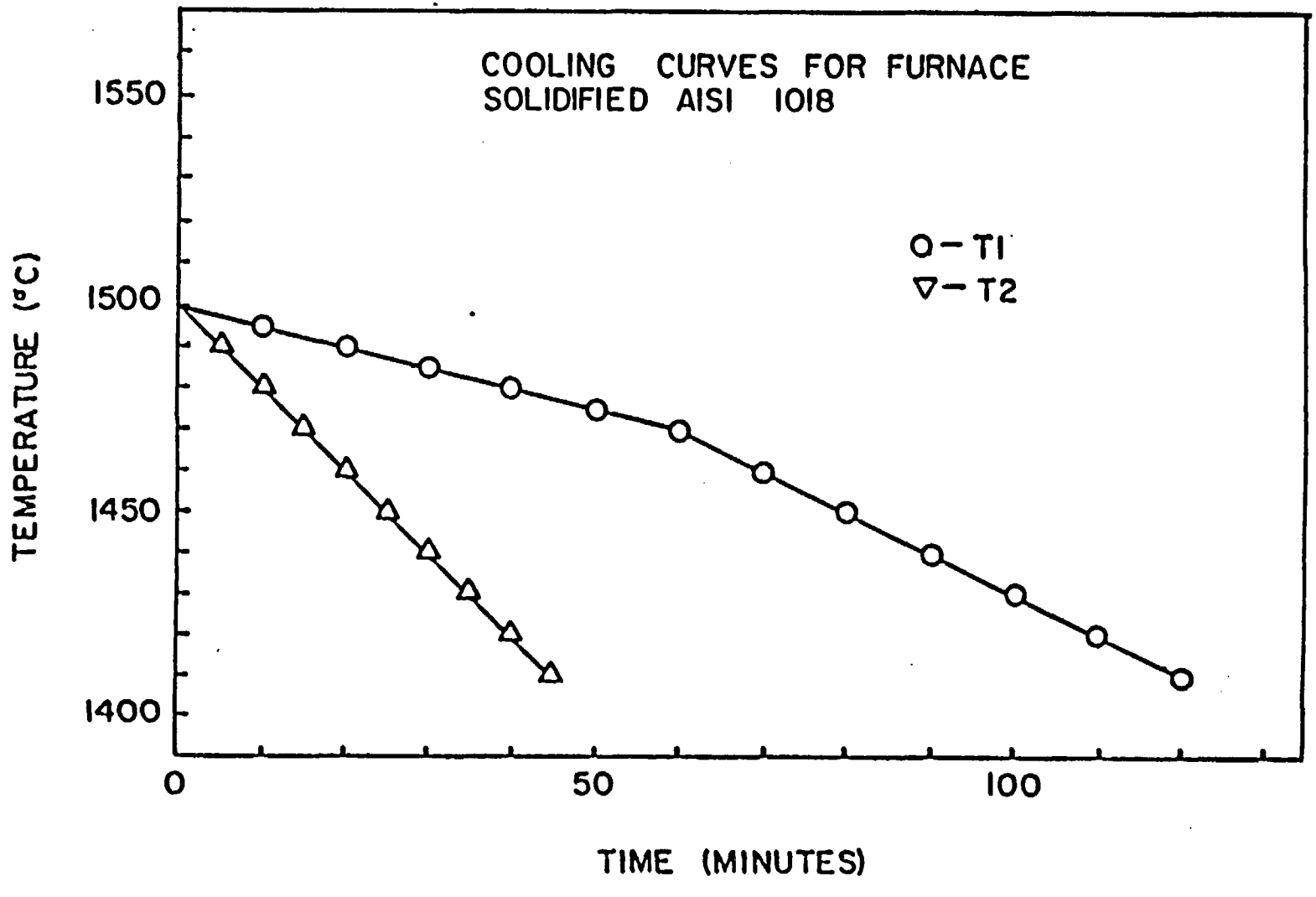

Figure 9. Cooling curves obtained from furnace solidified specimens.

steel, and shot blasted away. Two heats were produced by the above technique and were sectioned for metallographic analysis. The chemical control was unimportant as this procedure was designed to show secondary dendrite arm spacing versus solidification time, which is independent of alloy content (10). Figure 10 shows a plot of secondary dendrite arm spacing as a function of solidification time for a wide variety of conventional steels. The importance of secondary dendrite arm spacing on mechanical and corrosive container performance will be addressed in the results and discussion. It is only important here to describe the technique used to achieve long solidification times.

2.2 INGOT MOLD FABRICATION

Ingot molds were manufactured to act as chill molds which would simulate the centrifugal casting process. Two wooden patterns were constructed from pine, rammed in olivine molding sand, and cast with class 30 grey iron. The grey iron mold halves were matched together according to the configuration of Figure 11a and 11b. Each mold and a 1" x 6" x 18" (25.4 mm x 152.4 mm x 457.2 mm) strip

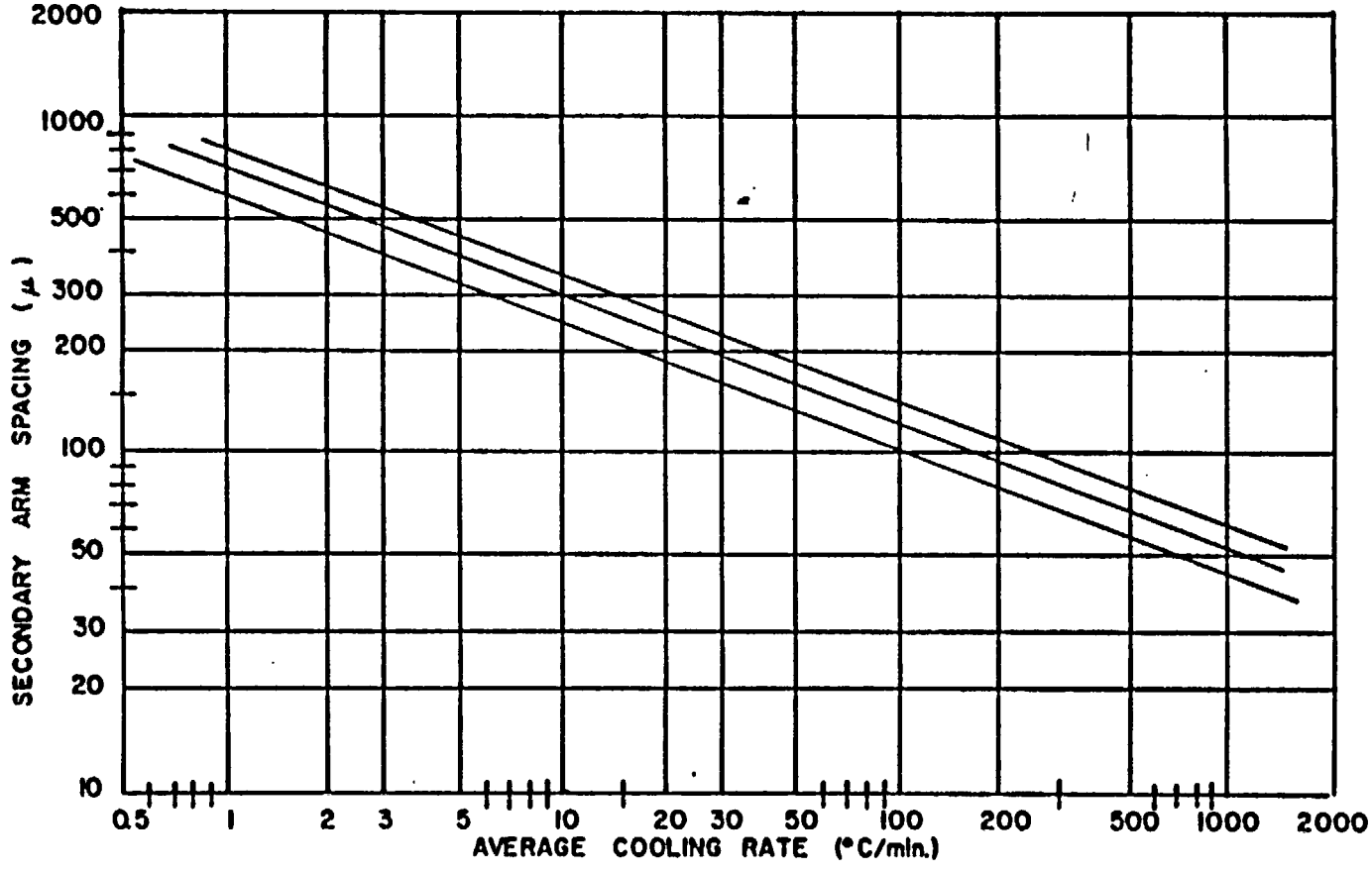

Figure 10. Experimental data on dendrite arm spacings in commercial steels containing from 0.1 to 0.9 weight percent carbon (10).

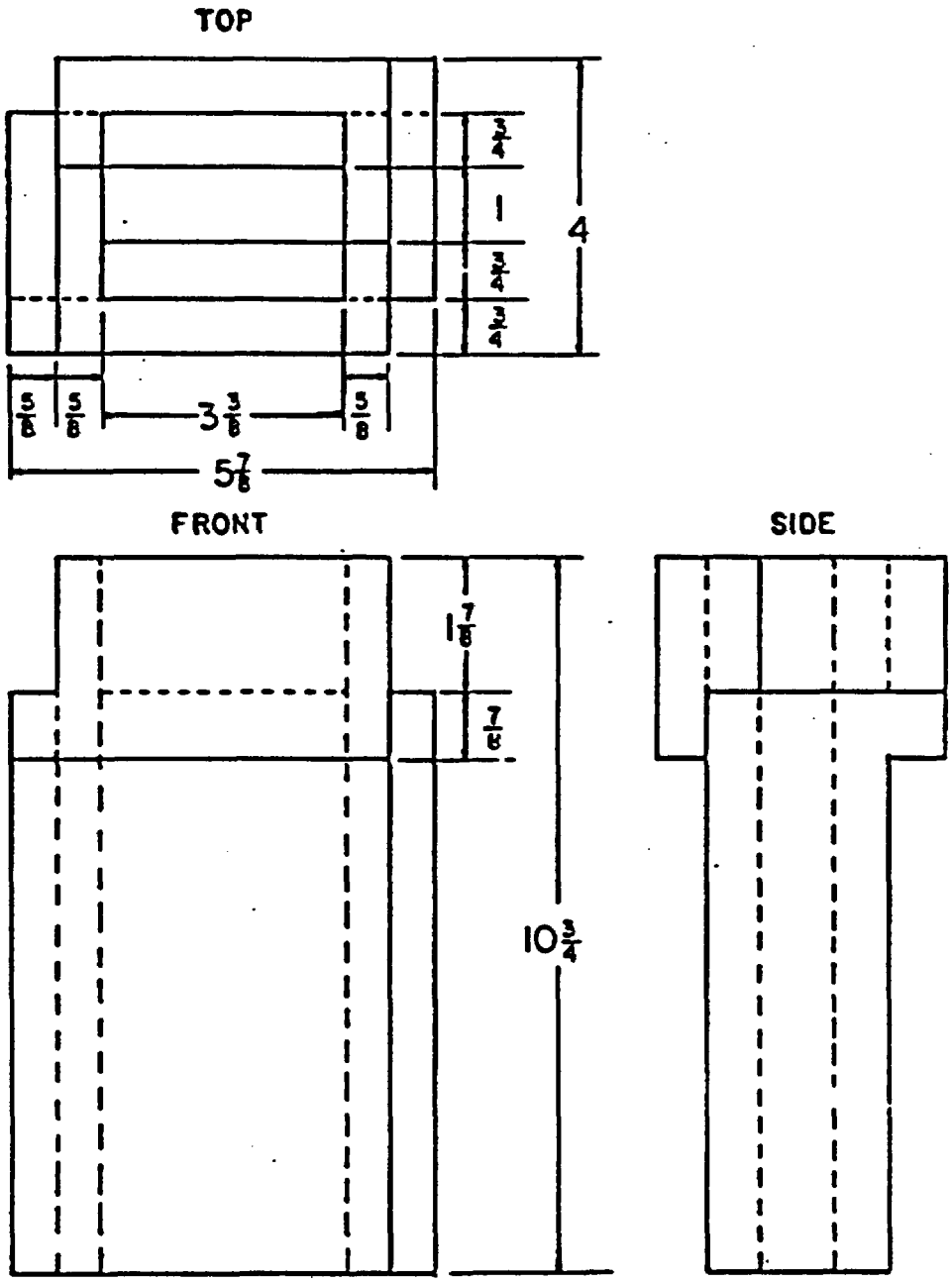

Figure 11a. The ingot mold design used for casting one inch (25.4 mm) thick steel plate.

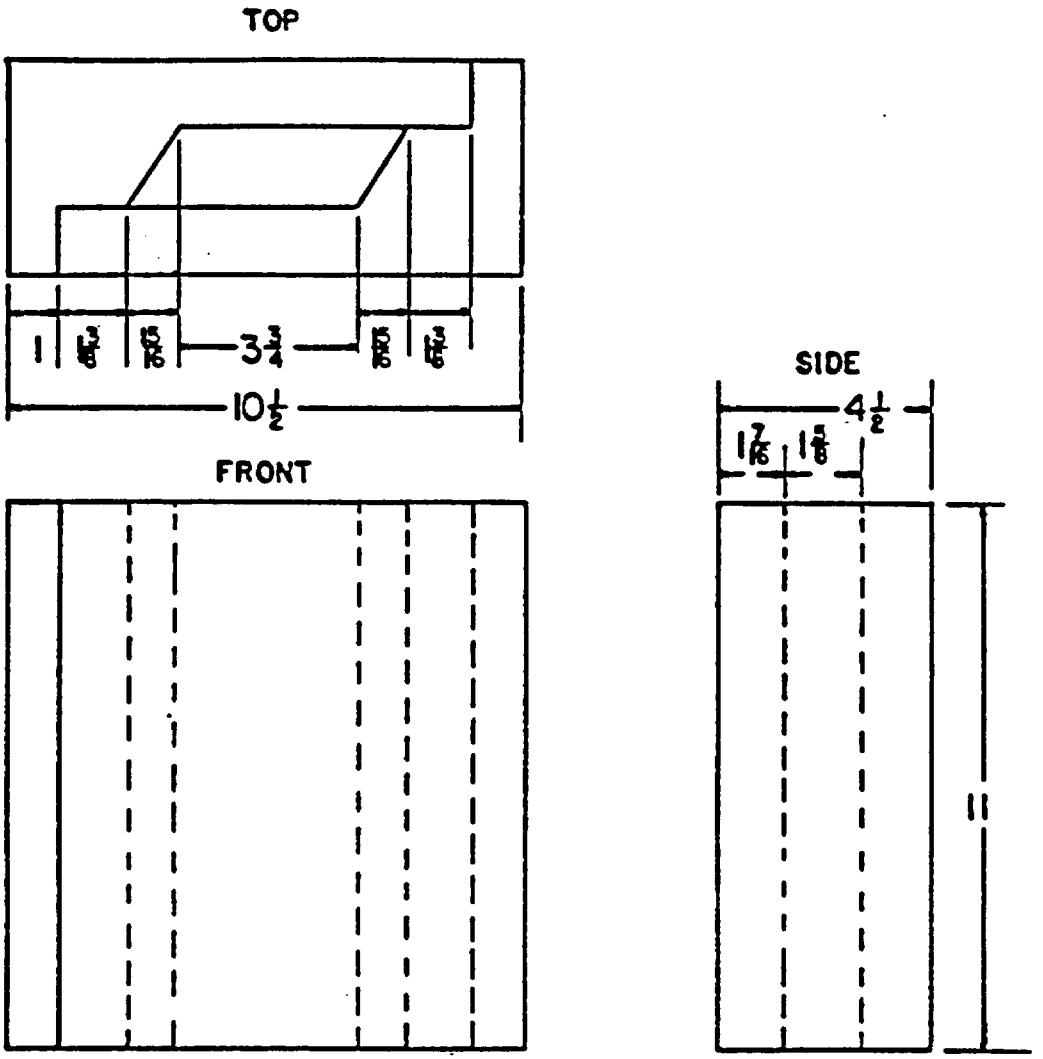

Figure 11b. The ingot mold design used for casting 1.5 inch (38.1 mm) thick steel weld plate.

of ductile iron plate was painted with a water base Al_2O_3 mold wash, and dried. The molds were arranged on the ductile iron chill plate and olivine molding sand was rammed between them as shown in Figure 12. This configuration was used to cast all the experimental plate for this investigation.

2.3 PIG IRON PRODUCTION

Before any steel could be made, pig iron was produced in the Inductotherm 30, 50 pound (23 kg) induction furnace. Bar stock (SCM Metal Products ENL101) of chemical composition (weight percent): %C-0.0026, %Mn-0.006, %Si-0.0017, %P-0.0012, %S-0.0024 was added cold along with powdered graphite, brought up to 1430°C and poured into olivine sand molds. Ferrosilicon was added when needed to control a carbon monoxide boil but it was kept to a minimum to insure the pig iron would be white. Pig iron was also made with ARMCO A101 steel bar stock of chemical composition: %C-0.034, %Mn-0.053, %Si-0.003 and %S-0.007, using the above procedure. Table II shows the chemical analysis of the pig irons used for the steel making process.

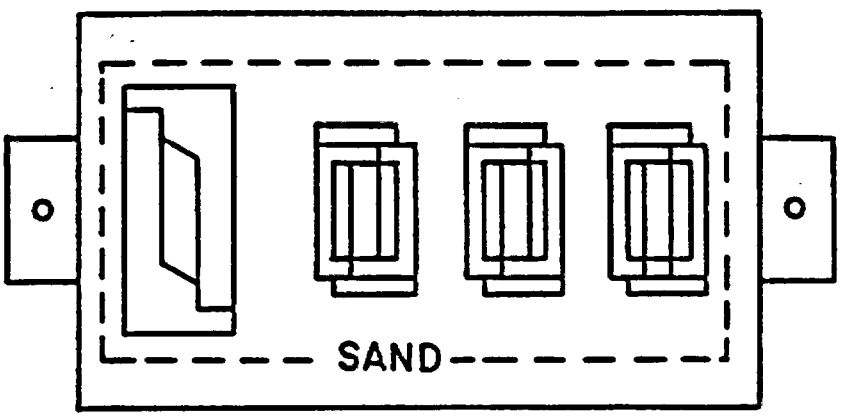

Figure 12. Mold configuration prior to tapping steel.

Table II. Chemical analysis (weight percent) of pig iron used to produce experimental steel.

Identity	%C	%Mn	%Si	%S
NRC-P1	4.05	-	0.50	0.006
NRC-P2	4.08	0.14	0.30	0.007
NRC-P3	3.30	0.10	0.10	0.01
NRC-P5	3.74	0.64	0.13	0.01

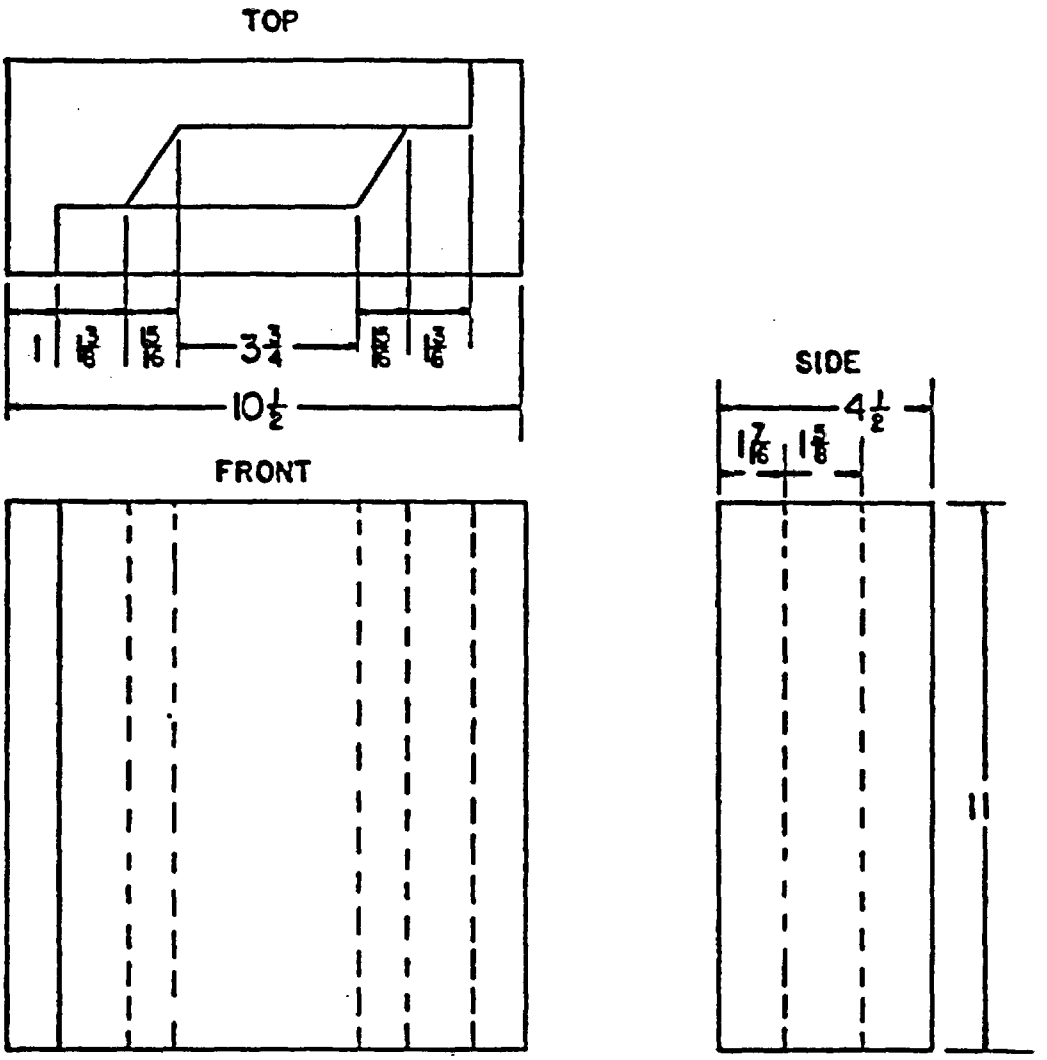

Figure 11b. The ingot mold design used for casting 1.5 inch (38.1 mm) thick steel weld plate.

of ductile iron plate was painted with a water base Al_2O_3 mold wash, and dried. The molds were arranged on the ductile iron chill plate and olivine molding sand was rammed between them as shown in Figure 12. This configuration was used to cast all the experimental plate for this investigation.

2.3 PIG IRON PRODUCTION

Before any steel could be made, pig iron was produced in the Inductotherm 30, 50 pound (23 kg) induction furnace. Bar stock (SCM Metal Products ENL101) of chemical composition (weight percent): %C-0.0026, %Mn-0.006, %Si-0.0017, %P-0.0012, %S-0.0024 was added cold along with powdered graphite, brought up to 1430°C and poured into olivine sand molds. Ferrosilicon was added when needed to control a carbon monoxide boil but it was kept to a minimum to insure the pig iron would be white. Pig iron was also made with ARMCO A101 steel bar stock of chemical composition: %C-0.034, %Mn-0.053, %Si-0.003 and %S-0.007, using the above procedure. Table II shows the chemical analysis of the pig irons used for the steel making process.

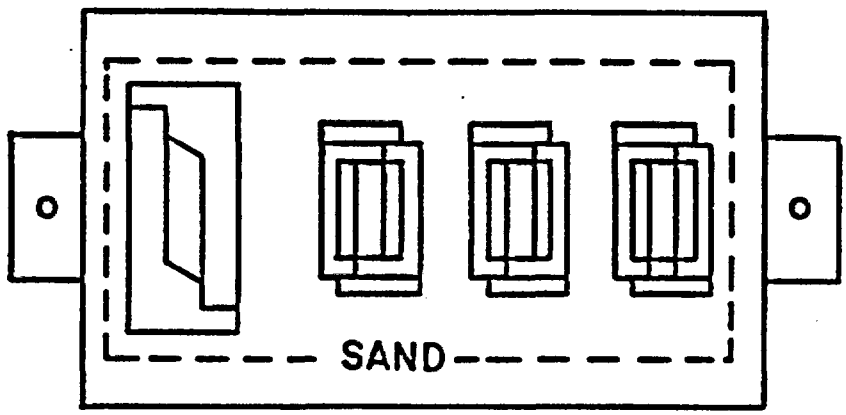

Figure 12. Mold configuration prior to tapping steel.

Table II. Chemical analysis (weight percent) of pig iron used to produce experimental steel.

Identity	%C	%Mn	%Si	%S
NRC-P1	4.05	-	0.50	0.006
NRC-P2	4.08	0.14	0.30	0.007
NRC-P3	3.30	0.10	0.10	0.01
NRC-P5	3.74	0.64	0.13	0.01

2.4 STEEL PRODUCTION

Nineteen heats of steel were produced in the 50 pound (23 kg) Inductotherm 30 furnace. The charge calculations and melt logs used in this phase of the investigation were essential to predicting the final chemical analysis of the steel. It was found that the reactions that took place during steelmaking should be monitored and documented during the duration of the steelmaking process in order to duplicate successful heats and avoid poor quality castings. The critical documentation was: type of scrap, temperature of alloy additions, type of bar, furnace and ladle conditions, time spent in the furnace after alloy additions, pouring temperature, tapping temperature, ladle time, and deoxidation additions. Keeping procedure consistent was essential to quality control.

An iterative charge calculation technique was used for heats NRC-1 through NRC-16. An example of this and instructions for its use are in Appendix C. Charge calculations for heats NRC-17 through NRC-19 were done on an HP15C hand calculator using matrix algebra.

Melt logs for every heat were kept, noting times and temperatures at which additions were made. The steelmaking procedure follows.

Scrap and bar stock were added cold. The power was turned on and the heat was brought to the molten state. At meltdown 30 grams of standard ferrosilicon was added to control any premature boil. At 1600°C pig iron was added which induced a carbon monoxide boil, and simultaneously increased the carbon level of the melt. The carbon monoxide boil was allowed to go on for exactly five minutes at which time 50 grams of ferrosilicon was added to block the boil. The temperature of the melt was brought up to 1675°C in ten minutes. (The time between the end of the carbon monoxide boil and 1675°C was critical. If it was longer than ten minutes, plus or minus three minutes, then the carbon losses were inconsistent.) At 1675°C the balance of the ferrosilicon was added and the heat was tapped to the ladle, which contained the ferromanganese and one half of the aluminum charge. The balance of the aluminum was added to the molten stream during tapping to the ladle. The slag was removed and the ladle was tapped to the molds. The time between tapping from the furnace and pouring the molds

varied from 30 seconds to two minutes depending on the desired oxygen content. The high sulfur heats needed an addition of pyrite (FeS_2) and that was added cold with the bar stock at the beginning of the heat. The bar stock used was the same as the bar used to make pig iron and is shown in Table II. The scrap used which was AlSl 1008 and AISI 1018 steel, and the ferromanganese, ferrosilicon and pyrite compositions are shown in Table III.

2.5 CHEMICAL ANALYSIS

After each heat a chemical analysis was determined using a vacuum emission spectrometer. The carbon, sulfur and oxygen contents were determined using a Leco carbon/sulfur determinator and a Leco oxygen/nitrogen determinator. The results of the chemical analysis are shown in Table IV. The melt losses were computed and the next charge calculation was made. A summary of losses for each heat is shown in Table V. The losses shown are unique to the furnace used, the melting procedure, and the alloy cast.

Table III. Chemical analysis (weight percent) of ferro-alloys and scrap used to make experimental steel.

Addition	Identity	%C	%Si	%Mn	%S	%Al
Bar Stock	A101	0.0026	0.0017	0.0006	0.0024	-
Bar Stock	ENL101	0.0340	0.003	0.053	0.007	-
Scrap	AISI 1008	0.087	0.50	0.41	0.021	-
Scrap	AISI 1018	0.21	0.25	0.86	0.02	-
FeMn	Med. Carb	1.46	1.46	80.10	-	-
FeSi	Stndrd.	-	50.0	-	-	-
FeS_2	Pyrite	-	-	-	53.33	-
Al	Shot	-	-	-	-	100

Table IV. Chemical analysis (weight percent) of cast experimental steels.

Heat No.	%C	%Mn	%Si	%S	%P	%Al	Mn/O	%O
Alloy A	0.18	0.50	0.10	0.01	0.02	0.05	25	0.0200
Alloy B	0.18	1.00	0.25	0.01	0.02	0.05	145	0.0070
Alloy C	0.18	1.00	0.25	0.045	0.02	0.05	145	0.0070
NRC-1	0.13	0.60	0.04	0.009	0.016	0.015	38.5	0.0156
NRC-2	0.17	0.44	0.02	0.01	0.02	NA	NA	NA
NRC-3	0.14	0.45	0.19	0.01	0.01	0.047	30.4	0.0148
NRC-4	0.17	0.63	0.09	0.01	0.01	0.044	42.9	0.0147
NRC-5	0.17	0.51	0.10	0.01	0.008	0.043	44.7	0.0114
NRC-8	0.21	1.12	0.41	0.01	0.02	0.030	106.7	0.0105
NRC-9	0.20	0.50	0.33	0.01	0.008	0.054	34.2	0.0146
NRC-10	0.09	0.81	0.06	0.01	0.013	0.025	31.4	0.0258
NRC-11	0.15	0.97	0.19	0.01	0.014	0.034	87.4	0.0111
NRC-12	0.17	1.06	0.32	0.01	0.013	0.050	64.2	0.0165
NRC-13	0.09	0.01	0.23	0.035	0.013	0.061	0.57	0.0176
NRC-14	0.15	1.07	0.21	0.045	0.012	0.054	49.1	0.0218
NRC-15	0.21	1.13	0.20	0.01	0.014	0.030	188.3	0.0060
NRC-16	0.24	0.38	0.24	0.01	0.009	0.040	NA	NA
NRC-17	0.21	0.41	0.23	0.007	0.007	0.038	NA	NA
NRC-18	0.16	1.01	0.28	0.008	0.01	0.023	NA	NA
NRC-19	0.18	0.90	0.30	0.045	0.002	0.045	NA	NA

Table V. Alloy losses (weight percent) that occurred during steelmaking.

Heat	Wt.% C	Wt.% Si	Wt.% Mn	Wt.% S	Wt.% Al
NRC-1	44.1	72.0	3.5	0	77.5
NRC-2	33.9	88.0	15.4	0	NA
NRC-3	47.5	69.5	17.5	0	29.6
NRC-4	48.1	72.4	NA	0	34.1
NRC-5	49.9	71.5	14.5	0	35.6
NRC-8	40.3	53.0	15.7	0	55.1
NRC-9	40.0	38.7	57.9	0	19.2
NRC-10	74.25	80.0	27.1	0	62.6
NRC-11	51.0	53.4	12.7	0	49.0
NRC-12	50.7	40.1	10.0	0	25.1
NRC-13	74.7	50.6	13.1	10	8.7
NRC-14	56.8	55.6	8.0	10	19.2
NRC-15	39.19	62.2	3.9	0	55.1
NRC-16	37.17	31.6	32.4	0	43.0
NRC-17	44.1	34.5	30.0	0	43.0
NRC-18	50.3	44.0	30.6	0	65.6
NRC-19	50.3	34.0	37.5	10	33.0

A sample from each heat of the one inch (25.4 mm) thick cast plate designed for the machining of Gleeble specimens was sectioned for metallographic examination. Each sample was polished to a 0.05 micron Al_2O_3 finish, etched with two percent nital, examined under a microscope, and photographed.

2.6 HEAT TREATMENT

The specifications for ASTM A-216 grade WCA steel call for the material to be delivered in the normalized, normalized and tempered , or annealed condition. Normalizing was the chosen condition for this investigation. Volume 7 of the 8th edition of the ASM Metals Handbook (17) revealed micrographs of normalized ASTM A-216 grade WCA steel, reproductions of which are shown in Figure 13.

The standard normalizing treatment for these steels is: Austenitize at 900°C for one hour per inch (25.4 mm) of thickness and air cool (18). A one inch (25.4 mm) thick cast plate of heat NRC-5 was treated by the above technique and sectioned for metallographic analysis. The grain size of 18 microns was calculated using the ASTM

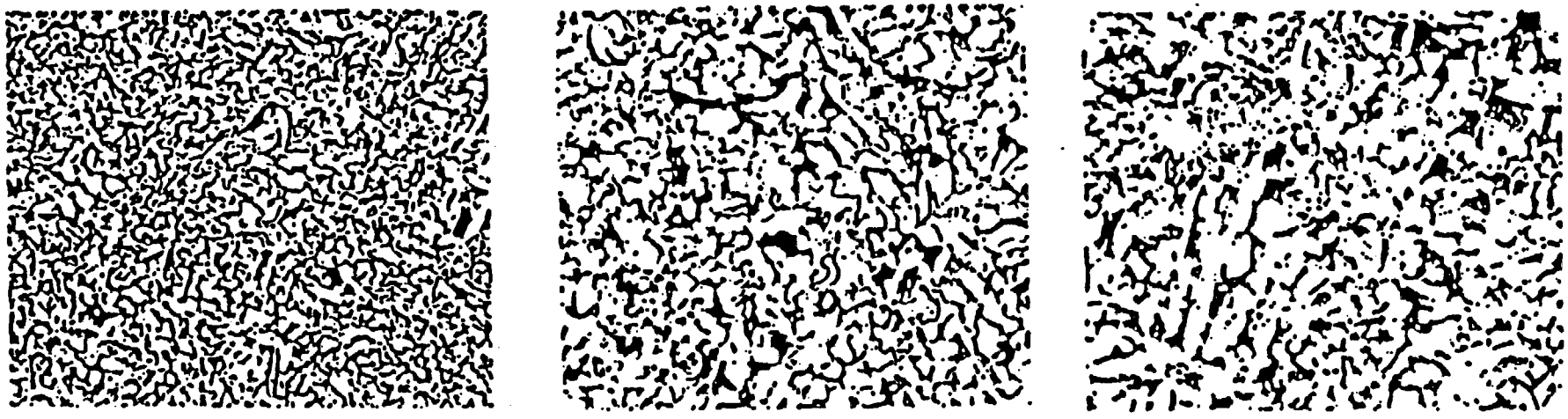

Figure 13. Reproductions of micrographs from the ASM Volume 7, eight edition of Metal Handbook, depicting grain size differences with varying section thickness. All steels shown have been normalized using standard normalizing treatments.

mean linear intercept technique and multiplied by 1.776 for three dimensions (19). The ferrite grain size varies with increased section thickness as shown in Table VI. The design for the overpack containers require wall thicknesses between three and fourteen inches (76.2 mm and 356 mm). This increase in section thickness yields a larger room temperature ferrite grain size than the one inch (25.4 mm) and 1.5 inch (38.1 mm) experimental steel, due to longer austenitizing times and slower cooler rates. The cooling rate of a six inch (152.4 mm) diameter casting cooled from a normalizing temperature of 900°C is approximately 10°C per minute as shown in Figure 14 (20). A controlled cooling device was designed to allow the one inch (25.4 mm) thick plates of this investigation to cool at 10°C per minute, and is shown in Figure 15. The calibration curves for this unit are shown in Figure 16. A type K thermocouple was mounted in predrilled holes to monitor the cooling rates shown in Figure 16. Curve one does meet the 10°C per minute criteria, however, due to the shorter austenitizing time (one hour as opposed to three hours), the room temperature ferrite grain size remained small. A modified heat treatment: austenitize at 1050°C for two hours, and cool in the cooling unit,

Table VI. Grain sizes of normalized ASTM-A216 grade WCA steels with varying section thicknesses.

Section Thickness	Grain Size (microns)
Experimental (1 in.)	18
Volume 7 (1 in.)	22
Volume 7 (3 in.)	36
Volume 7 (6 in.)	41

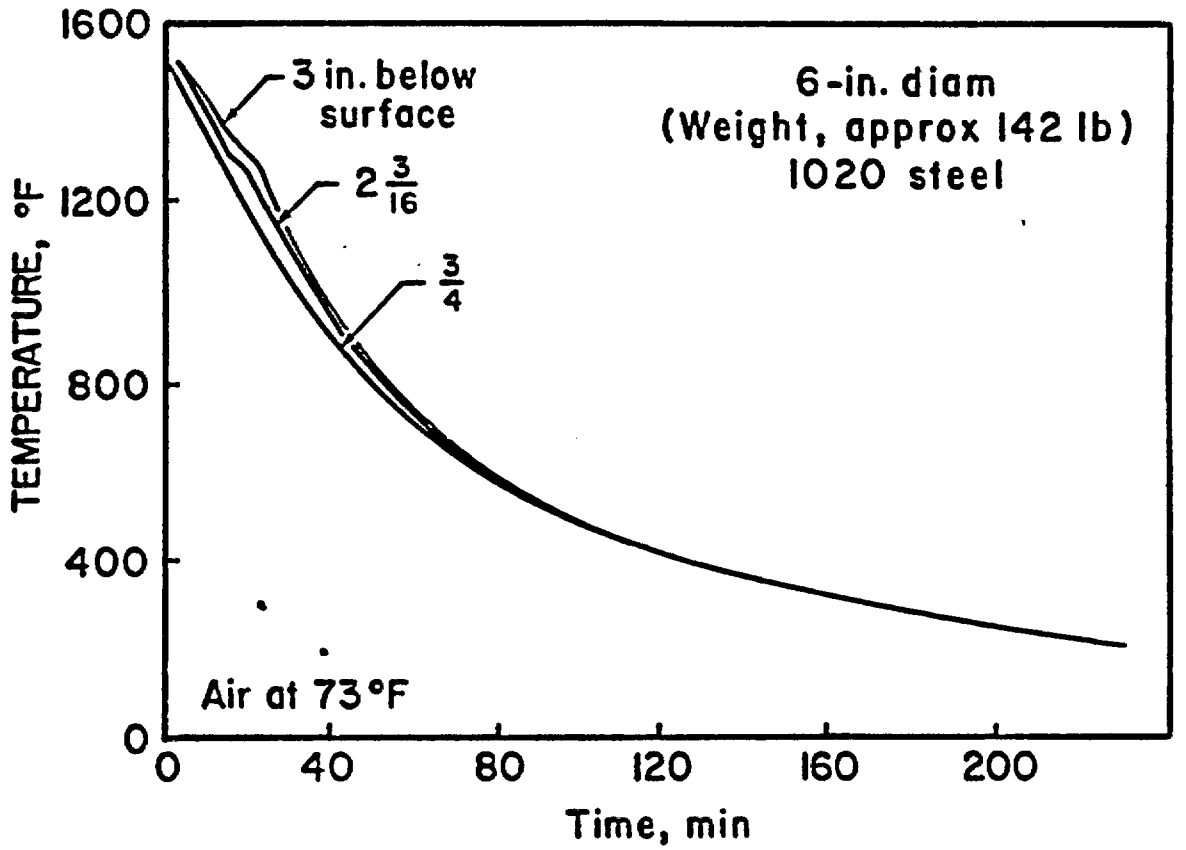

Figure 14. Cooling curve for a six inch diameter steel casting from a normalizing temperature of 900°C.

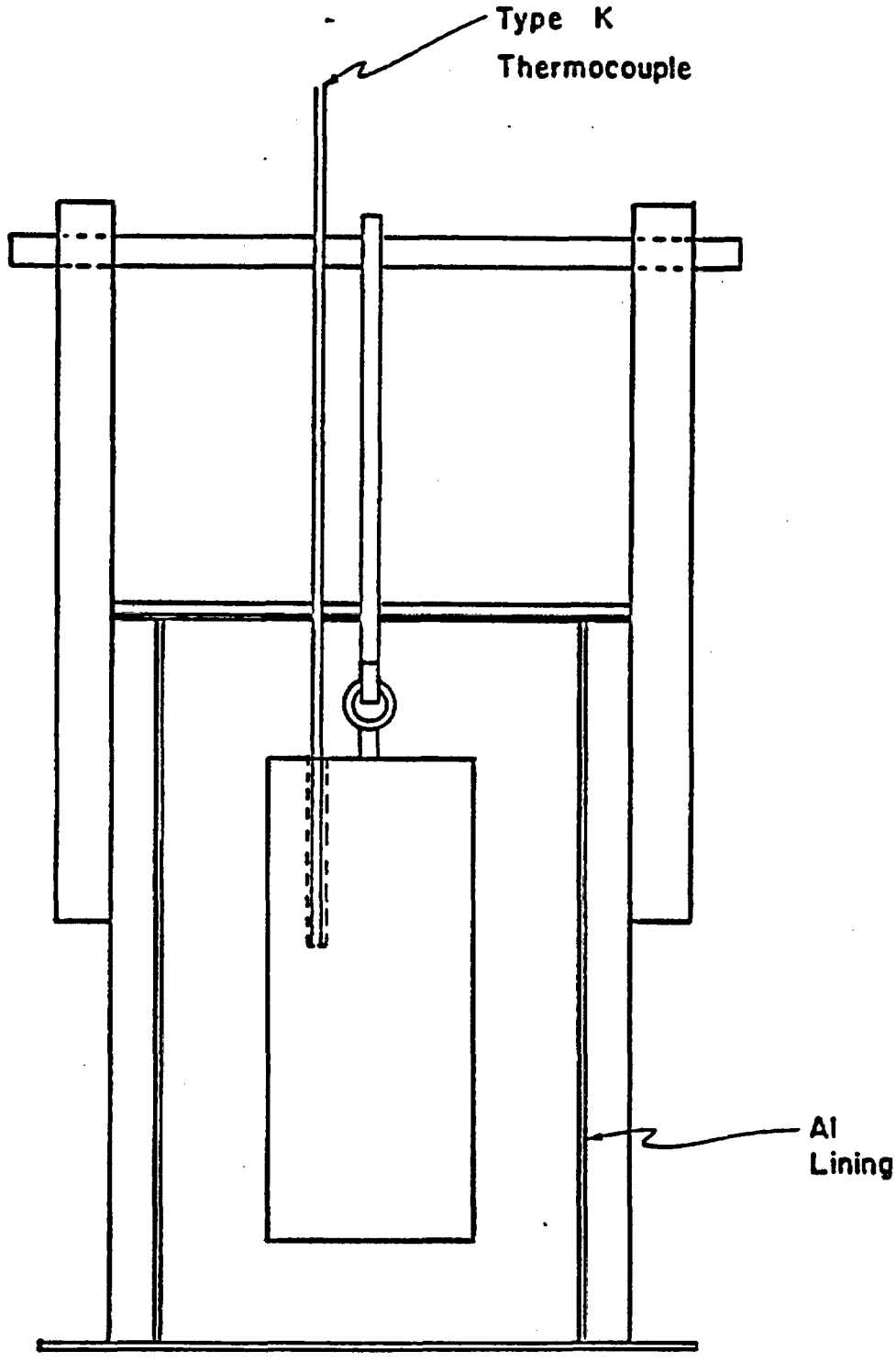

Figure 15. A schematic of the slow cooling device used to slow the cooling rate of a one inch (25.4 mm) thick plate to that of a 6 inch (152.4 mm) thick plate.

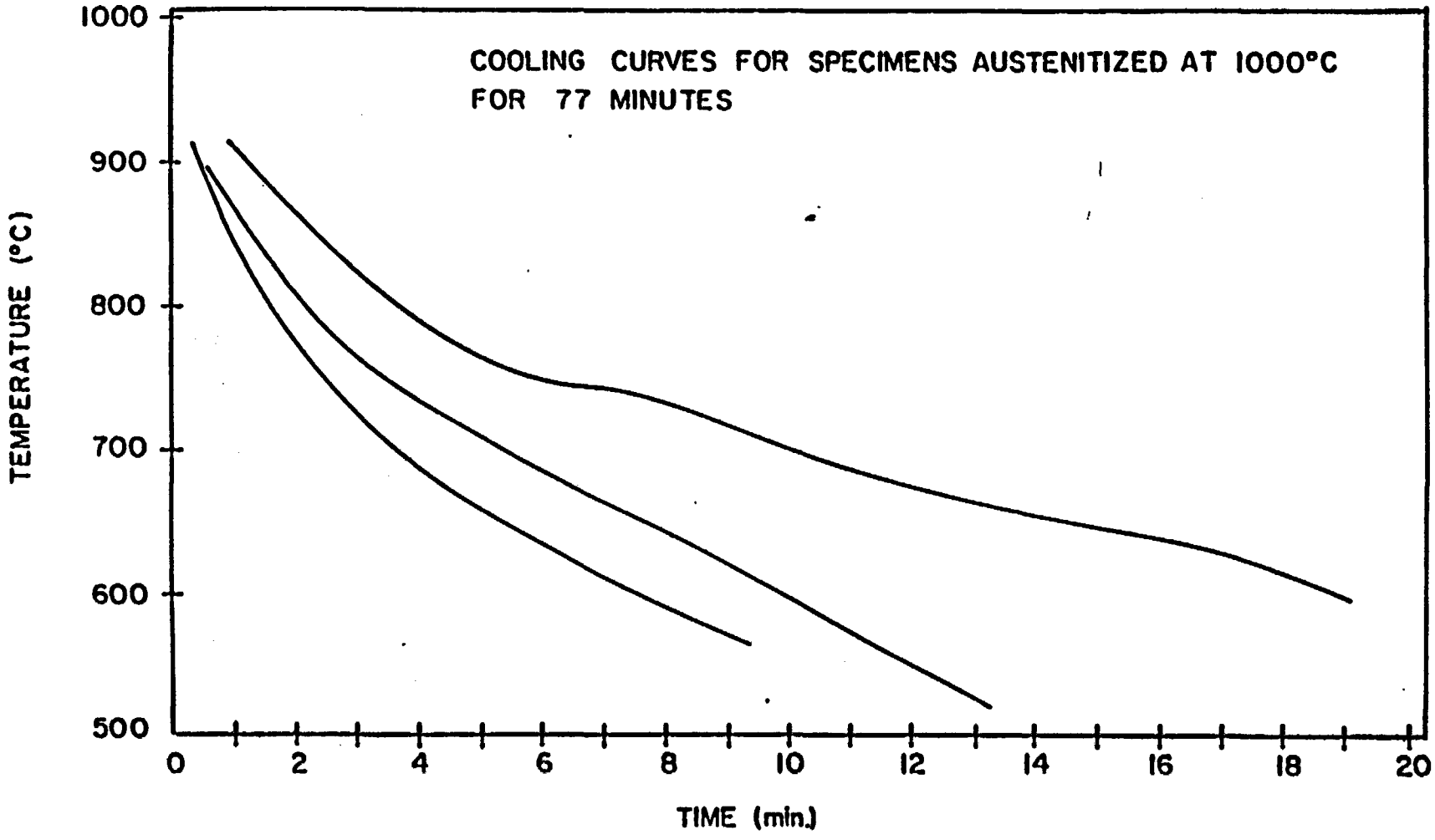

Figure 16. Calibration curves obtained from the slow cooling device of Figure 15.

yielded the desired room temperature ferrite grain size.

2.7 THERMOCOUPLE INSTALLATION AND CONSIDERATIONS

After the 1.5 inch (38.1 mm) weld plates were specially normalized, they were machined to the configuration of Figure 17. The plates were then instrumented with thermocouples to monitor the heat affected zone thermal cycle during the welding process. Two 5/64 inch (2 mm) diameter holes were drilled in each weld plate approximately six inches (152.4 mm) apart as depicted in the figure. The hole depth varied depending on what region of the heat affected zone was monitored. A 0.005 inch (.127 mm) diameter bare platinum wire was welded to a 0.005 inch (.127 mm) diameter bare platinum 13 weight percent rhodium wire using a capacitive discharge 150 volt welder, and a graphite block. The bare thermocouple was welded to the bottom of the predrilled holes using the same capacitor discharge welder. A schematic of the down hole welding process for thermocouples (21) is shown in Figure 18. The bare wires were protected by an Al_2O_3 two hole protector tube which slid over the two wires to prevent short circuiting. The

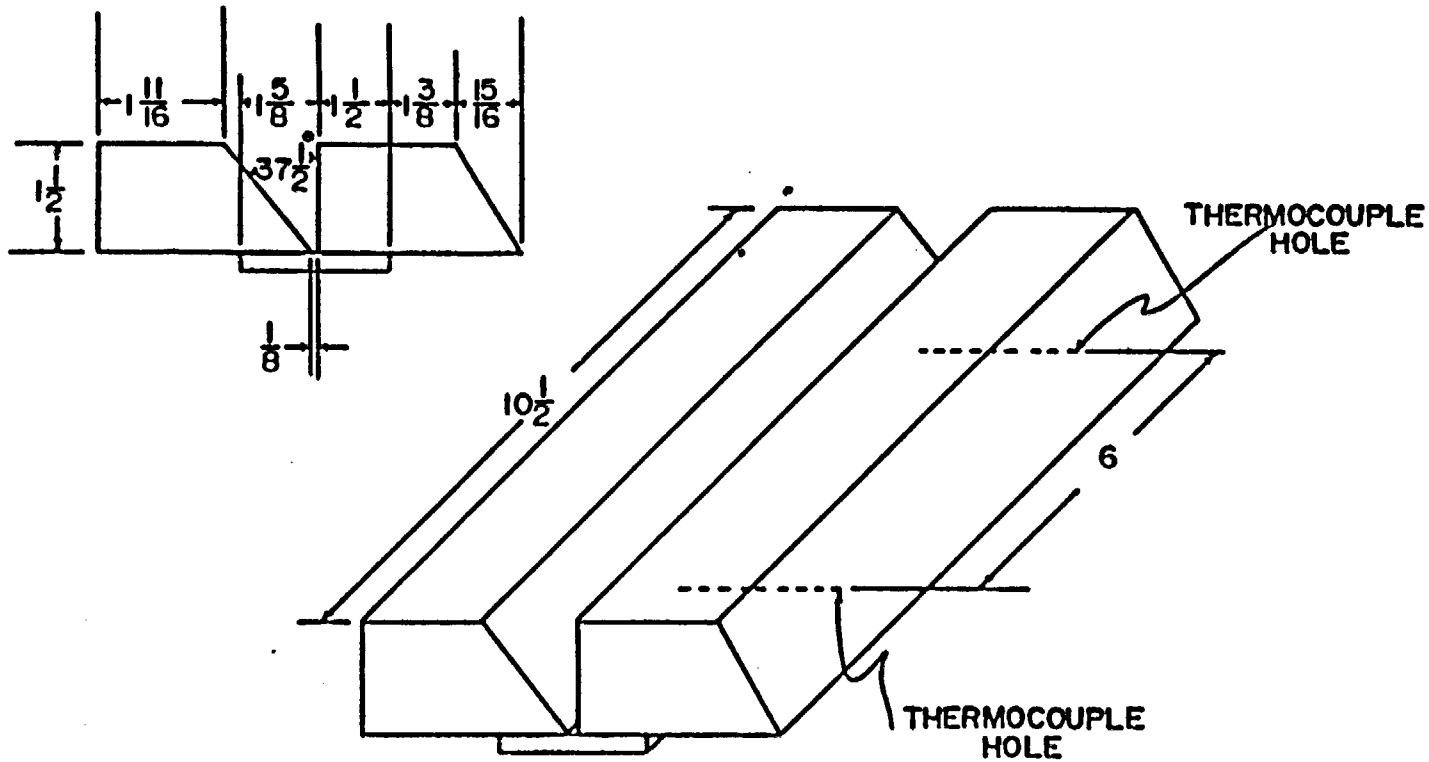

Figure 17. Weld joint configuration for the submerged arc welding process.

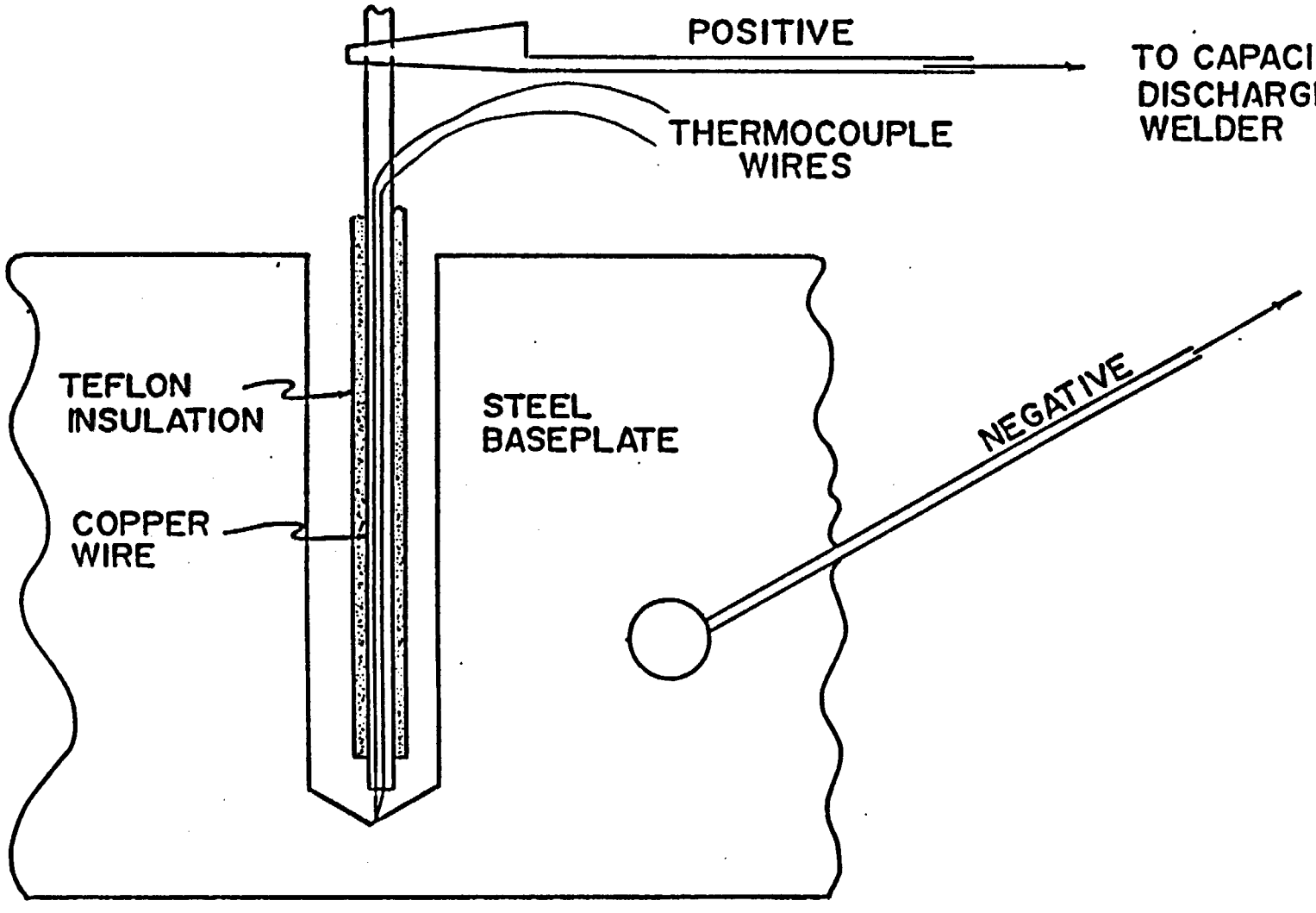

Figure 18. The down hole welding process for welding thermocouples in the bottom of a hole (21).

protector tube was cemented in place using an MgO refactory mix and the wires were connected to a type R junction box.

A type R numatron digital thermocouple monitor was calibrated using a constant voltage generator and readings were adjusted to correspond with tabulated standards (22). The numatron was then connected to the type R junctions of the weld-plate and used to insure proper wire polarity.

Before any thermocouple measurements were made, an evaluation of the parameters which affect the measurements of the temperature device used for this study was carried out.

The following considerations were assessed: thermal gradient across the hot junction; response time of the wires and hot junction; calibration and precision of the equipment used; and conversion from voltage-time to temperature-time.

Since the heat affected zone in this investigation is 3 mm in width the hot junction must be as small as possible to avoid any thermal gradient across it. A thermal gradient of 150°C is not uncommon in weld thermal cycle measurements (23). The hot junction was kept to

0.25 mm to eliminate any error caused by the dimensions of the hot junction. The response times of the 0.005 inch (0.127 mm) diameter thermocouple wires were calculated using guidelines set forth in literature (24). The theoretical response time for the thermocouples used was 0.0012 seconds for 0.005 inch (0.127 mm) wire, however the hot junction was 0.010 inches (0.254 mm) in diameter making the response time 0.0035 seconds.

At a 500°C/sec. heat up rate, typical for submerged arc welds an error of 1.75°C was possible in the peak temperature. The thermocouple reliability as determined from the ASTM manual (25) on the use of thermocouples was +/- 3.75°C between 538°C and 1482°C making a total cummulative error of +/- 5.50°C with just the system configuration. Due to the fine diameter of the thermocouple wire care was taken not to strain or damage it during installation making the quoted calibration invalid.

A Nicolet 4094 digital recording oscilloscope, which is a high response time instrument, was used to gather the voltage-time data from the thermocouples. In instruments designed for faster response, other desirable features have been sacrificed. The Nicolet 4094 is no

exception. The sensitivities are lower, and thus an amplified signal is better suited for measurements of this kind (23).

An isolation amplifier was placed in the circuitry to amplify the thermocouple signal. The amplifier is groundless, and as such, it filters any induced eddy currents or stray voltages caused by the welding process (26). Also in the thermometry circuit was a cold junction compensator necessary in all temperature measurements of this kind.

In combination with the errors previously described, and the amplification circuitry it was possible to have a 5.50°C error. This error, however, is constant, and as a result it only leads to an inaccurate position calculation in the placement of the thermocouple.

The Nicolet 4094 digital recording oscilloscope was used in combination with an integrated circuit isolation amplifier, and cold junction compensator to monitor heat affected zone thermal cycles. Two isolation amplifiers were calibrated by using a constant voltage generator and adjusted according to standard tables (22). The Nicolet 4094 (with the amplifiers and compensators connected) and the numatron were attached to a type R thermocouple in a

furnace and checked to see if their readings were consistent. The Nicolet 4094 was then connected through the isolation amplifier and cold junction compensator to the weld mounted type R junction and a setting of 0.3 ms/point was set on the scanner. Two thermocouple holes per weld were monitored with the oscilloscope/amplifier combination, using the two available channels on the Nicolet 4094. The complete set up is diagramed in Figure 19.

2.8 SUBMERGED ARC WELDING

Submerged arc welding was carried out on 1.5 inch (38.1 mm) weld plate from heat NRC-3, 4, 5, 8, 9, 10, 11, 12, 13, 14 and 15 using a Hobart RC 500, 500 ampere, direct current, 100 percent duty cycle, constant potential, reverse polarity power supply with remote carriage. The theoretical energy input was maintained at 2.45 MJ/m. A Hewlett Packard two pen analog chart recorder monitored voltage and amperage continuously during welding. A summary of the dial settings and actual readings is in Table VII. Tibor 22, 3/32 inch (2.38 mm) diameter wire, in combination with Oerlikon

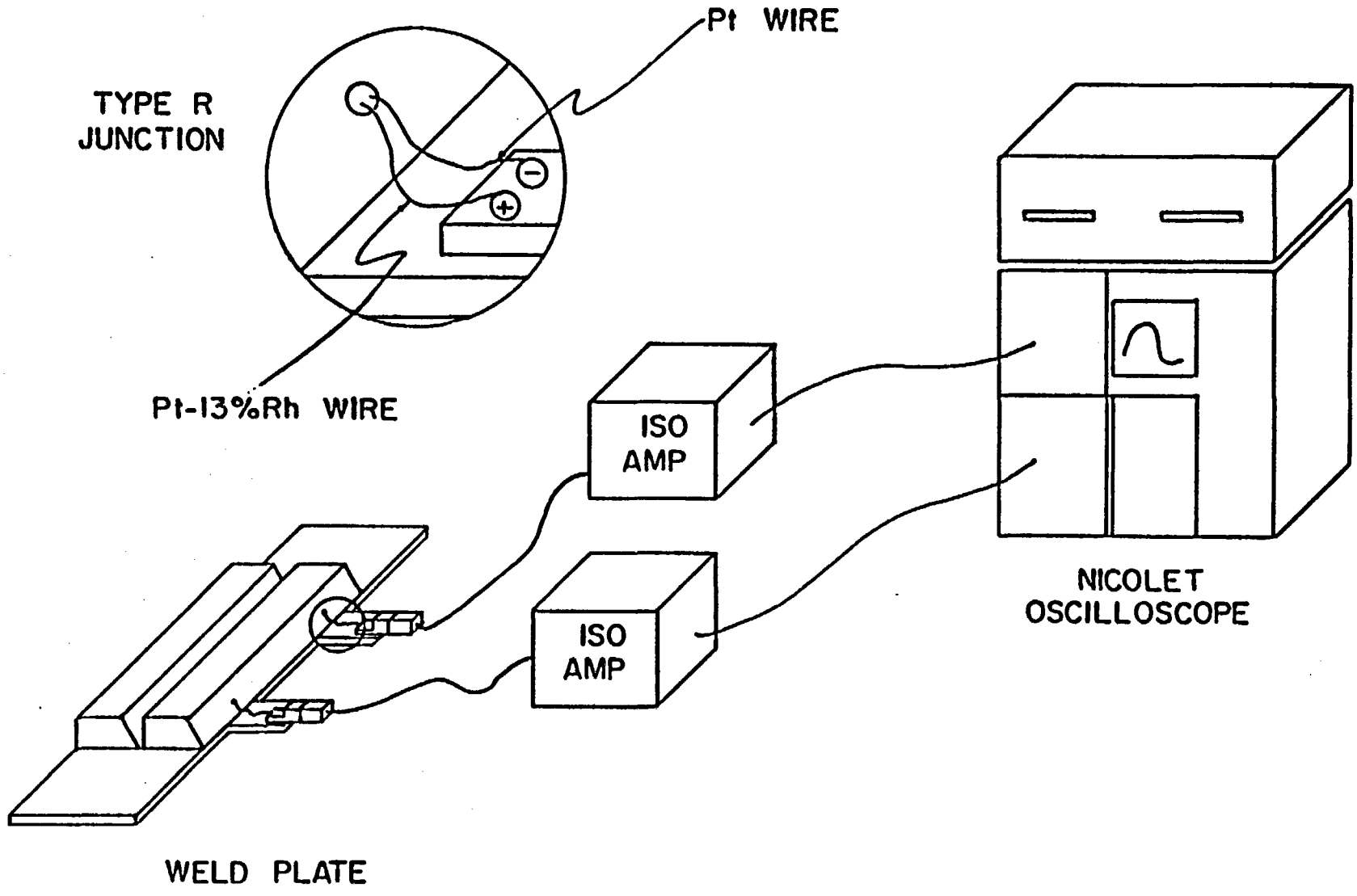

Figure 19. Diagram of the welding set up prior to welding.

Table VII. Welding parameters used to make submerged arc welds on experimental steels.

Weld	Pass	Volts	Amperes	Travel speed (m/s)	Heat Input (MJ/m)
SAW-5-1	root	31.00	496	0.0084	1.83
	2	26.50	474	0.0051	2.47
	3	26.60	476		2.49
	4	26.25	476		2.46
	5	25.75	488		2.47
	6	26.38	476		2.47
	7	26.50	472		2.46
	8	26.25	472		2.44
	9	26.25	468		2.42
SAW-12-1	root	25.50	512	0.0084	1.55
	2	24.75	520	0.0051	2.52
	3	26.00	492		2.51
	4	25.75	496		2.50
	5	25.50	508		2.54
	6	26.00	484		2.47
	7	26.00	486		2.49
	8	27.00	472		2.50
	9	26.50	480		2.49
SAW-14-1	root	35.50	536	0.0084	2.26
	2	36.50	536	0.0051	3.84
	3	35.00	560		3.84
	4	35.00	560		3.84
	5	35.50	556		3.87
	6	35.00	560		3.84
	7	35.00	556		3.82
	8	34.50	560		3.79

Table VII. Continued. . .

Weld	Pass	Volts	Amperes	Travel speed (m/s)	Heat Input (MJ/m)
SAW-15-1	root	24.50	528	0.0084	1.54
	2	26.00	500	NA	NA
	3	24.75	512	0.0051	2.48
	4	26.00	492		2.50
	5	25.50	492		2.46
	6	25.75	496		2.50
	7	25.75	508		2.56
	8	25.00	520		2.55

OP121TT flux was used for welds. The nominal composition of each is shown in Table VIII. A flux depth of 1.25 inches (32 mm) was maintained for each pass. Between passes the flux was removed by hammer and chisel.

2.9 METALLOGRAPHY

After welding, the plates were sectioned transverse to the welding direction, and as close to the thermocouple holes as possible. The sectioned welds were ground to a 240 grit, finish and macroetched with two percent nital to reveal the weld structure. They were sectioned further to isolate the thermocouple hot junction, polished to 0.05 micron finish, etched with a boiling saturated picric acid in methonol with one percent Aerosol OT (27) solution for two minutes to reveal the prior austenite grain size next to the fusion lines, and photographed. The specimens were repolished to remove the picric etch and etched a second time with two percent nital to reveal the structure directly beneath the thermocouple. Photomicrographs were taken for documentation and for later comparison with weld simulated specimens.

Table VIII. Chemical analysis (weight percent) of Tibor 22 wire and Oerlikon OP121TT flux.

Wire	Tibor 22
C	0.059
Mn	1.48
P	0.008
S	0.009
Si	0.04
Cr	0.12
Ni	0.10
Mo	0.26
B	0.01
Nb	0.003
Cu	0.34
Ti	0.03
Al	0.028
O	0.006
N	0.007

Flux*	Oerlikon OP121TT
SiO_2	11
Al_2O_3	17
MgO	32
CaO	7
CaF_2	24
MnO	1
TiO_2	1
Na_2O	1
Fe_2O_3	2

* Nominal Composition

2.10 THERMAL PROFILING

The thermal data stored on disk in the Nicolet 4094 oscilloscope was in voltage-time. The voltage-time data was transmitted to an IBM AT personal computer, and converted to temperature-time using a ninth order polynomial (22) (for the program see Appendix D).

The temperature-time data was filtered by appropriate programming, to print every 10th data point. Each wave was recorded using 7936 points, so some filtering was necessary to handle the numbers (for the program see Appendix D (27)). The printed thermal data was further sorted from 794 points to 50 points manually, to form a representative set of data which were programmed into a Gleeble 1500 for weld heat affected zone simulation.

The temperature-time data obtained from the welding procedure was plotted and an attempt to match these experimental curves with the three dimensional heat flow equations presented by Rosenthal (16) was completed. Supplementary data from the Welding Institute (29) coincided with measured data and it was incorporated into

this phase of the investigation. Modifications to the Rosenthal equations presented by Tsi (30) were investigated and using an empirical modification of his technique a reasonable representation of the thermoprofiles was obtained.

Modifications to the Rosenthal equation for three dimensional heat transport were used to describe the higher peak temperatures that were unable to be measured in the heat affected zone. It is important to describe the origin and use of these modifications, as they are strictly empirical. Rosenthal's equation is listed here again with the variables described previously.

$$T - To = \frac{q/v}{2\pi\lambda t} \exp\left(\frac{-r^2}{4at}\right) \quad \text{(EQ 1)} \qquad (14)$$

The experimental curves show that heating is faster than predicted by Rosenthal and cooling is slower. In order to use Rosenthal equation some modifications were made.

The Rosenthal assumption that material physical coefficients are constant is wrong. As shown in Figure 20, carbon steels have a drastic change in specific heat (31) at 1000°K. This is due to a phase change from fcc

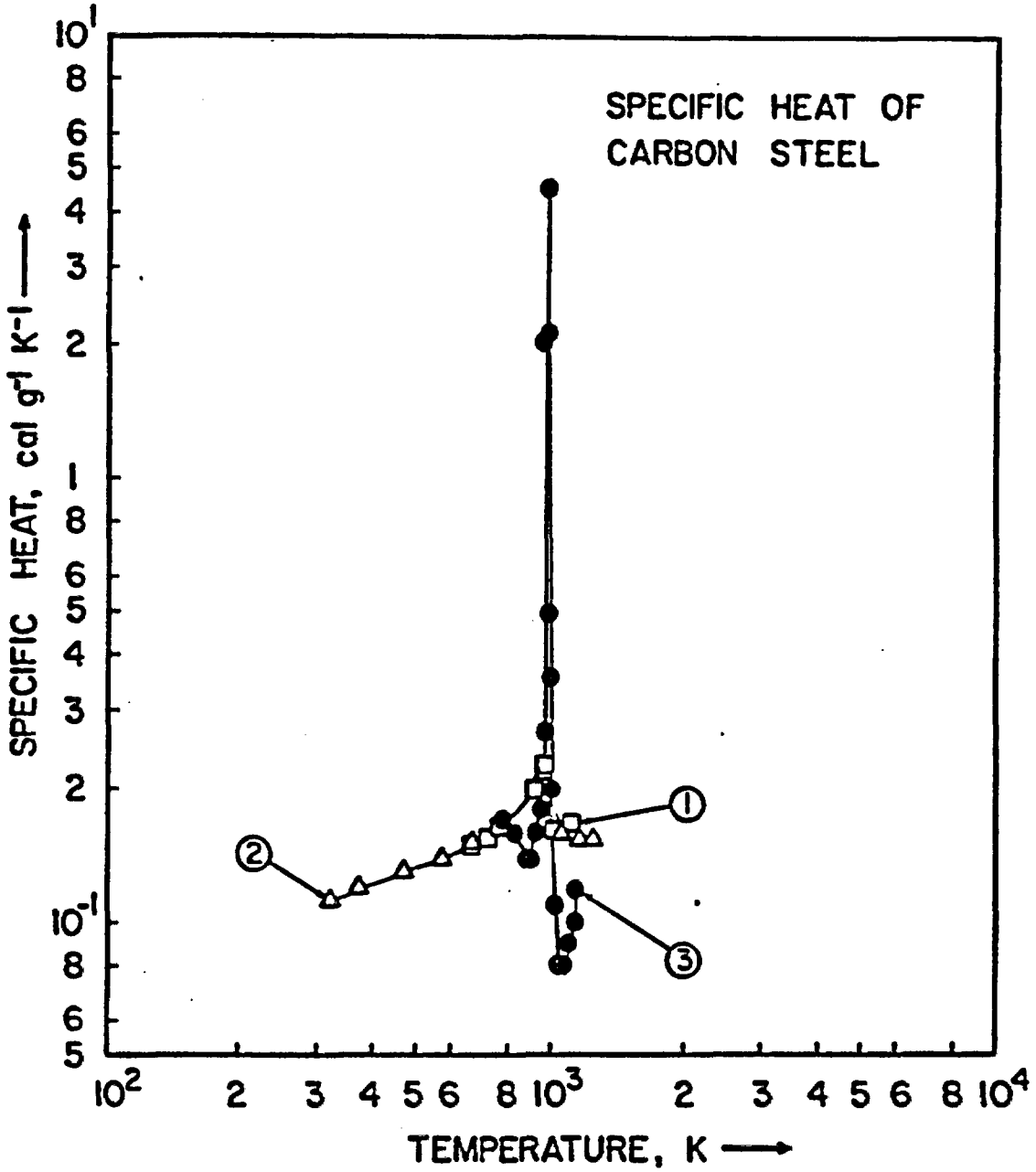

Figure 20. Specific heat for a group of carbon steels (30).

(face centered cubic) austenite to bcc (body centered cubic) ferrite. Thermal conductivity changes with temperature (32) as shown in Figure 21. Density changes also, as expected, when heating steel, but this change is slight. If these variations in thermal properties were incorporated into the Rosenthal equation, it would approach reality, however it could no longer be integrated to its present form and a numerical iterative solution would be needed (16). Numerical approaches such as this, and finite element analysis, as performed by the Welding Institute (29) is beyond the scope of this investigation. Instead an empirical simplistic approach was used to modify the thermal conductivity.

On the heat-up cycle, Rosenthal's equation was too slow, a progressively higher thermal conductivity was inserted until the equation approached the observed. However, on the cooling cycle this increased conductivity would increase the cooling rate and reduced cooling was needed. A second equation which was identical to the first except a progressively lower thermal conductivity was inserted, which slowed the cooling until it matched the observed. Two equations were used, one with a high thermal conductivity for heating, and one

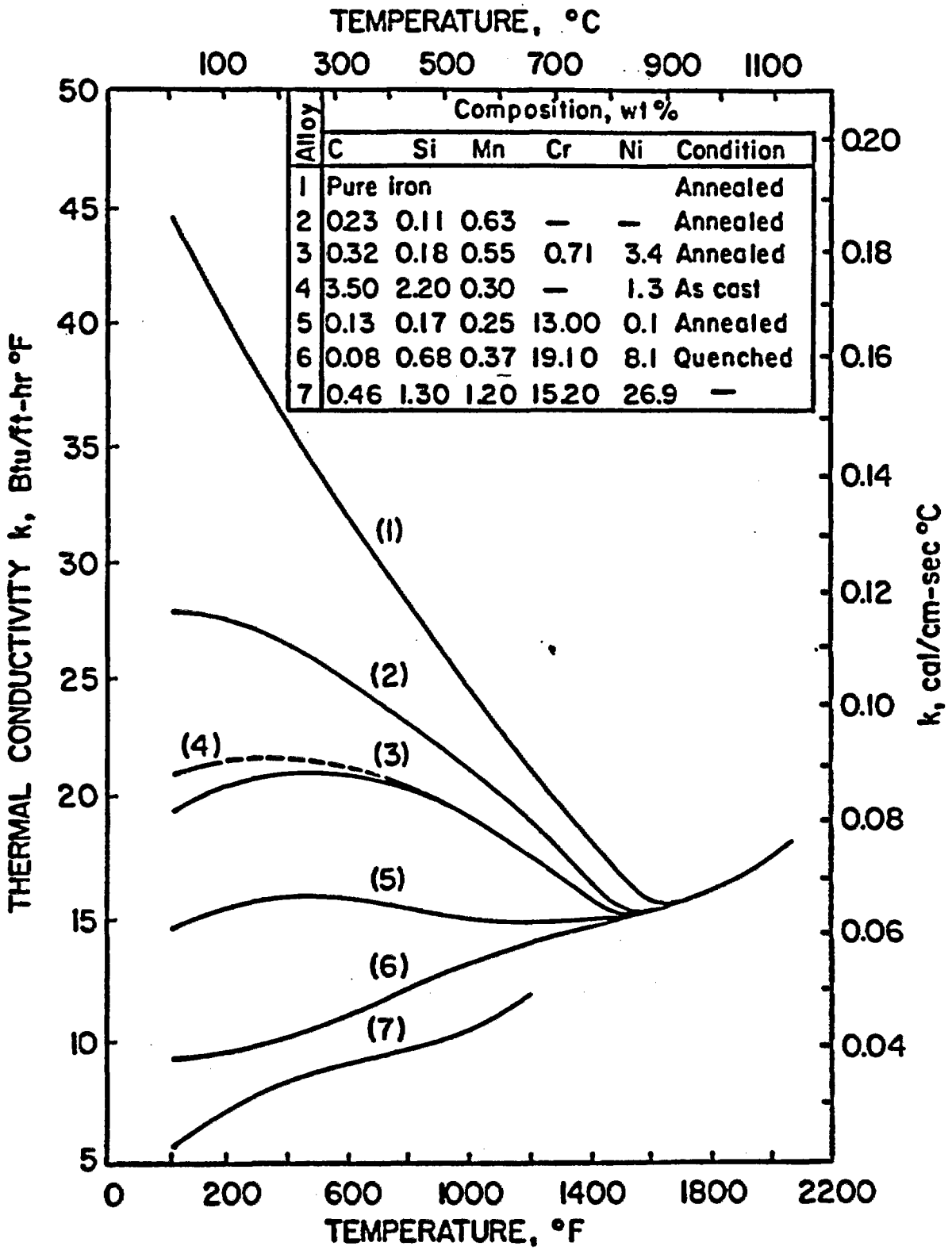

Alloy	Composition, wt % C	Si	Mn	Cr	Ni	Condition
1	Pure iron					Annealed
2	0.23	0.11	0.63	—	—	Annealed
3	0.32	0.18	0.55	0.71	3.4	Annealed
4	3.50	2.20	0.30	—	1.3	As cast
5	0.13	0.17	0.25	13.00	0.1	Annealed
6	0.08	0.68	0.37	19.10	8.1	Quenched
7	0.46	1.30	1.20	15.20	26.9	—

Figure 21. Changes in thermal conductivity with temperature for a variety of steels.

with a low thermal conductivity for cooling. The curves MR11092, MR111 and MR1111 are these modified equations plotted, along with the experimental curves, 15W12, 14W11, 12W10, 12W9 and the Welding Institutes curve WI-1 in Figure 22.

The curves shown in Figure 22 were programmed into the Gleeble 1500 weld simulator and used for heat affected zone modelling of steels from heat NRC-5, NRC-12, MRC-14 and NRC-15.

2.11 GLEEBLE SIMULATION

Twelve specimens from each heat, NRC-3, 5, 12, 14 and 15, were machined from the specially normalized Gleeble plate to 0.250 inch (6.36 mm) diameter, 4 inch (102 mm) long cylindrical specimens for use in the Gleeble 1500.

The machined samples were mounted in the Gleeble thermo-mechanical weld simulator. The span between the jaws was kept constant at one inch (25.4 mm). On samples where the peak temperature was below 1200°C a type K thermocouple was welded to the specimen to monitor the induced thermal cycle. Above 1200°C a type R

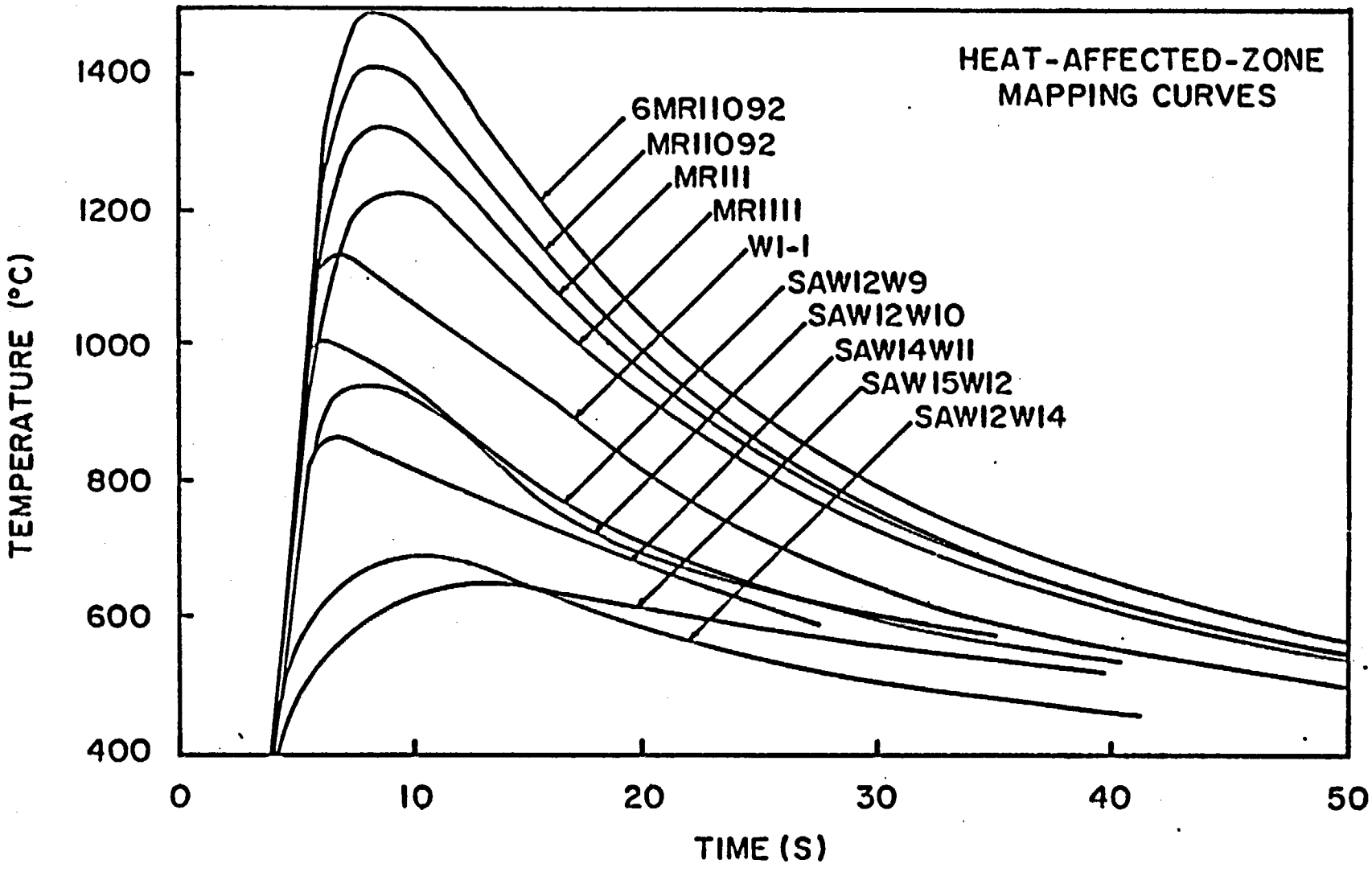

Figure 22. Experimentally measured and analytically derived thermal profiles describing specific areas in the heat affected zone.

thermocouple was used. The thermoprofiles were recorded on an analog chart recorder which is part of the Gleeble 1500 unit. On samples where peak temperatures were below 1000°C the full scale setting on the chart recorder was one volt (1000°C full scale). Above 1000°C the full scale setting was two volts (2000°C full scale). The chart speed was 40 cm/min. with the coordinate setting on Y-vs-t. After thermal cycling the Gleeble specimens were sectioned directly beneath the thermocouple hot junction and polished to an 0.05 micron Al_2O_3 finish. All specimens were etched in two percent nital and photographed. Specimens where the prior austenite grain boundaries were not decorated with allotriomorphic ferrite, were repolished and etched with saturated picric acid in methanol with one percent Aerosol OT and again photographed. The microstructures were compared to the microstructures of the actual welds and the Gleeble 1500 was evaluated as a tool to model heat affected zone microstructures on cast steel. In addition, the microstructures generated by the Gleeble were examined to find microstructural differences caused by cleanliness and alloy chemistry between samples.

3.0 RESULTS AND DISCUSSION

The various manufacturing processes used to fabricate cylindrical overpack containers were discussed at the beginning of this thesis. Two processes, static casting and centrifugal casting were examined as manufacturing techniques. The variables that affected the as-cast microstructures emphasized the advantage of centrifugal casting as the manufacturing technique best suited for cylindrical overpack container production. The results of the experiments to verify the effects of alloy chemistry, cleanliness, initial solidification processing, heat treating, and welding on the microstructure of centrifugally cast steels are discussed here. The results of weld thermal cycle simulation on a Gleeble 1500 to produce samples large enough for mechanical testing are discussed as well.

3.1 STATIC CASTING

Large static castings of the dimensions of the overpack container will generally have a region of columnar solidification and a region of equiaxed

solidification. Columnar solidification is characterized by a degree of undercooling at the solid/liquid interface of a solidifying melt. The nucleation of solid is at the mold/metal interface and preferential growth along the <100> crystallographic direction predominates (33). Equiaxed solidification is typified by long solidification times with little or no thermal gradient present. Nucleation occurs in the bulk liquid yielding an equiaxed structure. This region generally occurs at the center of large "chunky" castings and is the last metal to solidify.

The two furnace solidified specimens T-1 and T-2, used to model statically cast overpack containers, were cooled at 0.5°C and 2.0°C per minute respectively; and examined metallographically to reveal secondary dendrite arm spacing as a function of solidification time. Equiaxed solidification occurred in both castings as shown in Figure 23. No secondary dendrite structure was seen in T-1 and thus no measurement was made. However, T-2 revealed the beginning of a secondary dendrite arm structure which prompted a normalizing treatment. (Normalizing did not change the initial solidification structure, but merely enhanced the segregated

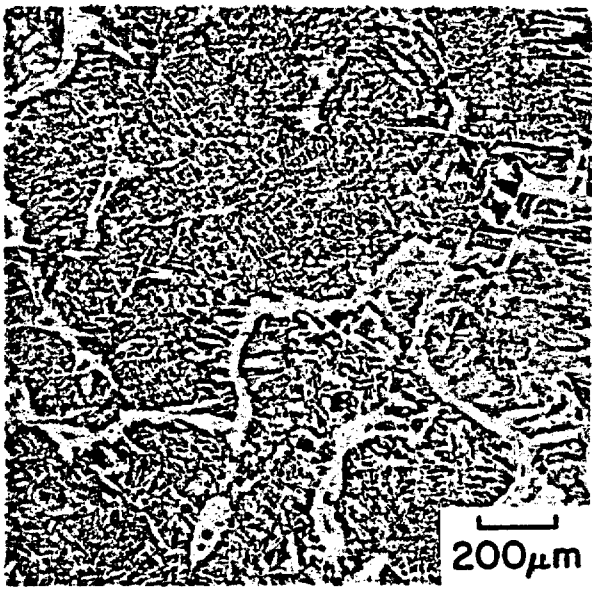

T1

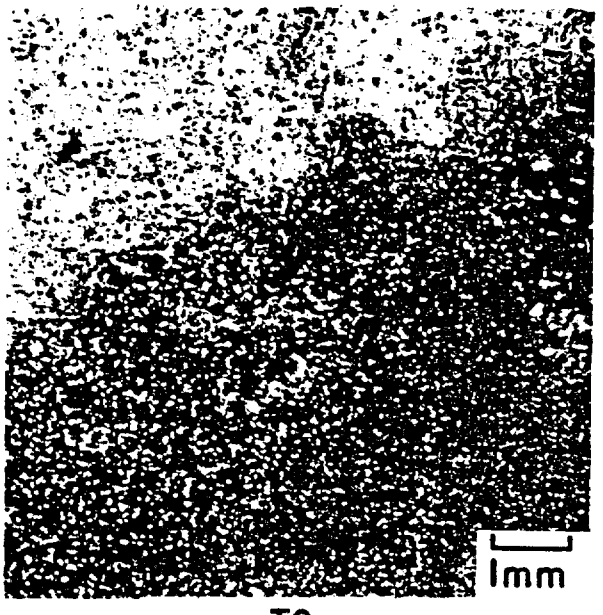

T2

Figure 23. Photomicrographs of the furnace solidified specimens T1 and T2. T2 shows the beginning of secondary dendrite arms. 2% nital etch.

interdendritic regions). The measured arm spacing was 970 microns and followed the diagram of Figure 10, which shows secondary dendrite arm spacing as a function of solidification time.

The effects of alloy content and cleanliness on microstructure and properties was not evaluated for these two steels, as static casting was eliminated as a viable manufacturing technique for overpack containers. The secondary dendrite arm spacing measurements were carried out only to determine if the experimental technique was successful. For completeness, the chemical analysis of T-1 and T-2 is shown in Table IX. The remainder of this discussion will address the effects of alloy content and cleanliness on the microstructure and properties of centrifugal castings.

3.2 CENTRIFUGAL CASTING

Nineteen heats of steel were cast into grey iron ingot molds. Each heat yielded two one inch (25.4 mm) thick plates and one 1.5 inch (38.1 mm) thick plate which provided specimens for welding and metallographic analysis which typify centrifugal castings. The 1.5 inch

Table IX. Chemical analysis of statically cast experimental steels, before and after casting.

	%C	%Mn	%Si	%S	%P	%Al
T1 before casting	0.17	0.85	0.20	0.025	0.01	0.02
T1 after casting	0.15	0.15	0.10	0.02	0.01	0.01
T2 before casting	0.17	0.85	0.20	0.025	0.01	0.02
T2 after casting	0.16	0.17	0.39	0.04	0.01	0.01

(38.1 mm) thick plate and one inch (25.4 mm) thick plate were normalized as described in the experimental procedure. The as-cast, and normalized one inch (25.4 mm) plates were examined for: compliance to the ASTM A-216 grade WCA specification, inclusion distribution, phase identification, the effects of cleanliness and alloy content on microstructure, and secondary dendrite arm spacing. The 1.5 inch (38.1 mm) thick normalized plate was welded; monitoring heat affected zone thermal cycle, sectioned, and examined metallographically to determine the effects of alloy and cleanliness variations on heat affected zone microstructure. Upon completion, the effects of welding and casting process variables on the microstructure and properties of ASTM A-216 grade WCA steel was determined. The chemical analyses for the 19 heats cast are shown in Table IV. Since NRC-5, NRC-12, NRC-14, and NRC-15 best match the target alloys A, B, and C of the aforementioned specification, they will be the subject of this discussion. The other heats will be the subject of future work and may be mentioned only on occasion during the duration of this thesis.

Figure 24 shows micrographs of the as-cast structures. The experimental steels do match the

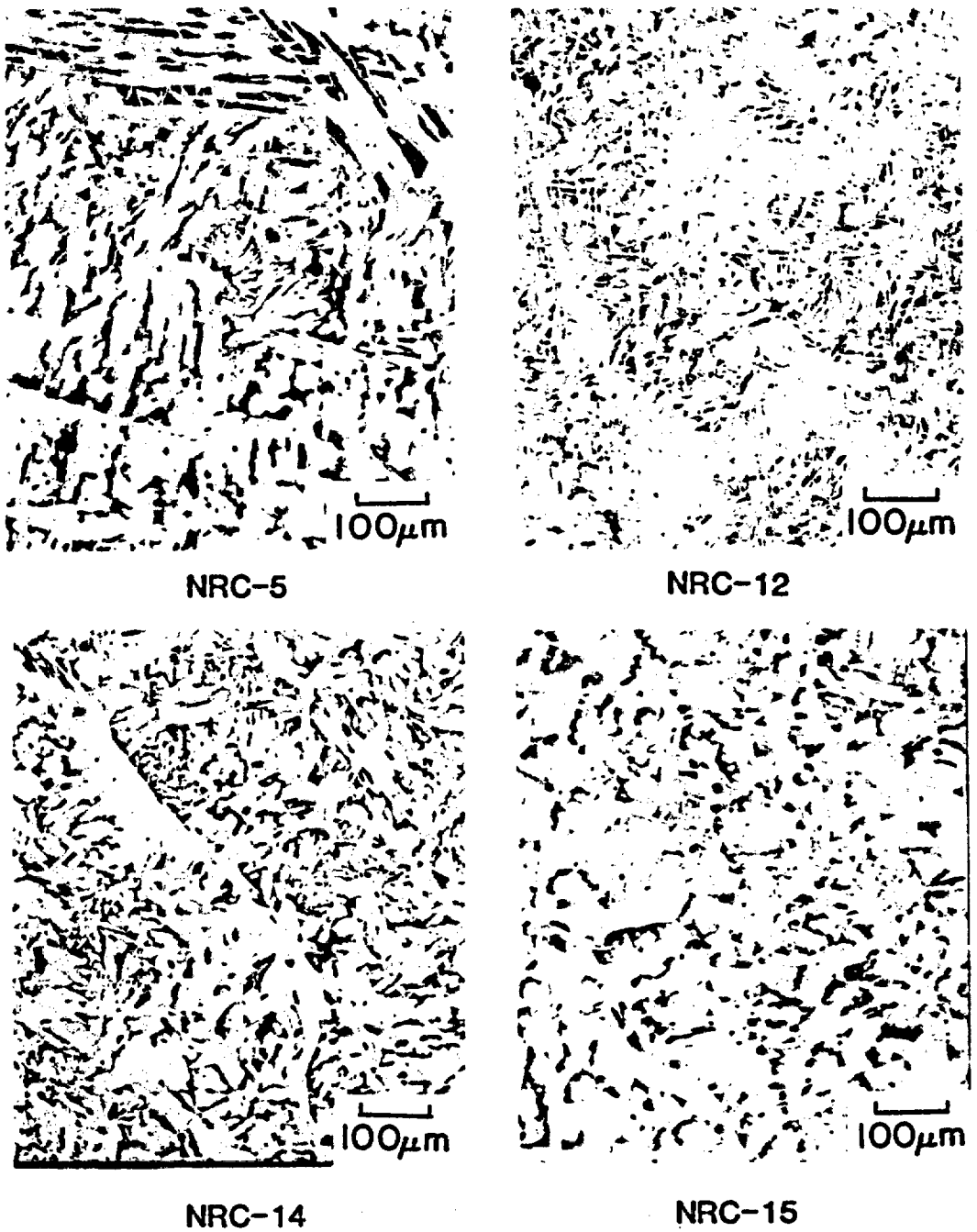

Figure 24. Photomicrographs of the four steels used for this study, shown in the as-cast condition. 2% nital 100x.

microstructure of ASTM A-216 grade WCA steel, showing elongated ferrite grains (white) with islands of pearlite (black). (Note: the pearlite volume fraction appears to change from specimen to specimen; however, sectioning differences and small changes in carbon content account for this.)

Specimens were polished to a 0.05 micron finish and examined optically in the unetched condition. Micrographs in Figure 25 show the observed structure. NRC-5 has 114 ppm oxygen and 0.01 weight percent sulfur so the inclusions shown are primarily $MnSiO_2$, Al_2O_3, and MnS as the scanning electron microscope analysis shown in Table X reveals. NRC-12 has 165 ppm oxygen and 0.01 weight percent sulfur, and shows a higher oxide inclusion volume fraction than does NRC-5. NRC-14 has 218 ppm oxygen and 0.045 weight percent sulfur and has the highest inclusion volume fraction of the steels studied. NRC-15 with 0.01 weight percent sulfur and 60 ppm oxygen has the lowest non-metallalic inclusion volume fraction of all.

Figure 24 indicates that neither the inclusion counts nor the chemical variations in silicon, manganese,

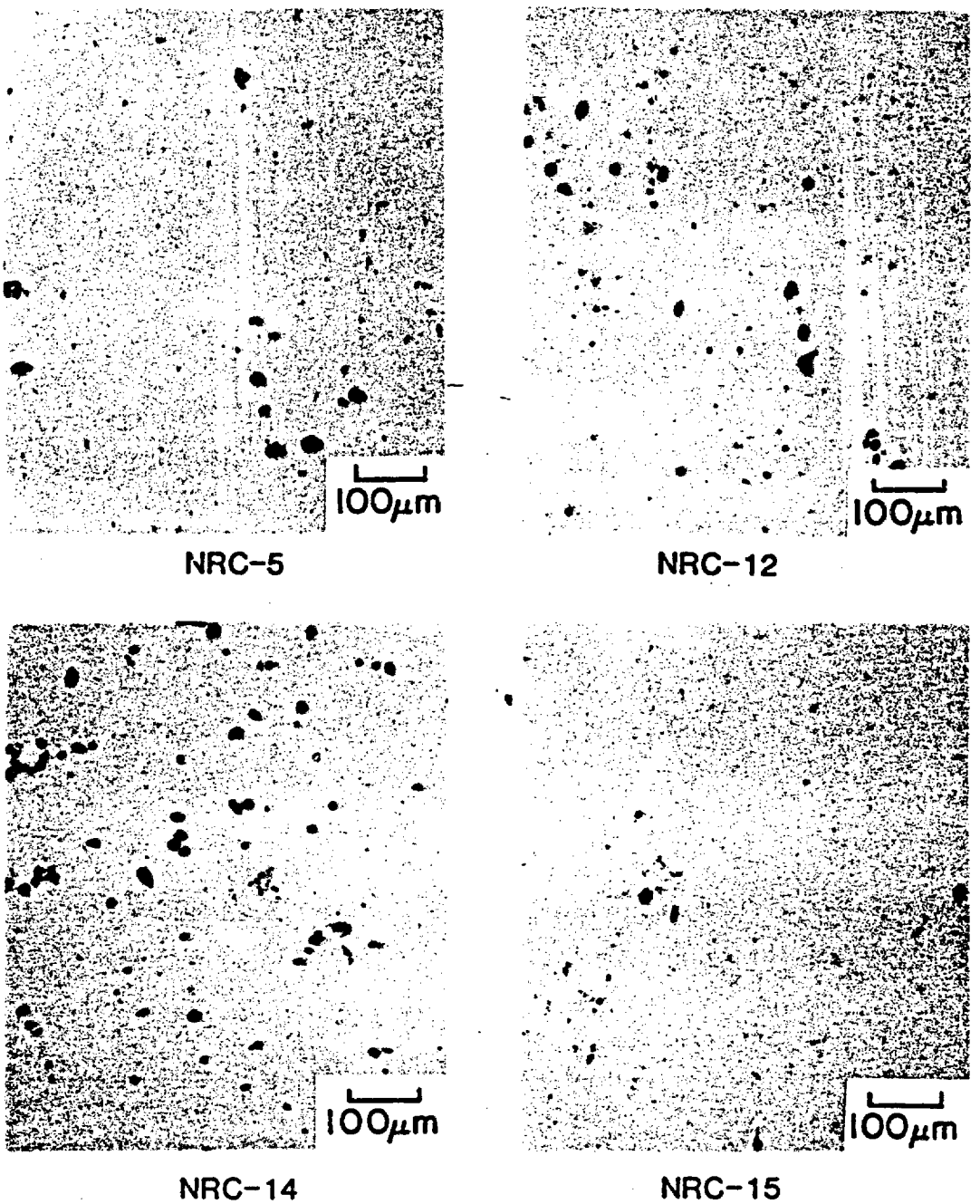

Figure 25. Photomicrographs of the four steels used in this investigation depicting the nonmetallic inclusions. Unetched 100x.

Table X. Scanning electron microscopy summary of inclusion identification and area fraction.

Sample	Area Fraction MnS (X10000)	Area Fraction* Oxide (X10000)
NRC-5	6.10	2.10
NRC-14	11.50	40.50
NRC-12	3.31	5.46
NRC-15	4.62	5.14

*Includes Al_2O_3 and $MnSiO_2$ combined

aluminum, sulfur or oxygen have a significant influence on the as-cast ingot microstructures.

The normalizing treatment is part of the manufacturing process prior to delivering the overpack container to the customer; therefore, effects of normalization on grain size and the effect of chemical variations, and inclusion distributions on the normalized microstructure must be assessed.

Normalizing is used to produce a uniform microstructure, refine the grain size, and to relieve residual stresses. This treatment brings the steel into the austenite phase, but is sufficiently low in temperature to prevent undesirable grain growth. Upon air cooling, the austenite transforms to equiaxed ferrite/pearlite. The room temperature ferrite grain size is a function of time and temperature spent in the austenite phase, and cooling rate from the austenite phase to room temperature, hence low austenitizing temperatures (900°C for AlSl 1018 steel) are used for normalizing treatments.

Standard normalizing treatments are; austenitize for one hour per inch (25.4 mm) of thickness, and air cool. For a typical 6 inch (152.4 mm) overpack container, this

procedure is; austenitize at 900° for three hours and air cool. A standard normalizing treatment for the experimental steels is; austenitize at 900°C for one hour and air cool. As expected, the 6 inch (152.4 mm) thick section has a larger room temperature ferrite grain size than the one inch (25.4 mm) section, due to the longer austenitizing temperatures, and slower cooling times as shown in Figure 14.

The modified normalizing treatment used in this study; austenitize at 1050°C for two hours and slow cool resulted in the structures shown in Figure 26. Comparison of these structures to actual heavy section castings, Figure 13, shows that the experimental modified normalizing treatment, indeed, produced structures typical of industrial castings. A summary of the grain sizes for the steels in Figure 26 and those in Figure 13 are in Table XI.

After normalizing, the secondary dendritic structure became visible and was measured to be 50 microns using linear intercept techniques. This spacing corresponds to a solidification cooling rate of 500°C per minute as seen in Figure 10. The secondary dendrite arm spacing (DAS) can be used as a tool to assess the effects of

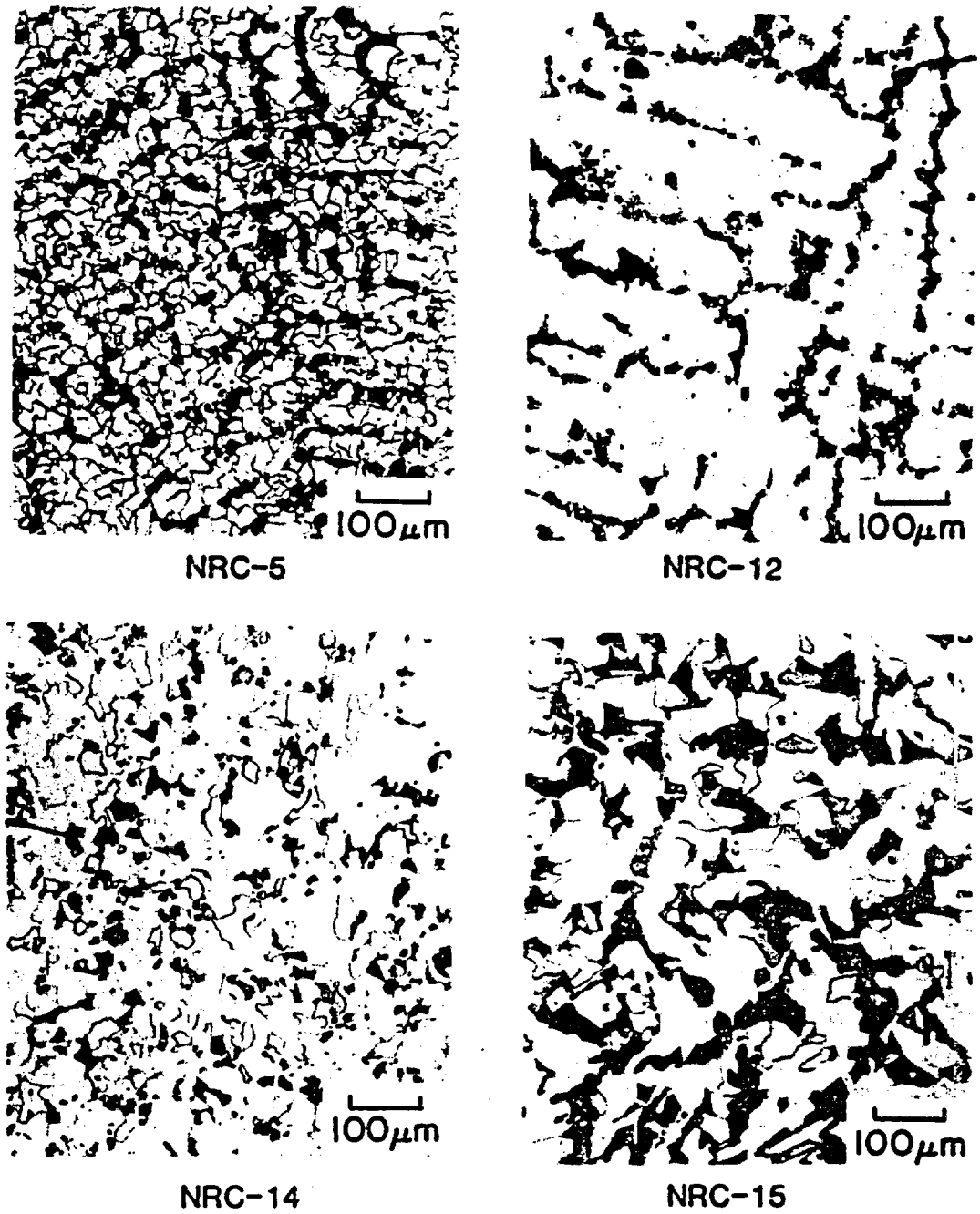

Figure 26. Photomicrographs of the experimental steels, in the normalized condition, showing typical ferrite/pearlite structure. 2% nital 100x.

Table XI. Summary of grain sizes of experimental steels and steels analyzed from Volume 7 Eighth Edition of the ASM Metals Handbook.

SPECIMEN	GRAIN SIZE (microns)
NRC-5	34
NRC-12	40
NRC-14	45
NRC-15	65
VOL. 7 (1")	22
VOL. 7 (3")	36
VOL. 7 (6")	41

microsegregation and macrosegregation on mechanical and corrosion behavior of overpack materials. The 1000 micron secondary DAS in the slowly solidified specimen and the 50 micron secondary DAS of the chill cast steels show that it is possible to determine the solidification rate by metallographic techniques alone. This visual and relatively easy to acquire information can represent a tool for quality assurance. The quantification of dendritic segregation effects on the mechanical and corrosion behavior is beyond the scope of this work. It should be noted that these segregation affects will play a role in container performance and that future work should address that fact on a quantitative basis.

Up to now the effects of alloying and cleanliness on overpack microstructure has shown little significance.

Optical microscopy revealed that no microstructual differences exist between the four steels due to the alloy and cleanliness modifications for the casting and normalizing manufacturing processes.

Welding is the final fabrication process of the overpack container prior to burial and, as such, an examination as to how the alloy and cleanliness

modifications influence the weld heat-affected-zone microstructure is warranted.

3.3 WELDING

In most welding processes, the weld metal microstructure can be controlled through selection of proper electrode and shielding combinations. The heat-affected zone in the basemetal, on the other hand, shows a wide variety of microstructural changes which depend on: welding energy input, base plate composition, inclusion type and distribution, and preweld and postweld heat treatments.

The heat affected zone in steel is usually divided into four sections: the grain growth region, closest to the fusion line which sees temperatures above 1100°C; the grain refined zone or recrystallized zone, next to the grain growth zone which sees temperatures between 1100°C and 900°C; the partially transformed zone, next to the grain refined zone with temperatures between 900°C and 750°C; and the zone of spherodized carbides, or tempered zone, which is furthest away from the fusion line and sees temperatures in the 750°C to 700°C range (14).

Figure 27 shows a schematic of the four zones with respect to distance from the fusion line, and their relation to the iron-iron carbide phase diagram. This diagram will serve as a tool for qualitative examination of the microstructures obtained during the welding process. Figure 28 shows micrographs of these four zones taken from an off-chemistry weldplate used to adjust the welder. It is typical of the structures that were seen in the actual experimental welds, although the chemical and inclusion variations of the experimental steels altered the zones as will be described later.

Eleven plates of the dimensions shown in Figure 17 were submerged arc welded using thermocouples to monitor the heat affected zone thermal experience. Welds SAW-5, SAW-12, SAW-14, and SAW-15 were made on normalized steel from heats NRC-5, NRC-12, NRC-14, and NRC-15, respectively, and were sectioned transverse to the welding direction, and as close to the thermocouple as possible, to reveal the position of the thermocouple hot junction (Figure 29). The welding parameters are shown in Table VII. Further sectioning and subsequent etching revealed the microstructure directly beneath the thermocouple. Photomicrographs of these areas were taken

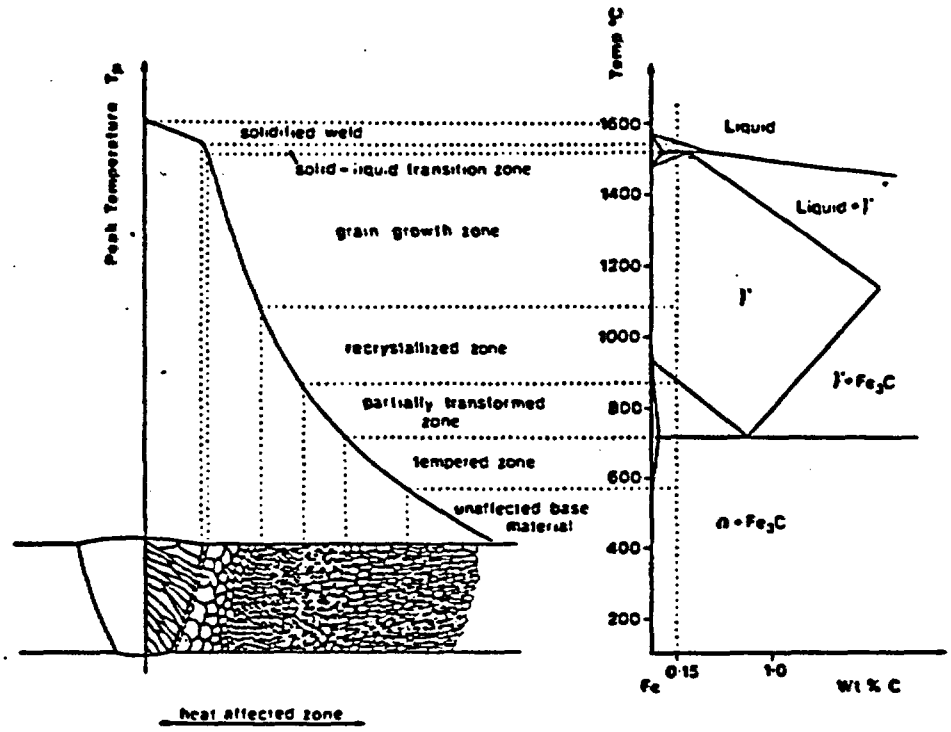

Figure 27. A schematic diagram of the various sub zones of the heat affected zone, corresponding to the alloy C_o (0.15 wt. %C). (14)

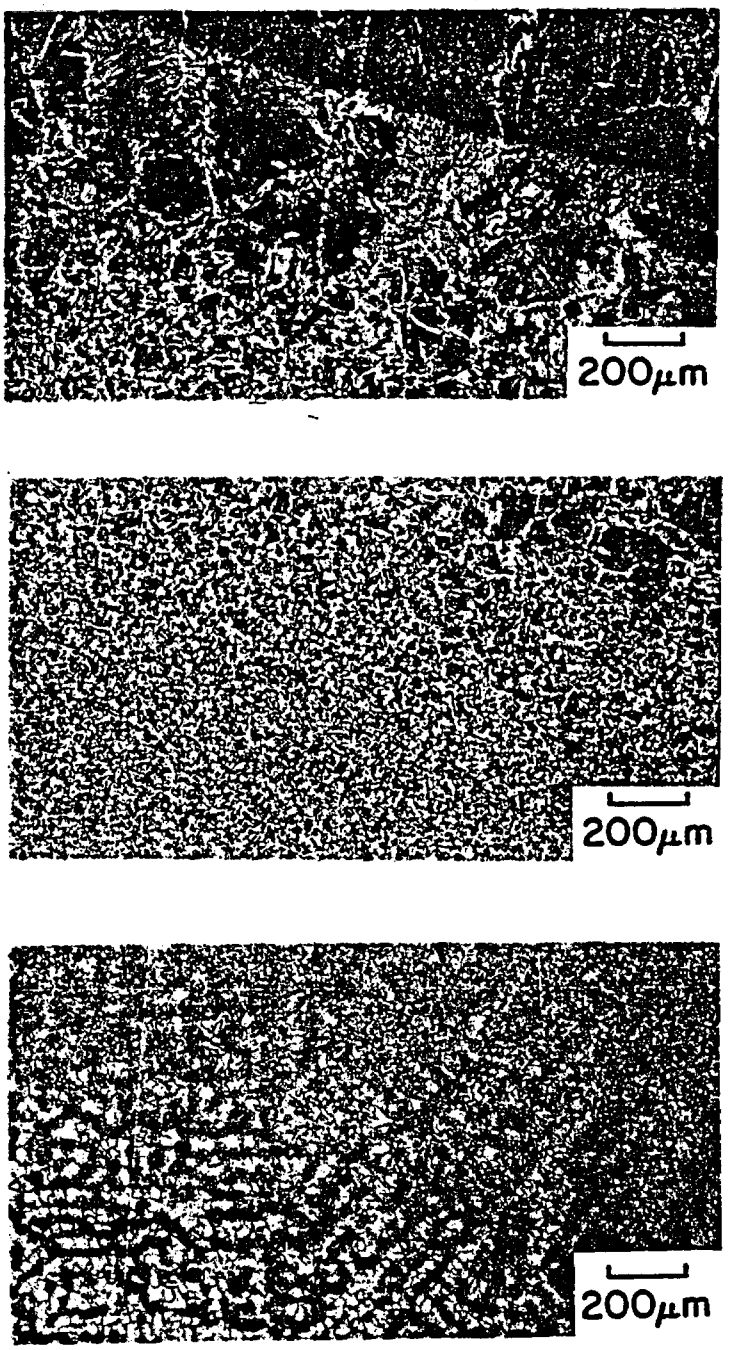

Figure 28. Photomicrographs of the four heat affected zone subzones in an off chemistry experimental weldment. The top micrograph shows the fusion line and grain growth region, the middle is recrystallized zone, and the bottom shows the partially transformed zone and tempered zone. 2% nital 50x.

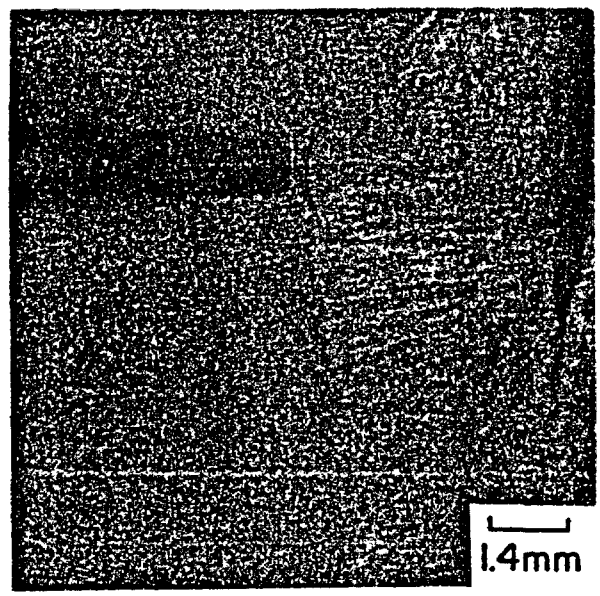

NRC-9

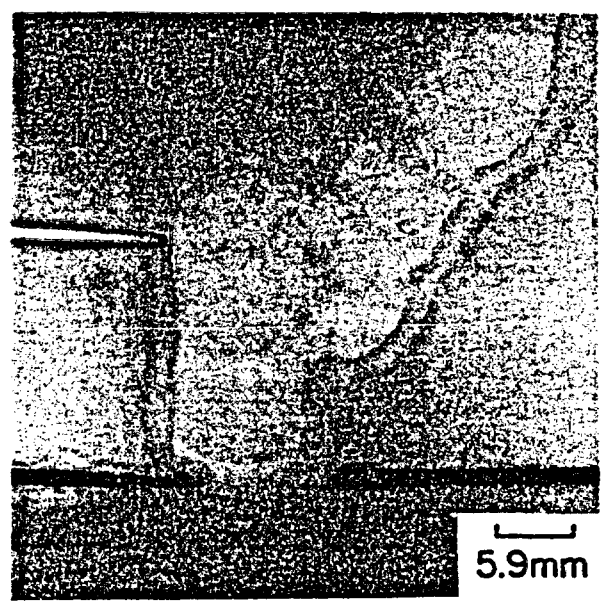

NRC-9

Figure 29. Photomicrographs showing typical thermocouple placement for thermal cycle measurements.

for comparison with the measured thermal experience. The thermal data was compared to the photomicrograhs taken below the thermocouples and evaluated using a continuous cooling transformation diagram for AISI 1018 steel (34) (Figure 30) and the diagram in Figure 27.

Figure 31 shows the microstructure directly beneath the hot junction of one of the thermocouples in SAW-15, along with the measured thermal experience that generated that structure. The weld joints took between 9 and 10 passes to fill, and the thermocouples measured the effect of all ten passes during the welding cycle. The curves shown in Figure 31 are the result of three of the welding passes that raised the temperature of the region being monitored to critical values. No significant microstructural changes occur for weld passes where the peak temperature is less than 600°C, so the curves for those weld passes were omitted.

The microstructure can be evaluated qualitatively by using the diagram of Figure 27 and the measured thermal experience. Curve SAW-15W7 of Figure 31 shows a peak temperature of 1028°C which according to Figure 27 should yield a fine grained microstructure. During heating, the ferrite to austenite transformation does not

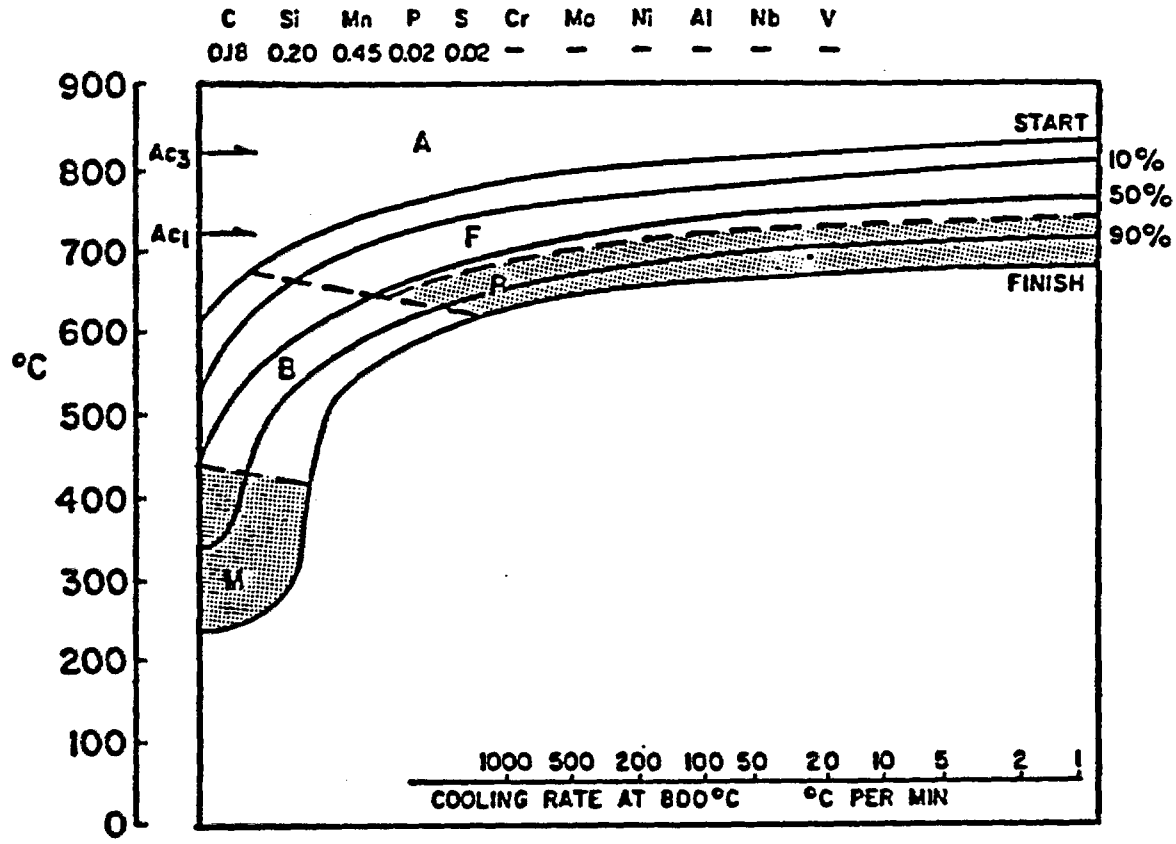

Figure 30. Continuous cooling transformation diagram for AISI 1018 steel (35).

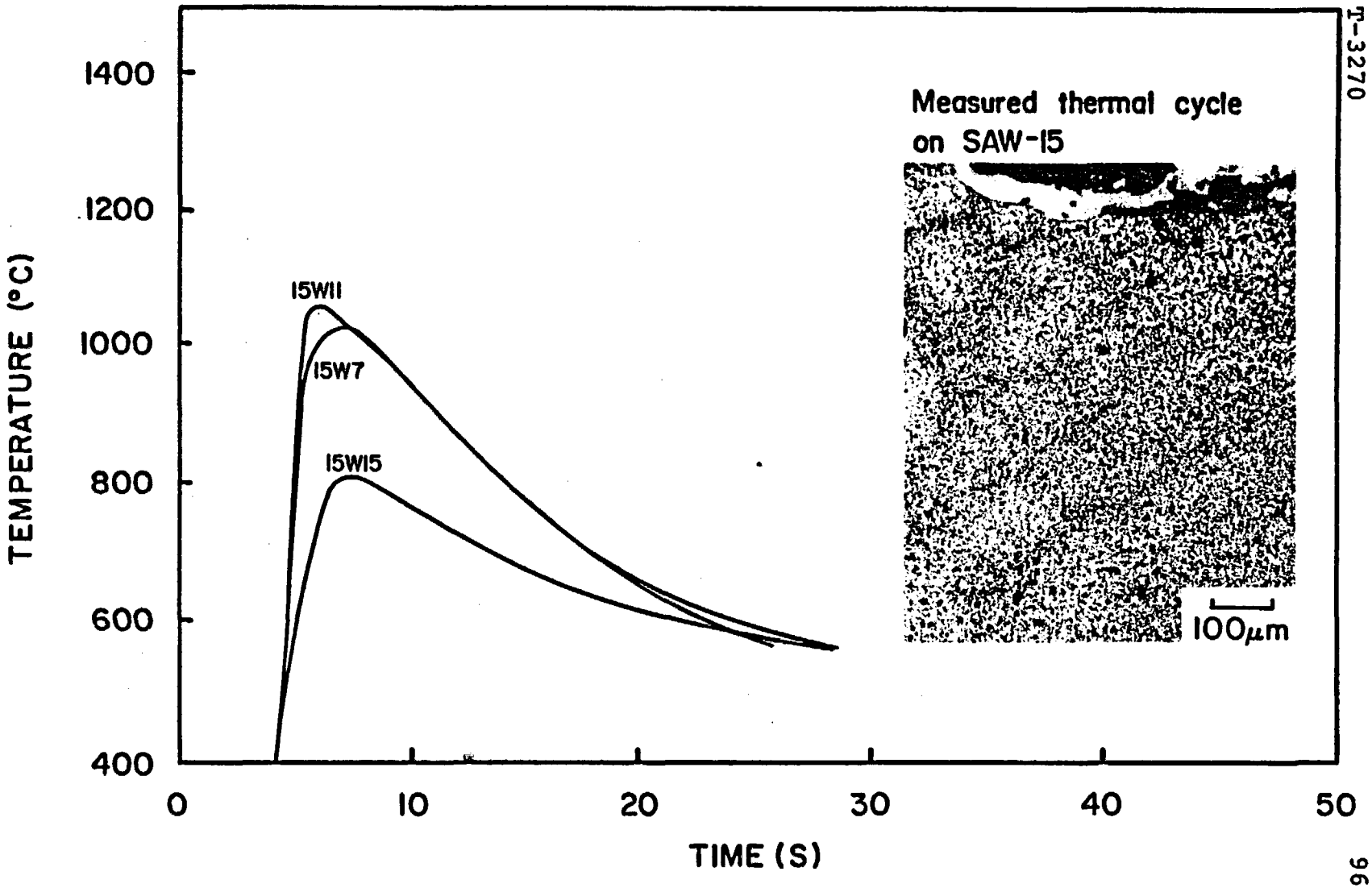

Figure 31. Thermal cycles measured from SAW-15, along with the associated microstructure showing fine equiaxed ferrite (white)/pearlite (black) typical of a recrystallized HAZ subzone.

have time to develop properly, the carbides may not fully dissolve, and the grain size remains small. The austenite to ferrite transformation on cooling produces a fine grained ferrite/pearlite structure (14). The next thermal cycle this region sees is depicted by curve SAW-15W11, which shows a peak temperature of 1060°C. This, too, is in the grain refined zone and yields a slightly more refined structure. The next measured thermal cycle SAW-15W15 shows a peak temperature of 815°C and is in the partially transformed region. The refined pearlite, from the previous two passes quickly austenitizes because of its lower ferrite to austenite transformation temperature. Upon cooling, the austenite to ferrite transformation yields pearlite. The structure is still refined and shows equiaxed ferrite/pearlite.

Figure 32 shows a micrograph from SAW-14 with the thermal experience that generated this structure. SAW-14W7 has a peak temperature of 1037°C which is in the grain refined zone. SAW-14W11 has a peak temperature of 892°C, and is in the partially transformed region. The already refined structure from the previous passes did not change, but the pearlite became more refined on this second heating.

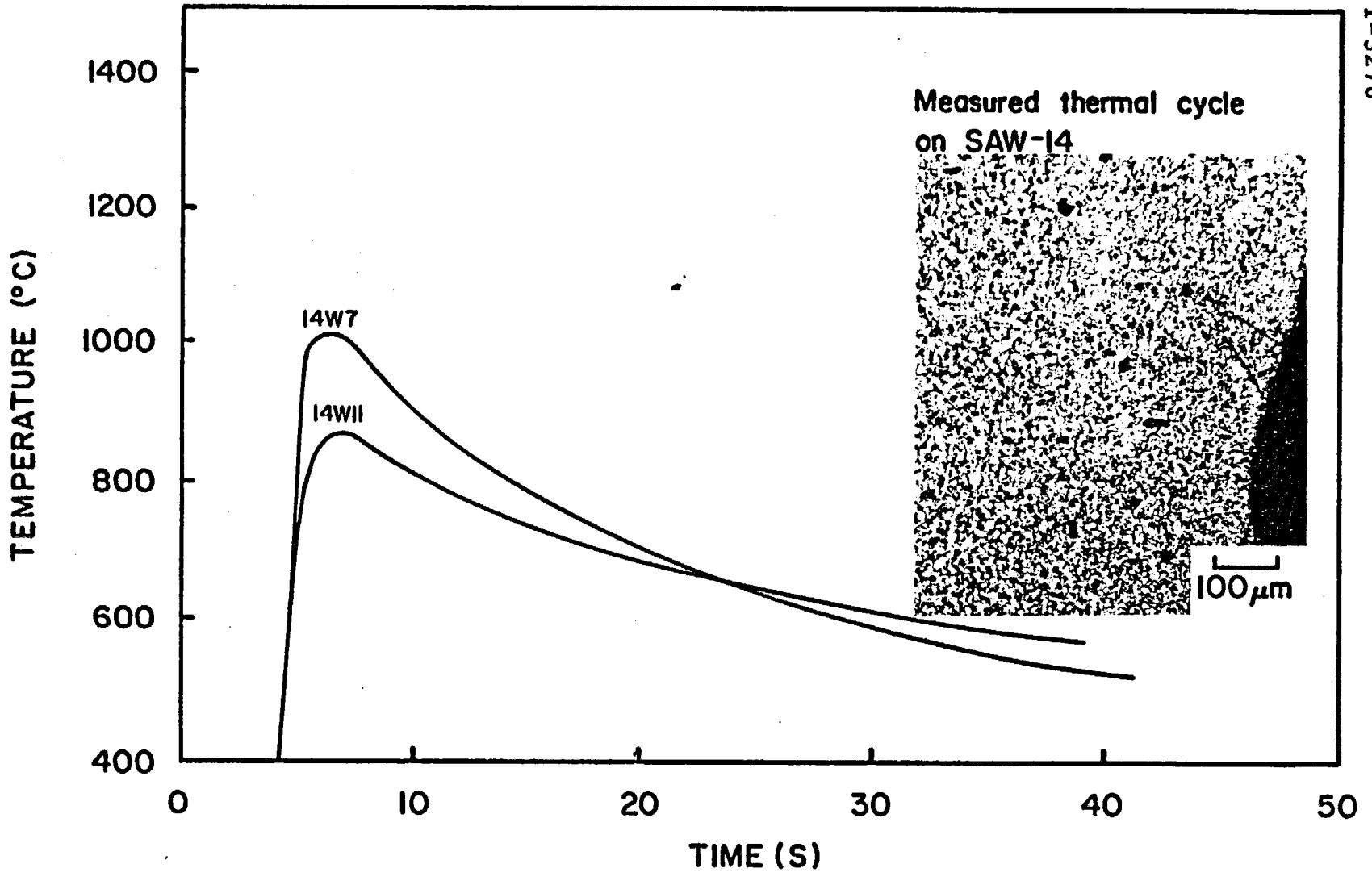

Figure 32. A measured set of thermal data taken from SAW-14 along with the associated microstructure. Refined equiaxed ferrite (white) and pearlite (black) are visible. 2% nital 100x.

Figure 33 shows a region monitored by a second thermocouple mounted in SAW-14. Curve SAW-14W10 has a peak temperature of 982°C and is in the lower grain refined region. Thermal profile SAW-14W14 has a peak temperature of 835°C which does not affect the already refined structure.

The thermal data was lost for the structures shown in Figure 34. However, from the appearance, the peak temperature was in the zone of spherioidized carbides between 700 and 750°C. This will be substantiated during Gleeble simulation.

Figure 35 depicts the microstructure of the region monitored by a thermocouple in SAW-12. SAW-12W10 has a peak temperature of 947°C which is between the grain refined zone and the partially transformed zone. SAW-12W14 has a peak temperature of 655°C and is outside the heat affected zone. The observed microstructure typifies a partially transformed region which, for this steel, indicates a sluggish ferrite to austenite transformation when compared to SAW-15. This anomaly will be addressed shortly.

Figure 36 shows the microstructure obtained from a second thermocouple hole in SAW-12. The thermal curve

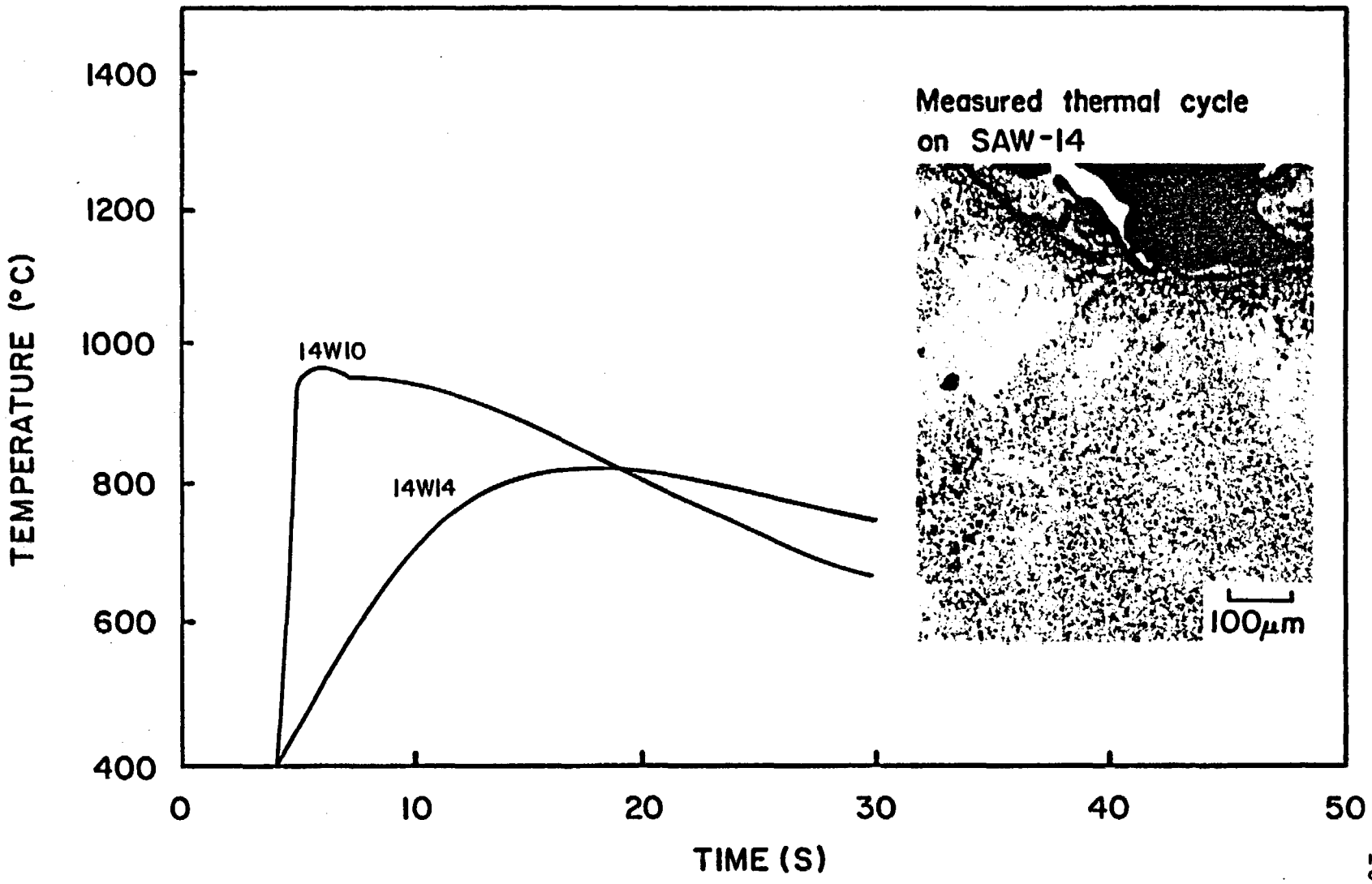

Figure 33. Thermal profiles measured from a second thermocouple in SAW-14 along with the associated microstructure, again showing refined ferrite (white) and pearlite (black). 2% nital 100x.

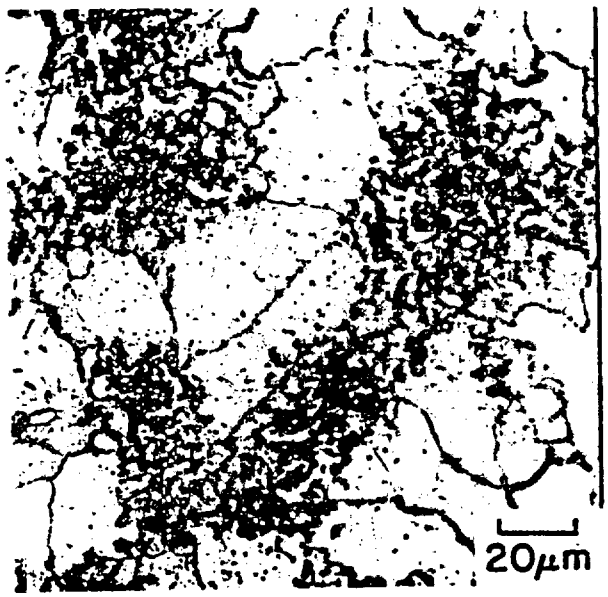

NRC-5

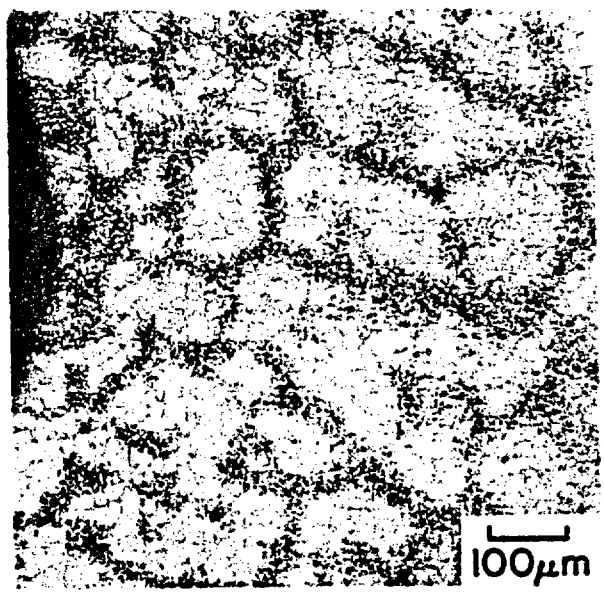

NRC-5

Figure 34. Photomicrographs taken below a thermocouple in SAW-5. The structure is partially transformed with broken pearlite (black) colonies and equiaxed ferrite (white).

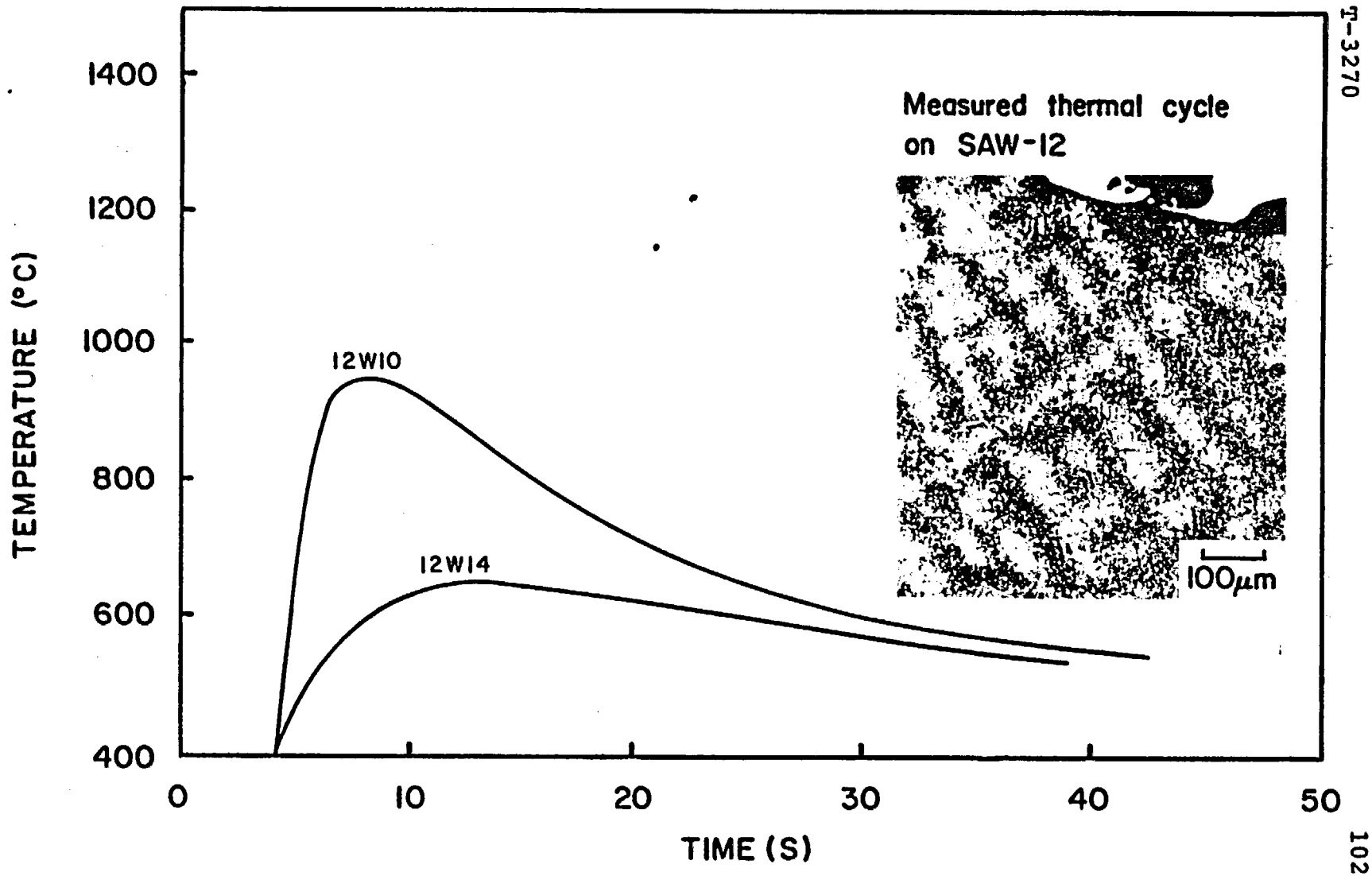

Figure 35. Thermal profiles measured from a second thermocouple mounted in SAW-12 along with the associated microstructure. The ferrite/pearlite morophology is partially transformed with broken pearlite (black) colonies. 2% nital 100x.

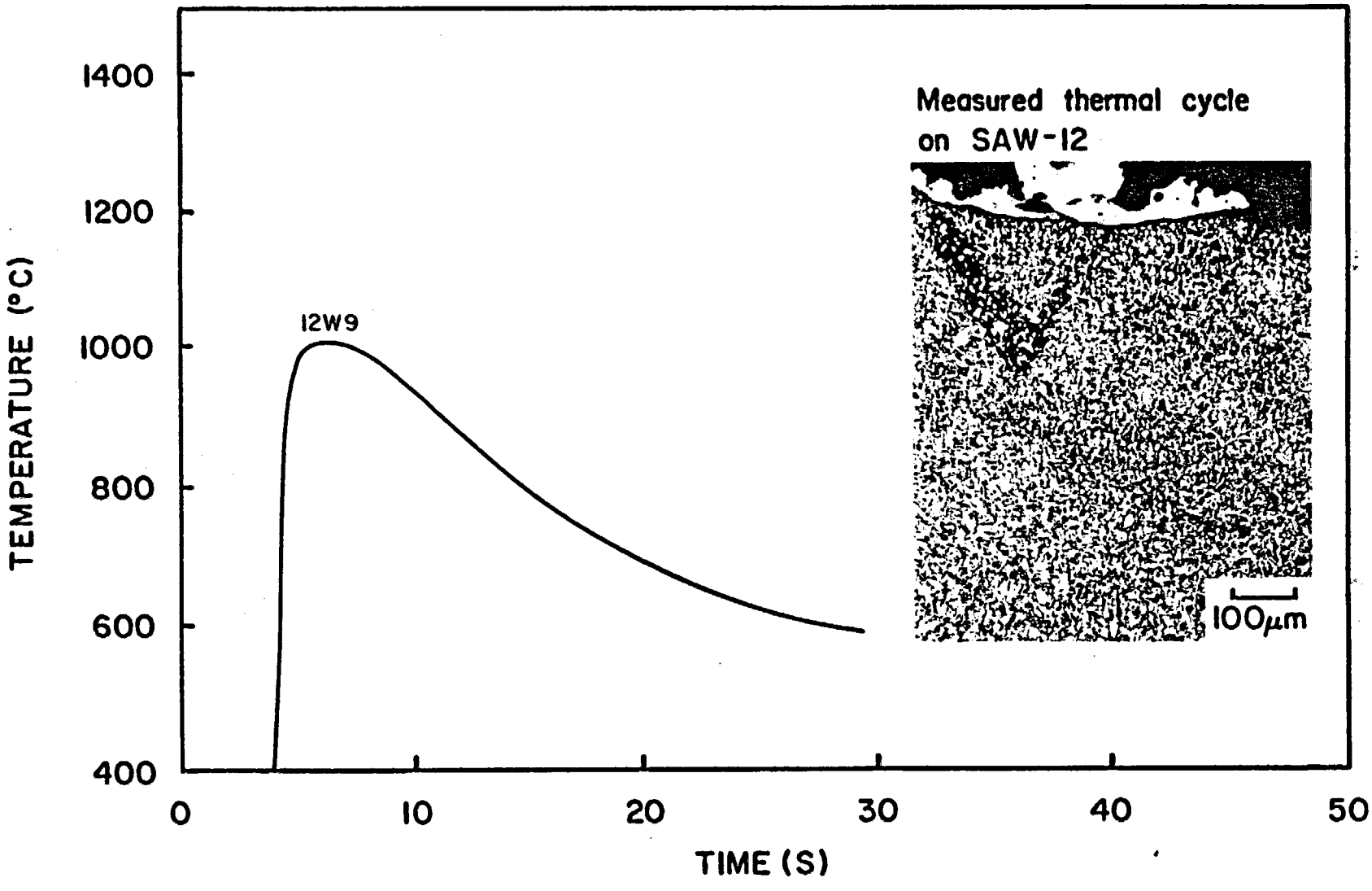

Figure 36. A thermal profile measured from a thermocouple mounted in SAW-12 along with the microstructure that was generated. It shows refined ferrite (white) and pearlite (dark). 2% nital 100x.

SAW-12W9 has a peak temperature of 1060°C which is in the grain refined region. As predicted , the microstructure is refined.

Figures 31 through 36 in conjunction with the diagram of Figure 27 prove that the experimental technique to measure the thermal experience of the heat affected zone was successful. Experimental constraints did not allow for the thermal experience to be measured closer than one millimeter from the fusion line. The weld joint design in combination with the multiple passes made thermocouple placement in this grain growth region prohibitive. The measured data, however, can be utilized to predict the thermal experience between 1100°C and the fusion line (1500°C) using appropriate heat transfer considerations. Before moving to that phase of the investigation further, microstructural examination of the affected zones of these welds was conducted.

Recalling that the basis behind this research was to investigate how casting and welding process variables affect the microstructure of steel overpack containers, and so far, for steels within the ASTM A-216 grade WCA specification, regardless of cleanliness or alloy content, no microstructural changes have been visible.

"Dirty" steel looks like "clean" steel, in the as-cast condition, and in the normalized condition. Now, in the weld heat affected zone where peak temperatures have not exceeded 1100°C, the structures also show very little sensitivity to the alloy and cleanliness modifications. However, when temperatures above 1100°C are reached, significant microstructural changes become apparent as shown in Figure 37a. These micrographs, with the fusion line at the top, show the region where peak temperatures range from 1520°C at the fusion line to approximately 1100°C at a distance of one millimeter away; precisely where thermocouple placement was prohibitive. Grain growth and particle dissolution significantly change the structure at these high peak temperatures and the affects of cleanliness and alloy content play a major role in the events that lead to the variance in microstructure depicted in Figure 37a and b.

Comparison of SAW-5 and SAW-12 shows that SAW-5 has more allotriomorphic ferrite, and Widmanstatten ferrite than does SAW-12. SAW-14 has a smaller prior austenite grain size than SAW-5, SAW-12 and SAW-15. The nature and mechanism for these microstructural changes will be discussed shortly. Suffice it to say that the observed

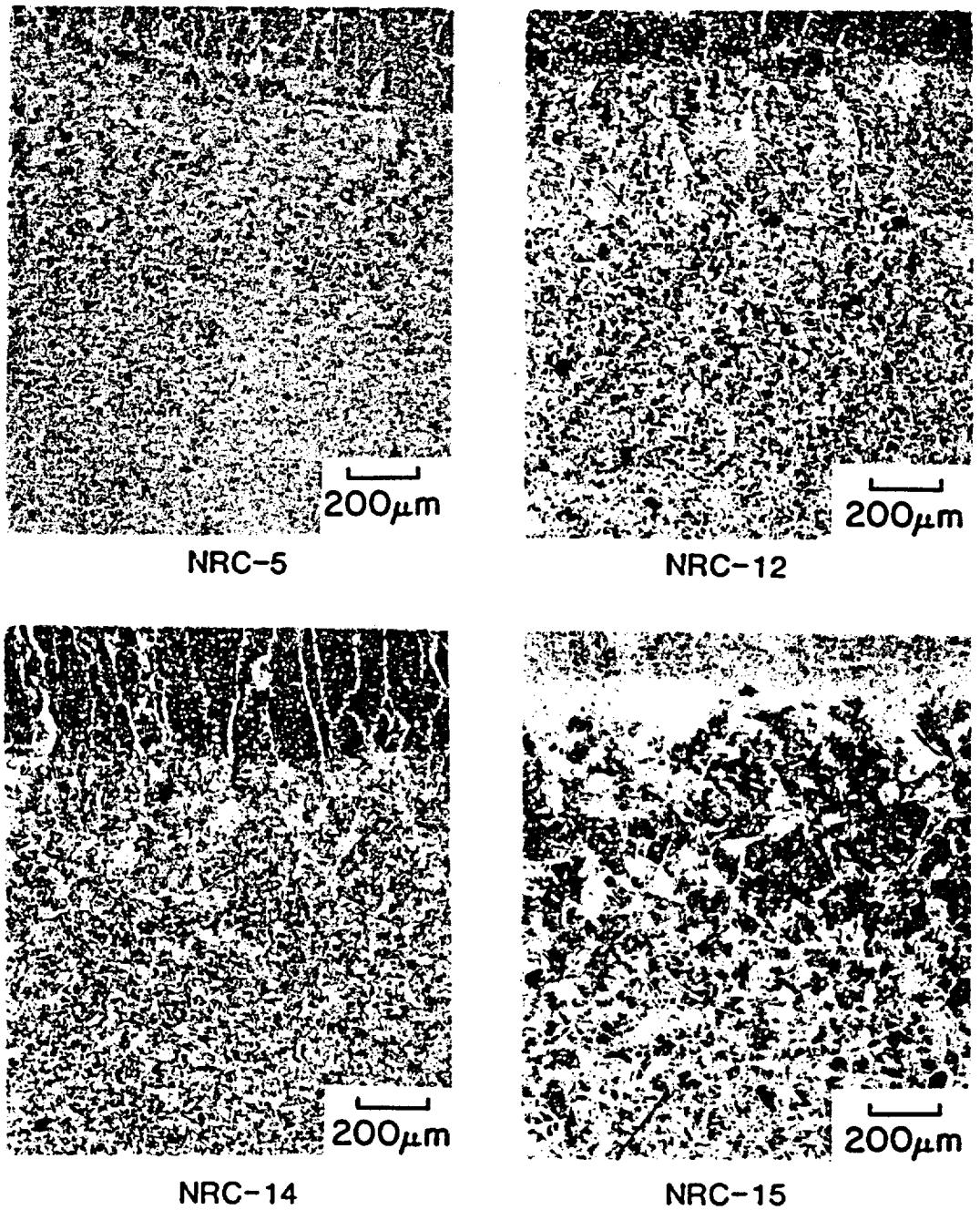

Figure 37a. The fusion zone (top) and grain growth region of the four welds studied, showing the microstructural differences directly next to the fusion line. Yorgasons etch, 50x.

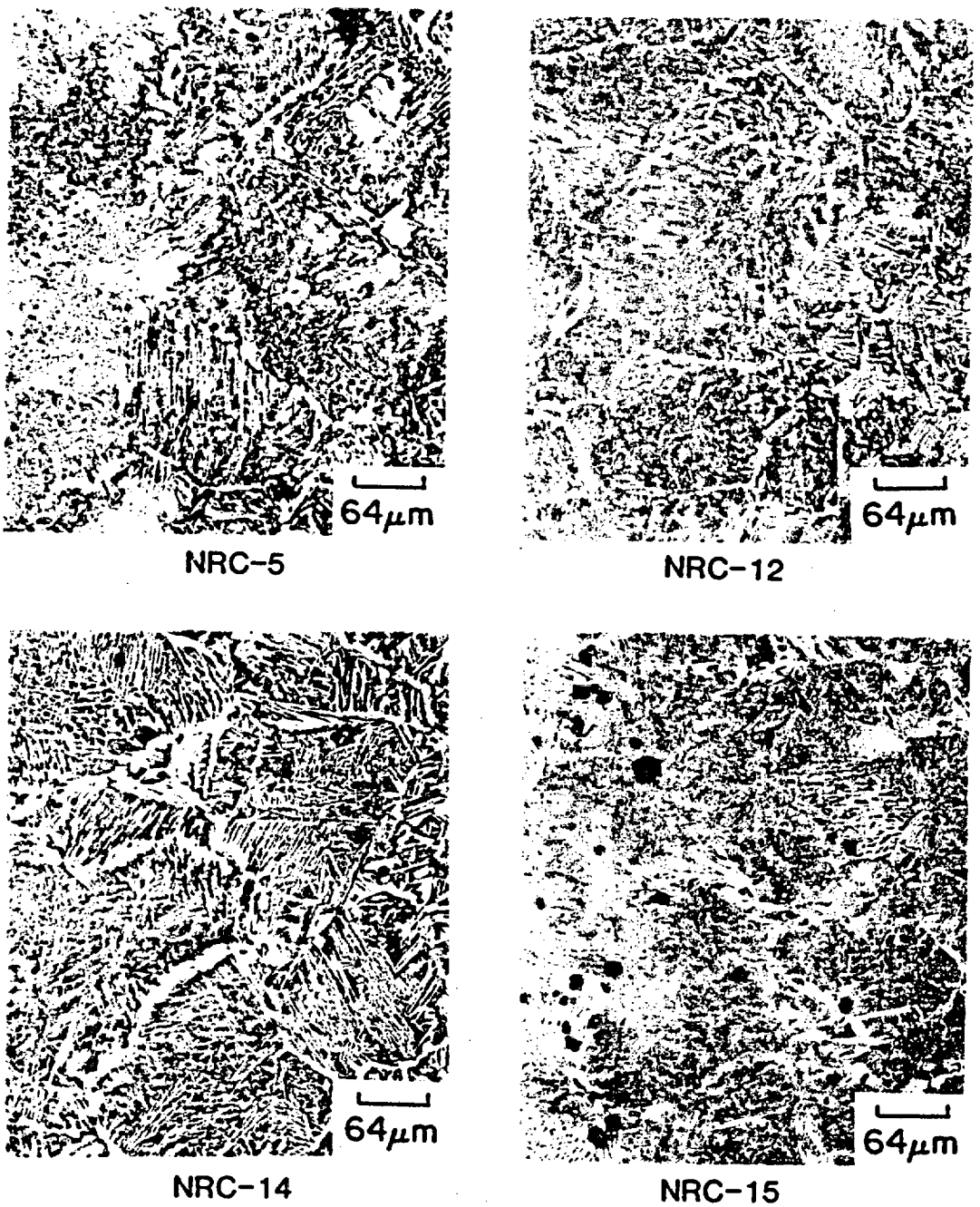

Figure 37b. The grain growth region of each of the four steels showing microstructural differences related to cleanliness and alloy content. Yorgasons etch, 156x.

differences can be directly related to alloy content and cleanliness.

3.4 HEAT AFFECTED ZONE MODELLING

Rosenthal's three dimensional heat transport equation (14) was used to predict the thermal experience of the one millimeter wide region adjacent to the fusion line. The analytical curves, MR11092, MR111, and MR1111 are shown in Figure 22 along with selected curves from the measured thermal cycles of this study.

The region significantly affected by the alterations in chemical composition was shown to be the one millimeter wide region next to the fusion line in which the peak temperature exceeds 1100°C. This grain growth region has the most susceptible microstructure to degradation by corrosion and loss of mechanical properties. Since mechanical or corrosion test specimens cannot be machined economically from a one millimeter wide region, a Gleeble 1500 weld simulator was evaluated as a tool to duplicate specific regions of the heat affected zone in a 0.250 inch (6.35 mm) diameter test specimen. First, the measured curves shown in Figures 31

through 36 were programmed into the Gleeble 1500. These thermal profiles were run on machined samples from the corresponding heats. For example, the curves shown in Figure 31 were measured on SAW-15 (Submerged Arc Weld on plate from heat NRC-15). Hence, Gleeble specimens were machined from heat NRC-15 plate, and the programmed thermal profiles were run on these specimens. A microstructural comparison between the actual weld and the Gleeble simulated microstructure was completed to evaluate the effectiveness of the Gleeble 1500 as a tool to duplicate heat affected zone microstructure in cast and normalized, welded steel. Secondly, a microstructural map of the heat affected zone at approximately 100°C peak temperature intervals between 690°C and 1450°C was generated on the four steels using the program curves shown in Figure 22. This map was used to evaluate the effects of alloy content and cleanliness on heat affected zone microstructure. The results of the microstructural duplication experiments using the Gleeble 1500 weld simulator are discussed below.

The thermal profiles SAW-15W7, SAW-15W11 and SAW-15W15 shown in Figure 31 were run on a Gleeble sample from cast and normalized NRC-15 plate. Figure 38a shows

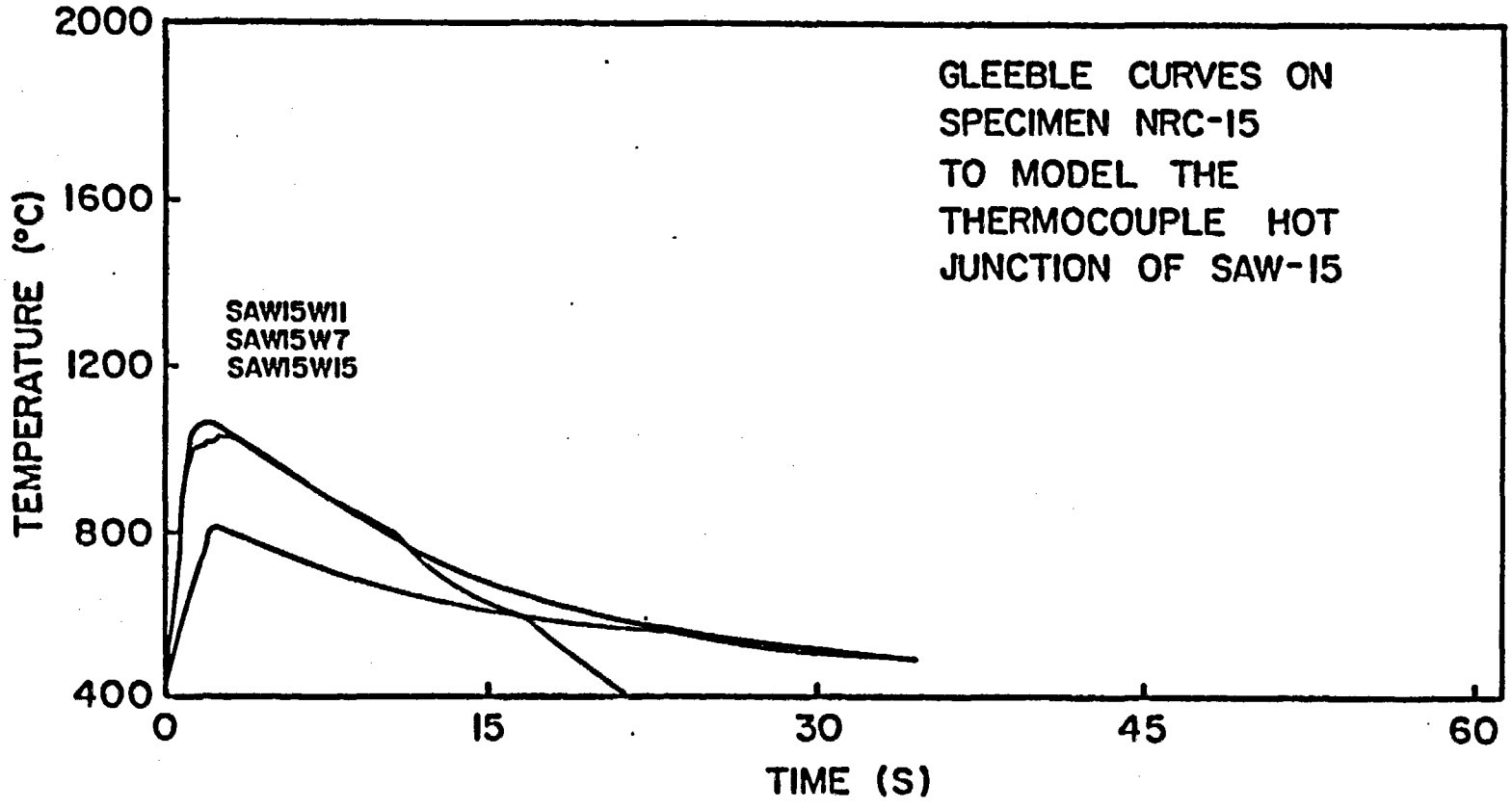

Figure 38a. The measured Gleeble curves which generated the microstructure of Figure 38b.

the thermal curves measured from the Gleeble 1500 and Figure 38b compares the simulated microstructure with the actual. As seen, the microstructural duplication is excellent, showing a refined grain size, and equiaxed ferrite/pearlite.

Thermal profiles SAW-12W10 and SAW-12W14 from Figure 35 were run on a Gleeble sample from heat NRC-12. The simulated thermal experience is plotted in Figure 39a and the simulated and actual microstructures are compared in Figure 39b. Again, the structures match very well. With a peak temperature from SAW-12W10 of 941°C, the structure is partially transformed with the pearlite being broken and fine.

Thermal profiles SAW-14W7 and SAW-14W11 from Figure 32 were run on a Gleeble specimen from heat NRC-14, and are shown in Figure 40a. The comparison in Figure 40b shows excellent agreement. The microstructure obtained is refined ferrite/pearlite typical of peak temperatures between 900°C and 1100°C as depicted by Figure 26.

Measured curves SAW-14W10 and SAW-14W11 were run on another Gleeble specimen from heat NRC-14 (Figure 41a). the comparison, shown in Figure 41b is again excellent. The microstructure is refined ferrite/pearlite.

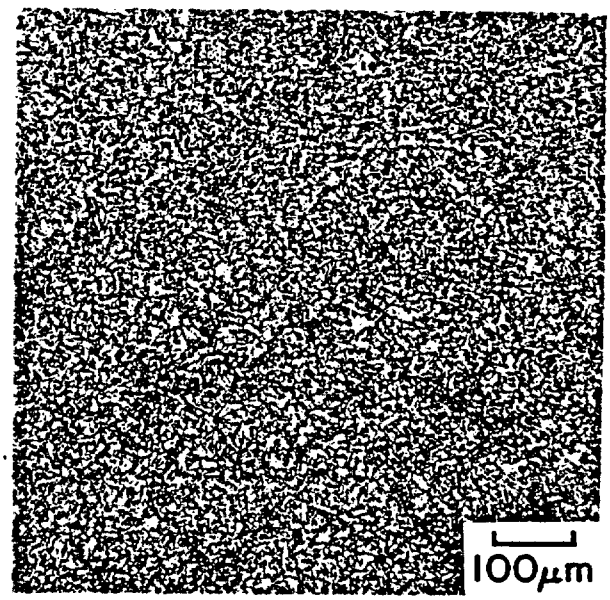

NRC-15

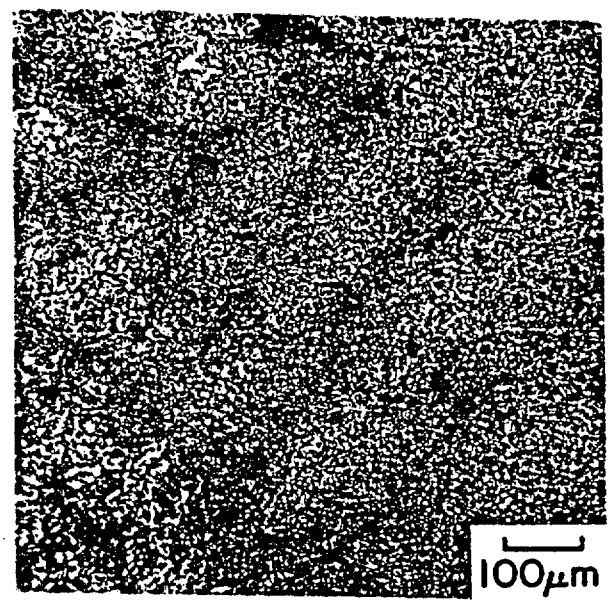

SAW-15

Figure 38b. A comparison between the Gleeble generated microstructure and the actual heat affected zone microstructure of plate from heat NRC-15. 2% nital 100x.

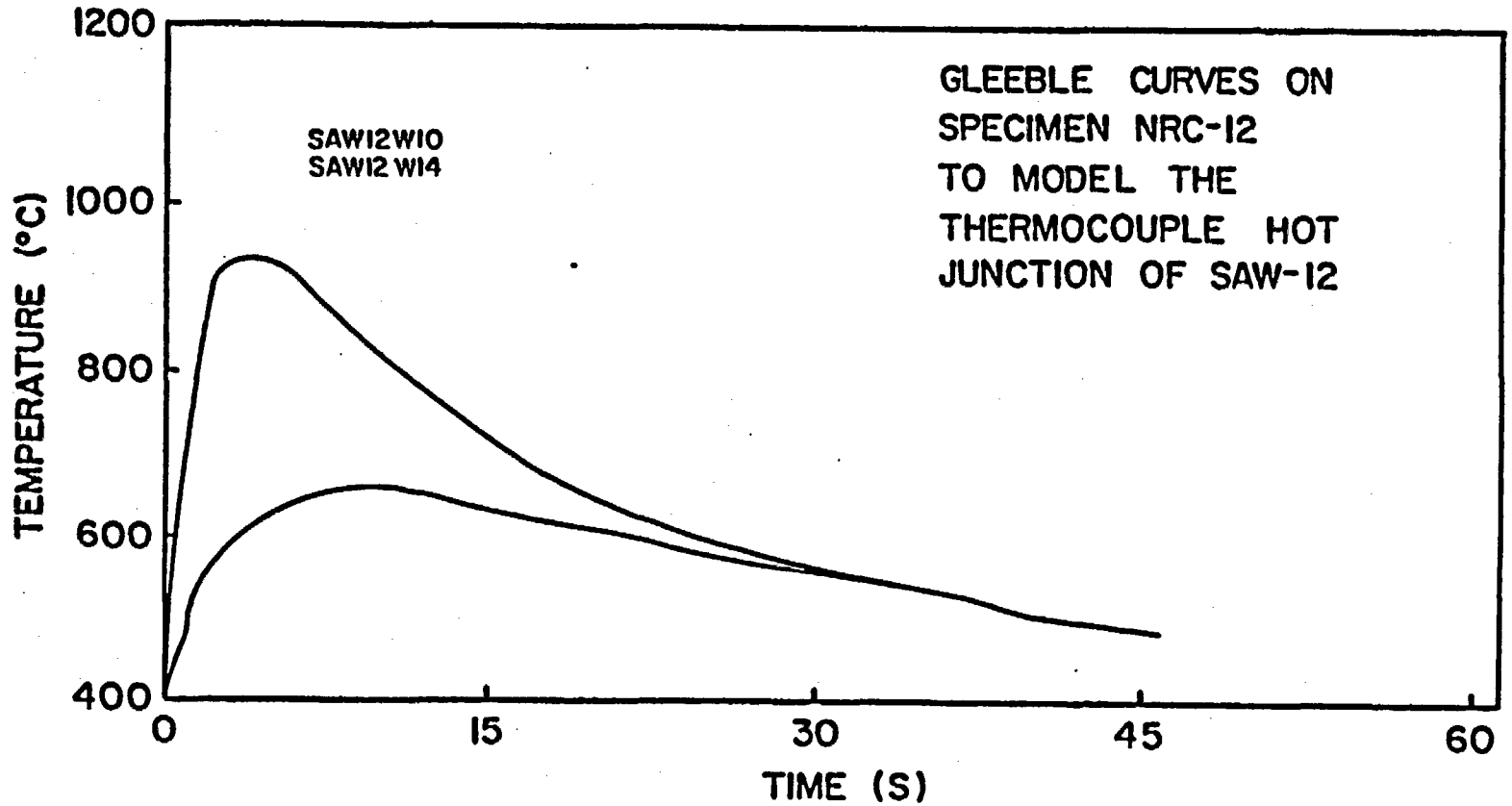

Figure 39a. The measured Gleeble curves which generated the microstructure of Figure 39b.

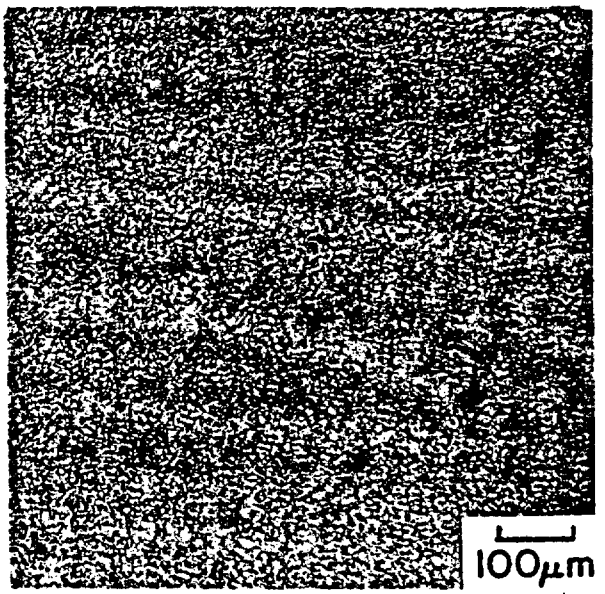

NRC-12

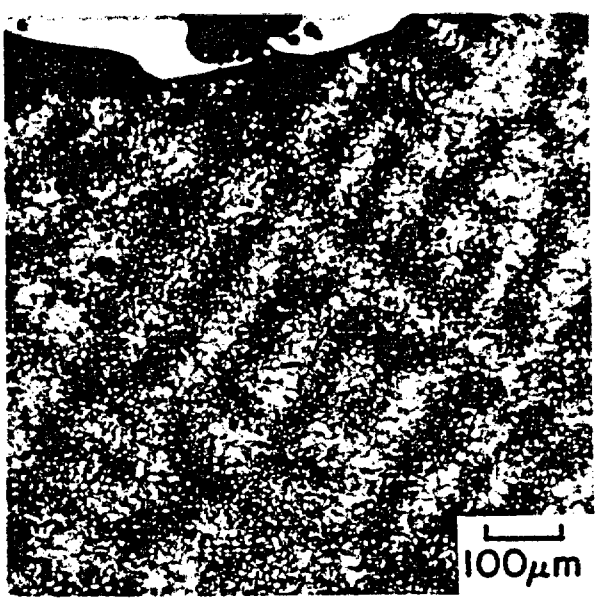

SAW-12

Figure 39b. A comparison between the Gleeble generated microstructure and the actual heat affected zone microstructure on plate from heat NRC-12.

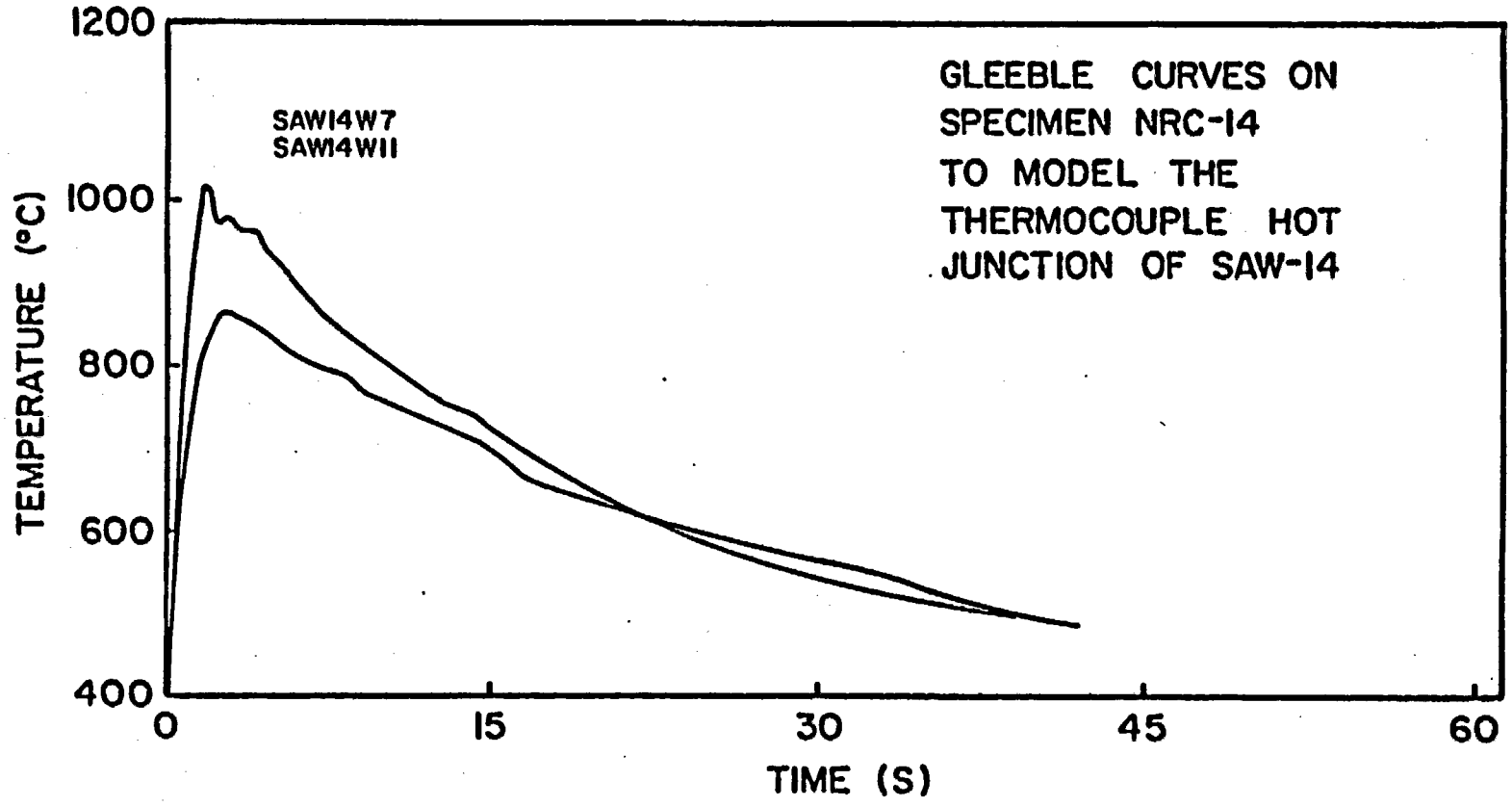

Figure 40a. The Gleeble curves which generated the microstructure of Figure 40b.

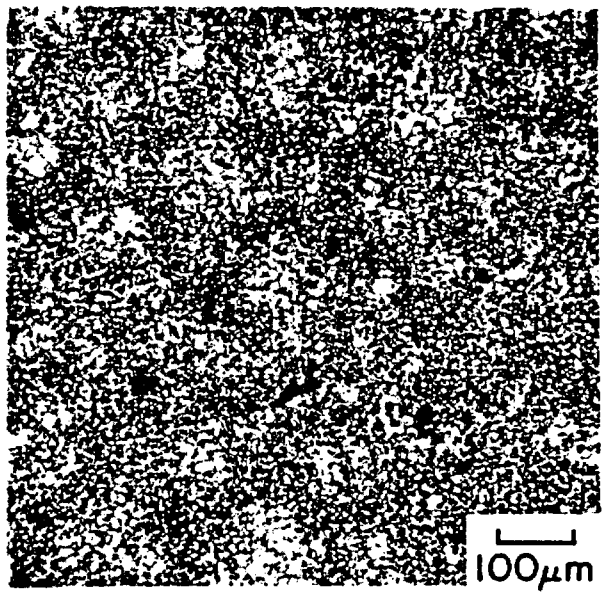

NRC-14

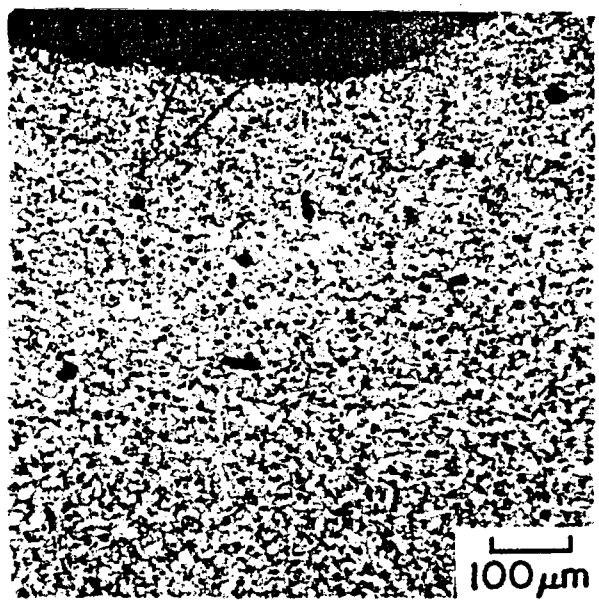

SAW-14

Figure 40b. A comparison between the Gleeble modelled and actual heat affected zone microstructure on plate from heat NRC-14. 2% nital, 100x.

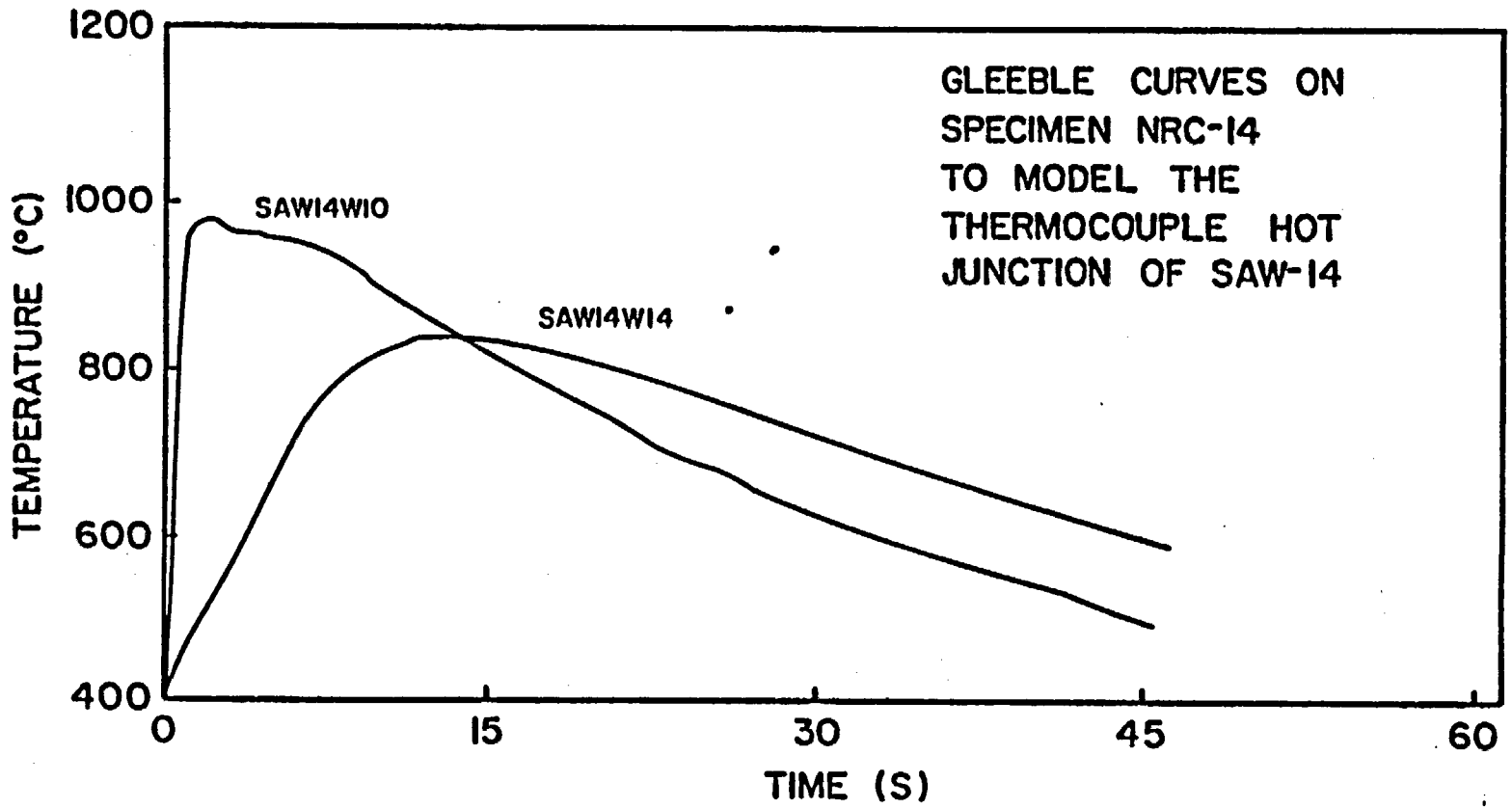

Figure 41a. The Gleeble curves which generated the microstructure of Figure 41b.

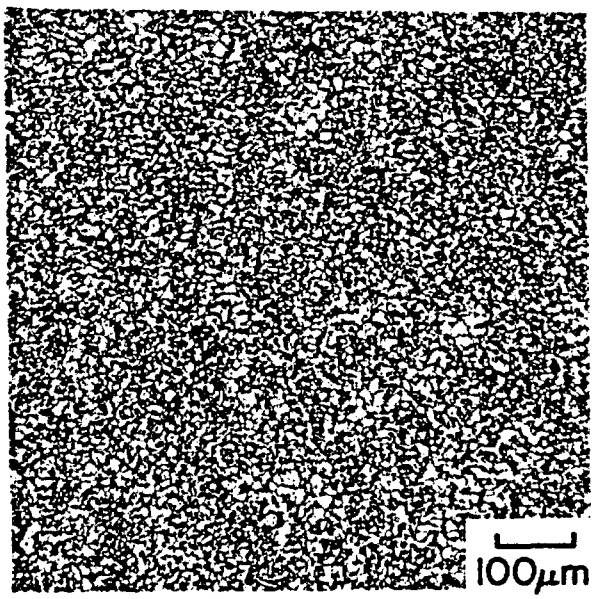

NRC-14

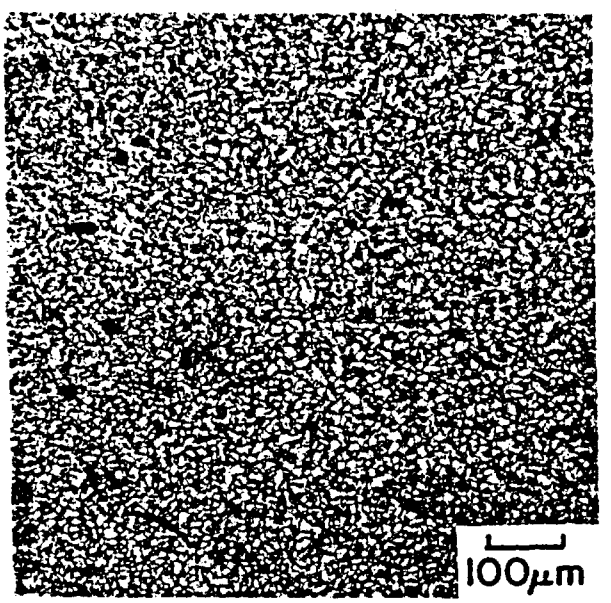

SAW-14

Figure 41b. A comparison between the Gleeble modelled and actual heat affected zone microstructure on a second sample from heat NRC-14. 2% nital, 100x.

Figure 42a shows curve SAW-12W9 which wwas run on a Gleeble specimen from heat NRC-12. Figure 42b shows the comparison between the actual microstructure obtained from thermal curve SAW-12W9 of Figure 37 and the Gleeble modelled structure. The structures are refined ferrite/pearlite.

These comparisons show that the Gleeble 1500 weld simulator can indeed duplicate the heat affected zone microstructure from measured time-temperature curves on cast and normalized weld plate.

The curves shown in Figure 22 were run on Gleeble samples from each of the heats of steel, NRC-5, NRC-12, NRC-14, and NRC-15. Each curve has a peak temperature approximately 100°C above the previous, so that the microstructures obtained represented a map of the heat affected zone at 100°C peak temperature intervals from 690°C to 1450°C. These chosen curves yielded specimens that show the microstructual changes brought about by the chemical variations and cleanliness of each steel.

The micrographs taken from the Gleeble specimens are shown along with the programmed curves that generated them. Figure 43a shows the thermal profile SAW-15W12

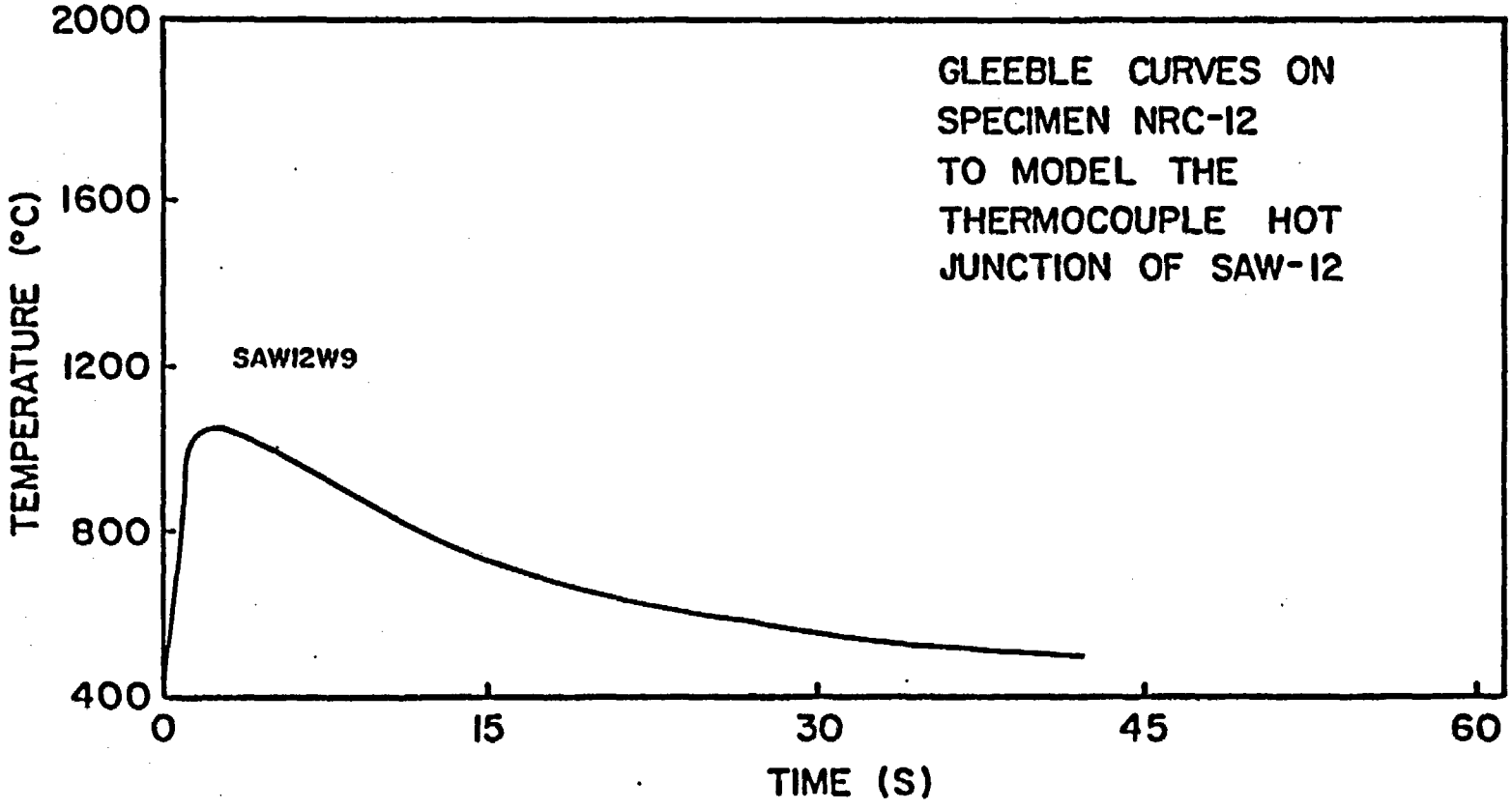

Figure 42a. The Gleeble curves that generated the microstructure of Figure 42b.

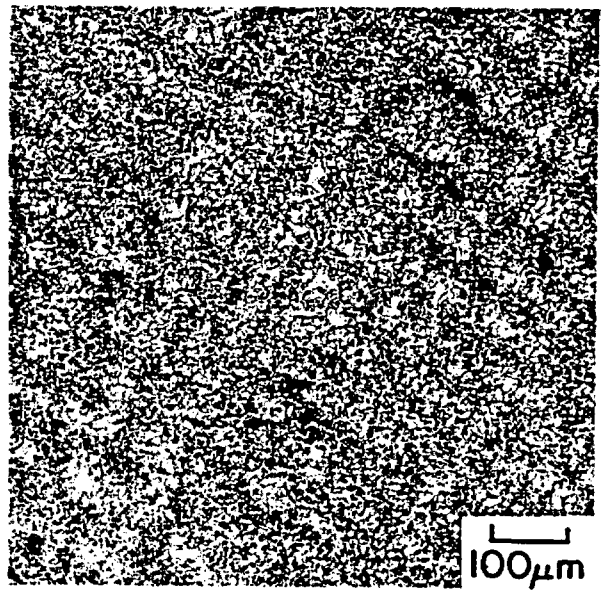

NRC-12

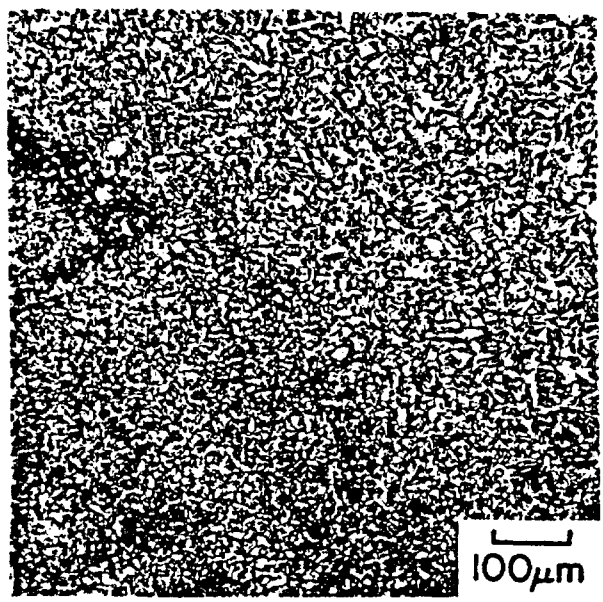

SAW-12

Figure 42b. A comparison between the Gleeble modelled and actual heat affected zone microstructure on a second sample from heat NRC-12. The curves that generated the structure are shown in Figure 42a.

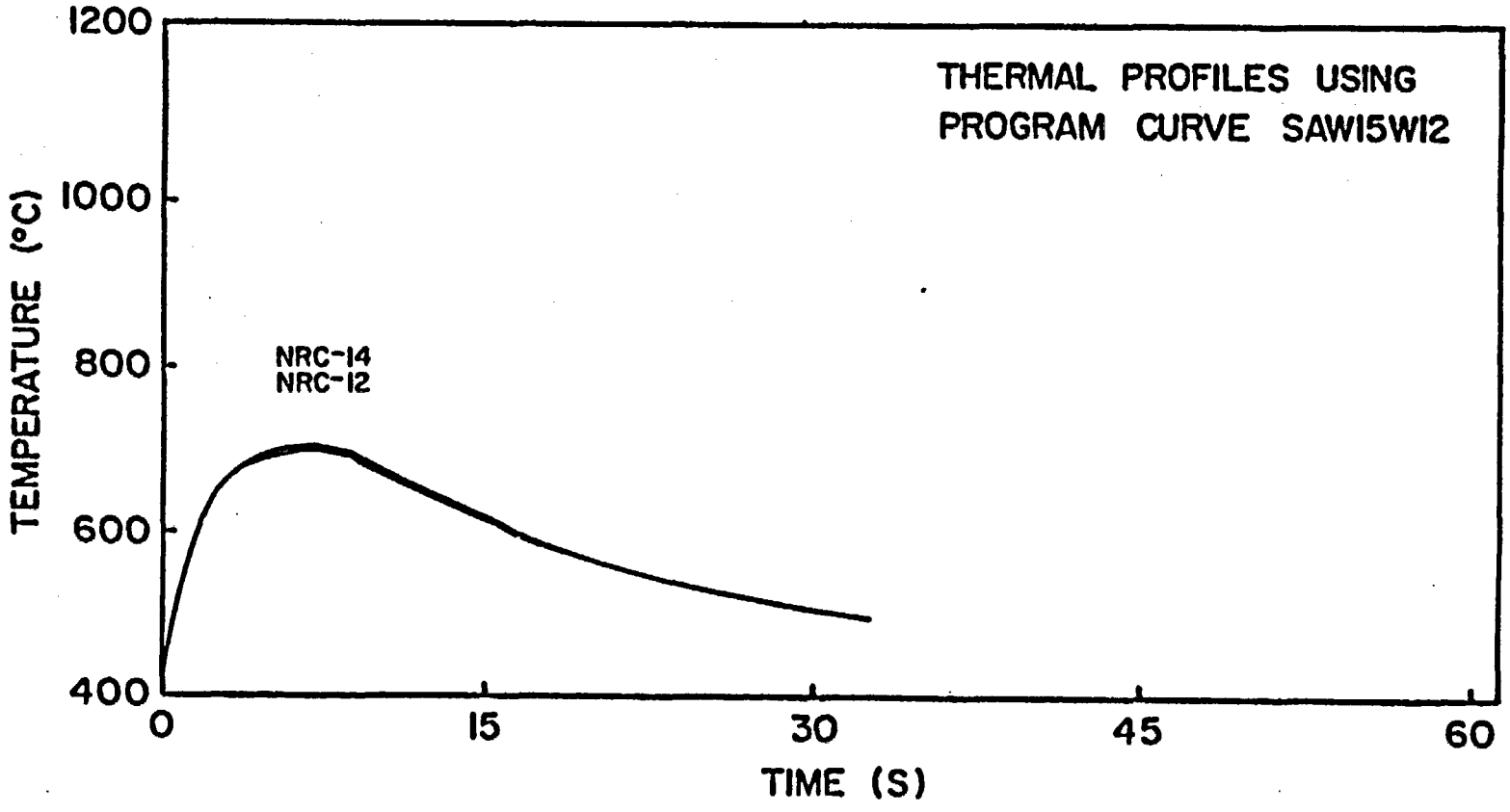

Figure 43a. The resultant thermal profiles on specimens NRC-12 and NRC-14 obtained using SAW-15W12 as a program curve.

that was run on heats NRC-12 and NRC-14. For NRC-14, the peak temperature was 705°C and for NRC-12 it was 697°C. Figure 43b shows the microstructure of both. No change over the starting microstructure of Figure 26 is observed.

Figure 44a shows the thermal profiles obtained using SAW-14W11 as a program curve. For NRC-5 the peak temperature was 860°C; for NRC-12, 865°C; for NRC-14, 870°C; and for NRC-15, 880°C. The resulting microstructures shown in Figure 44b reveal lamellar pearlite with some grain refinement.

Figure 45a shows the measured thermal profiles using SAW-12W10 as a program curve. The peak temperatures obtained were: NRC-5, 938°C; NRC-12, 931°C; NRC-14, 930°C; and NRC-15, 940°C. The microstructures (Figure 45b) show some refinement and breaking apart of the pearlite colonies. The structure seen on NRC-12 indicates that the transformations on heating and cooling are slower than the others. This sluggish transformation was noted earlier in the actual measured microstructure shown in Figure 35, but as yet no explanation has been determined.

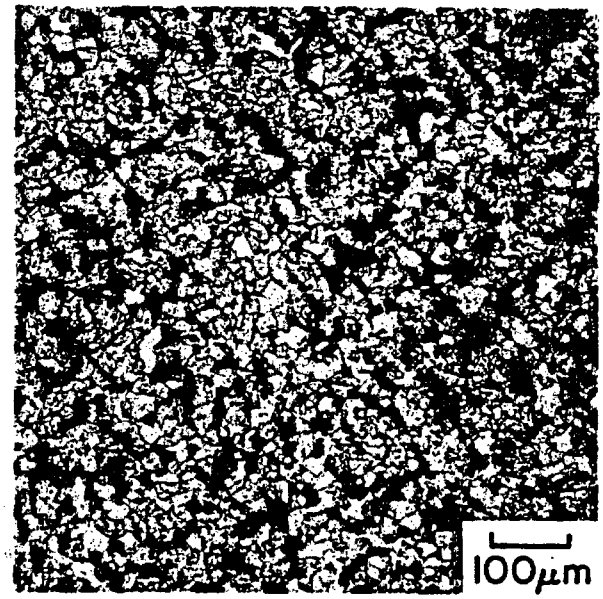

NRC-12

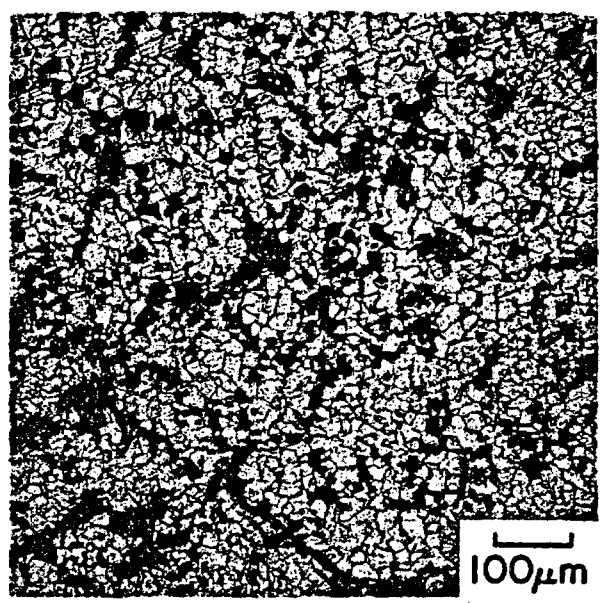

NRC-14

Figure 43b. The resultant microstructures generated from the curves of Figure 43a. 2% nital, 100x.

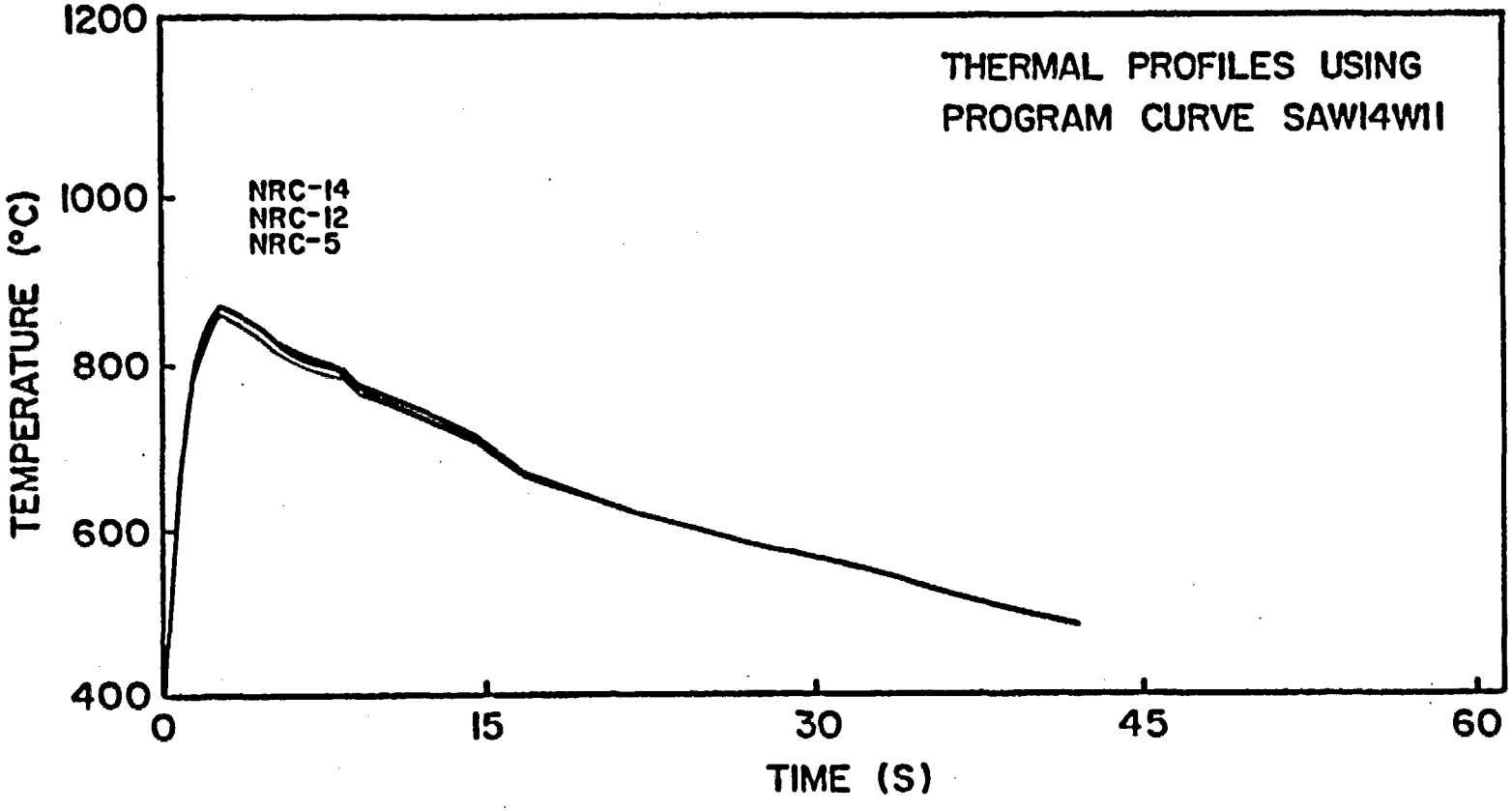

Figure 44a. The resultant thermal profiles on specimens NRC-5, NRC-12, NRC-14, and NRC-15 obtained using SAW-14W11 as a program curve.

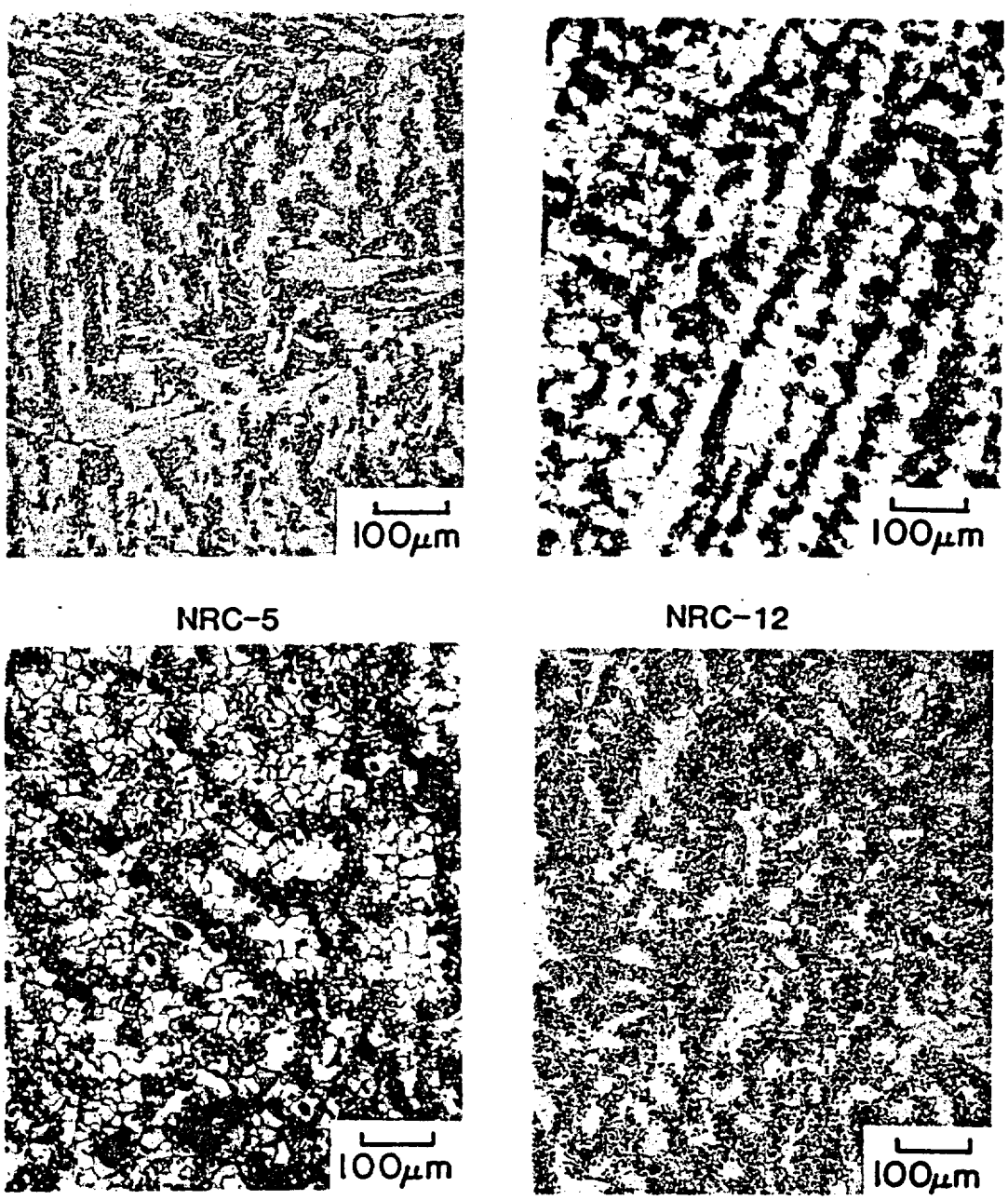

Figure 44b. The resultant microstructures generated from the curves of Figure 44a. There are slight microstructural variations but nothing significant. 2% nital, 100x.

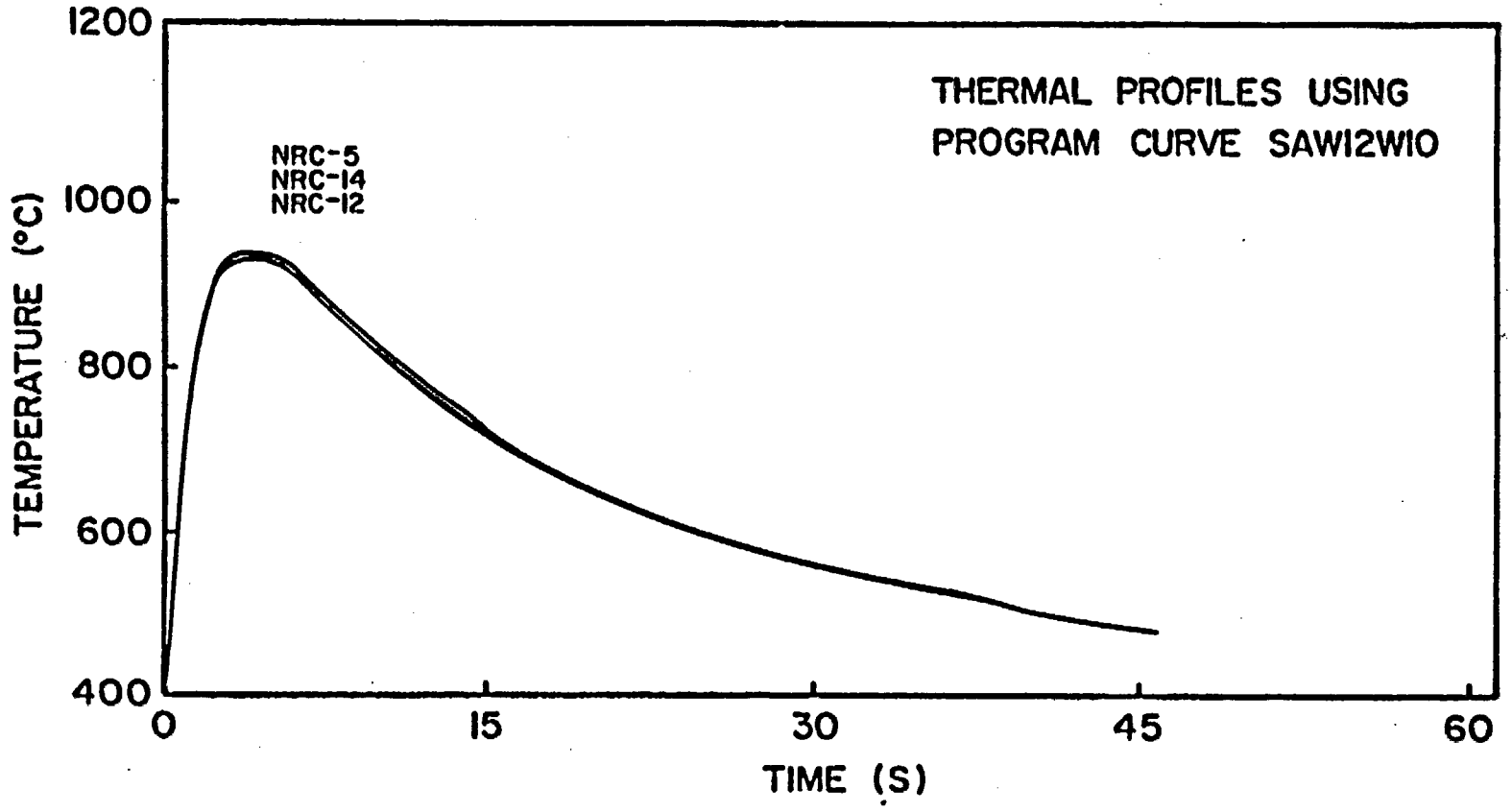

Figure 45a. The resultant thermal profiles on specimens NRC-5, NRC-12, NRC-14, and NRC-15 obtained using SAW-12W10 as a program curve.

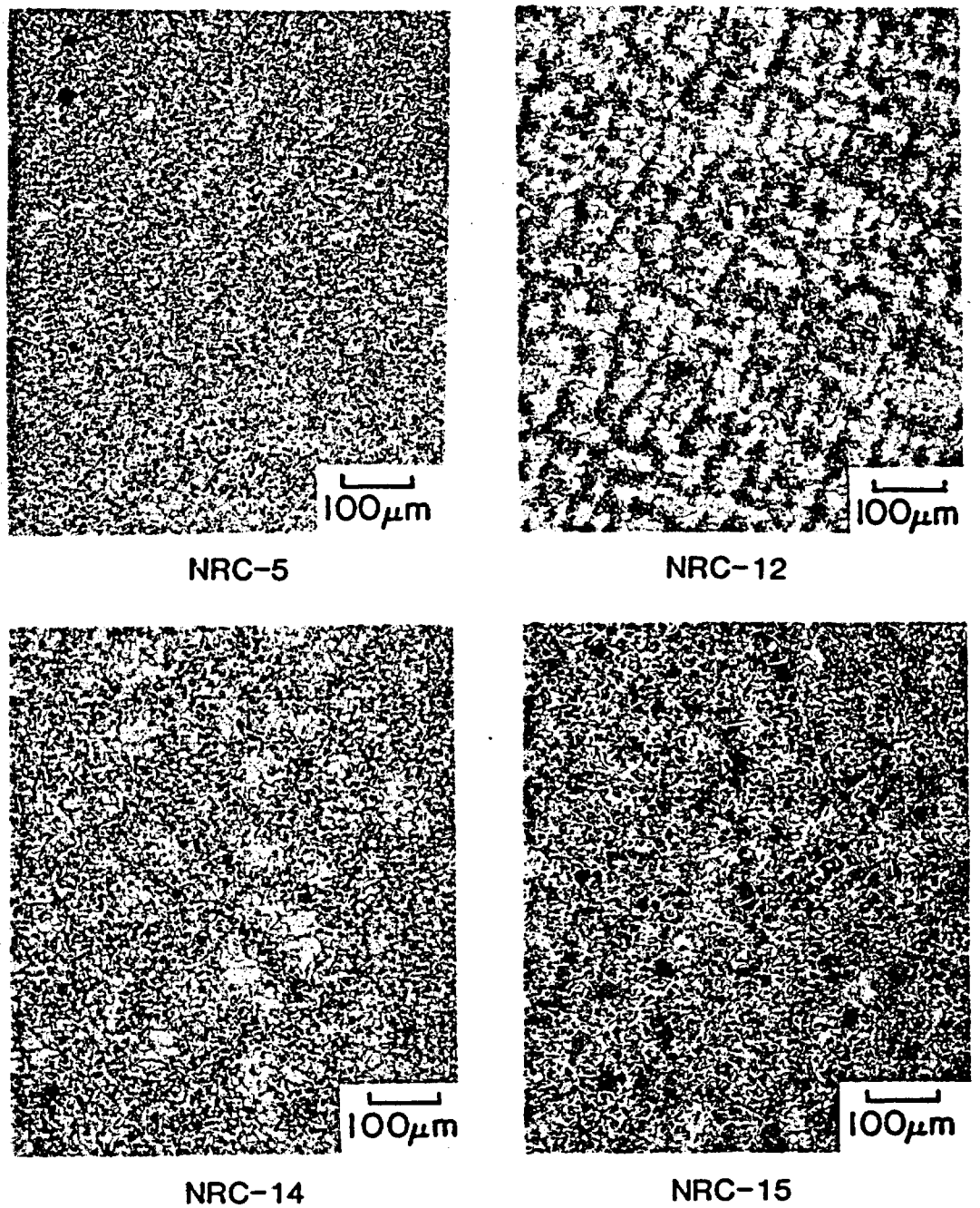

Figure 45b. The resultant microstructures generated from the curves of Figure 45a. 2% nital, 100x.

Figure 46a shows the thermal profiles obtained using SAW-12W9 as a program curve. The peak temperatures were: NRC-5, 1010°C; NRC-12, 1040°C; NRC-14, 1010°C; and NRC-15, 1040°C. The microstructures (Figure 46b) show a highly refined ferrite/pearlite structure, which has lost the signs of the dendritic structure, excepting NRC-12 which still shows sluggish transformations.

Figure 47a shows the measured thermal profiles using WI-1 as a program curve. The peak temperatures obtained were: NRC-5, 1170°C; NRC-12, 1135°C; NRC-14, 1160°C; and NRC-15, 1175°C. The obtained microstructures (Figure 47b) show a refined structure of equiaxed ferrite/pearlite. NRC-12 no longer has the sluggish transformations.

Figure 48a shows the thermal profiles obtained by using the empirically derived MR1111 program curve. The peak temperatures obtained were: NRC-5, 1228°C; NRC-12, 1250°C, NRC-14, 1275°C; and NRC-15, 1240°C. The obtained microstructures (Figure 48b) show the beginning of grain growth. There is an affect of cleanliness and chemical variations on the microstructures at these peak temperatures; the prior austenite grain sizes of NRC-12 and NRC-14 are larger than NRC-5 or NRC-15. (The prior

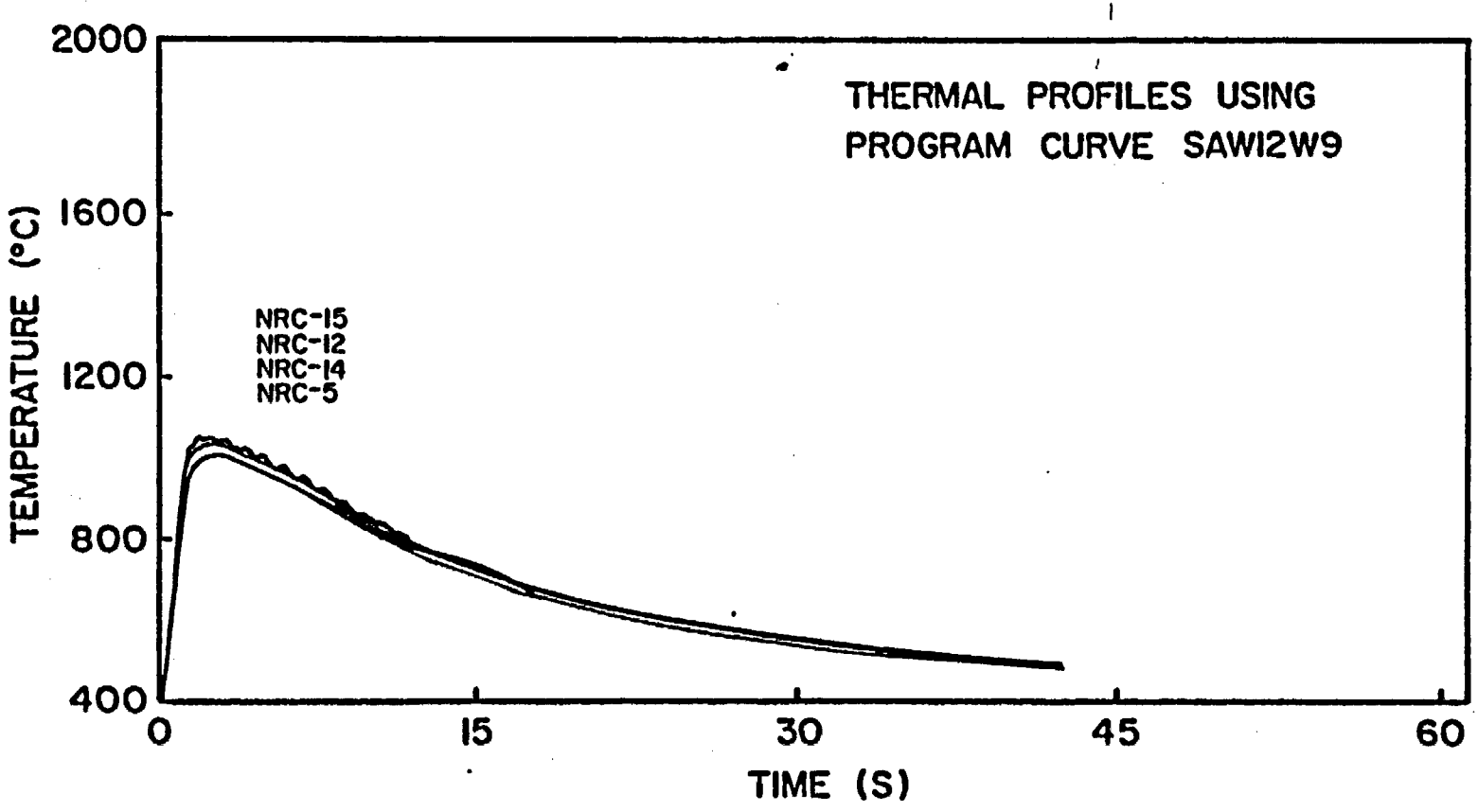

Figure 46a. The resultant thermal profiles on specimens NRC-5, NRC-12, NRC-14, and NRC-15 obtained using SAW-12W9 as a program curve.

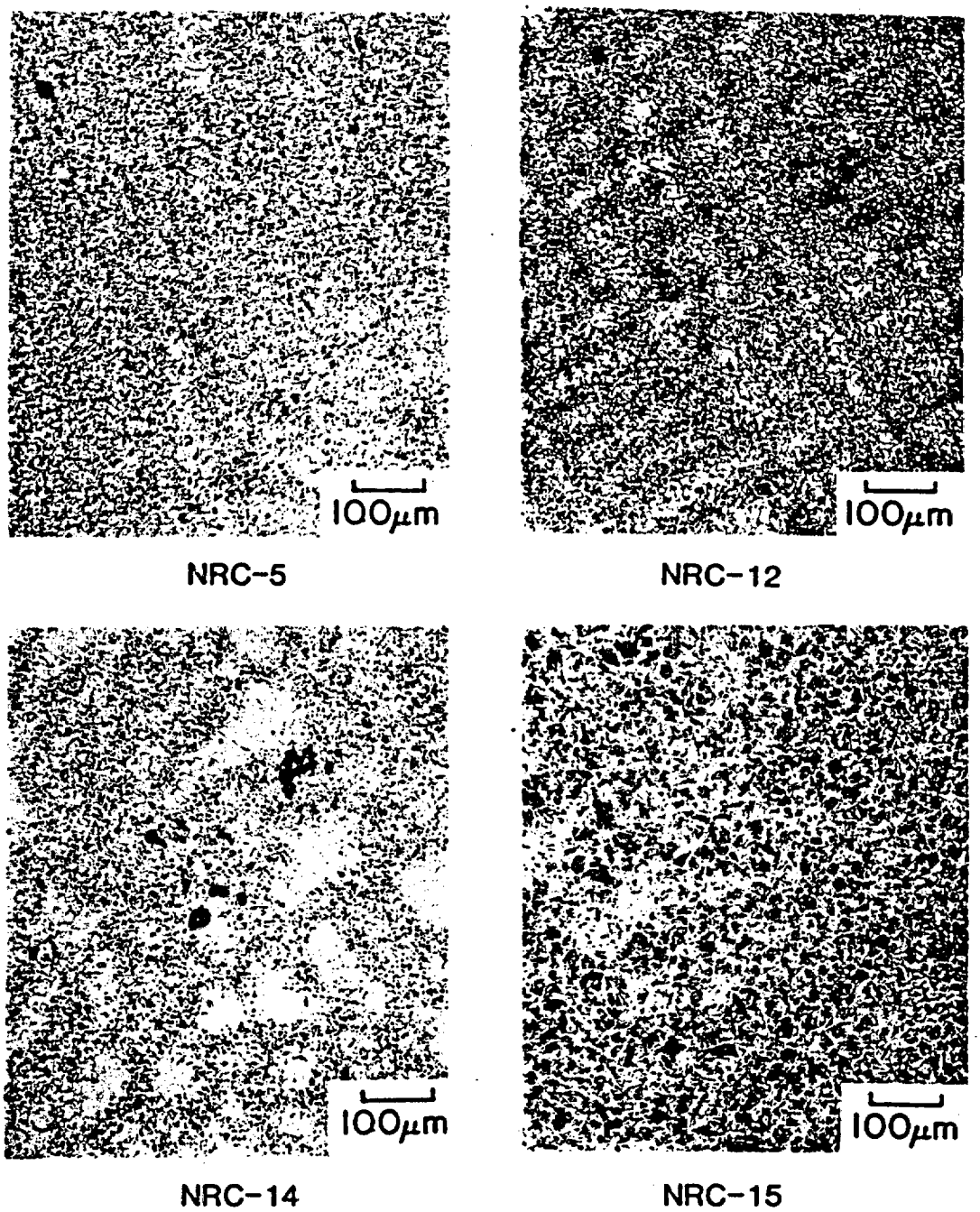

Figure 46b. The resultant microstructures generated from the curves of Figure 46a. NRC-15 has bainite grain centers decorated by allotriomorphic ferrite. The others show equiaxed ferrite/pearlite. 2% nital, 100x.

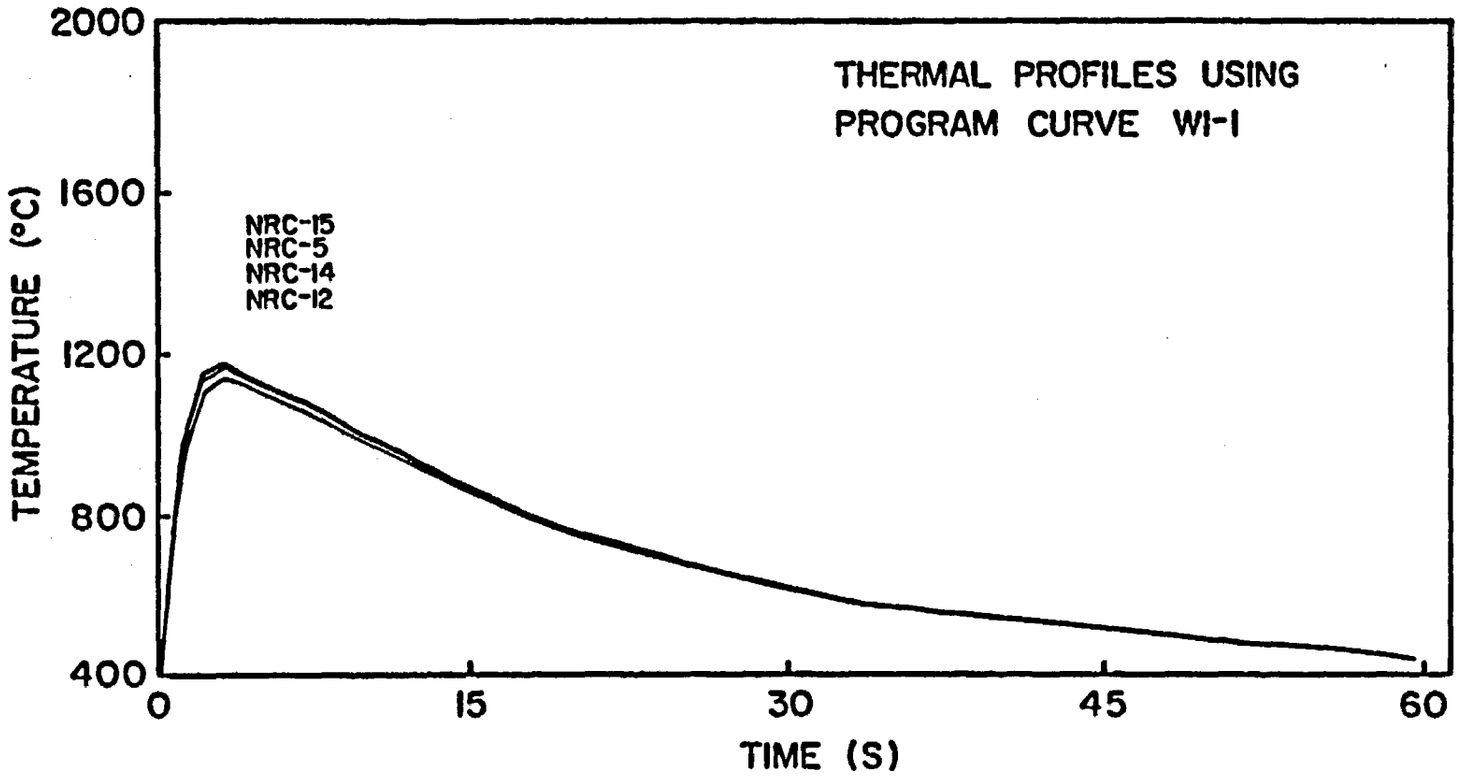

Figure 47a. The resultant thermal profiles on specimens NRC-5, NRC-12, NRC-14, and NRC-15 obtained using WI-1 as a program curve.

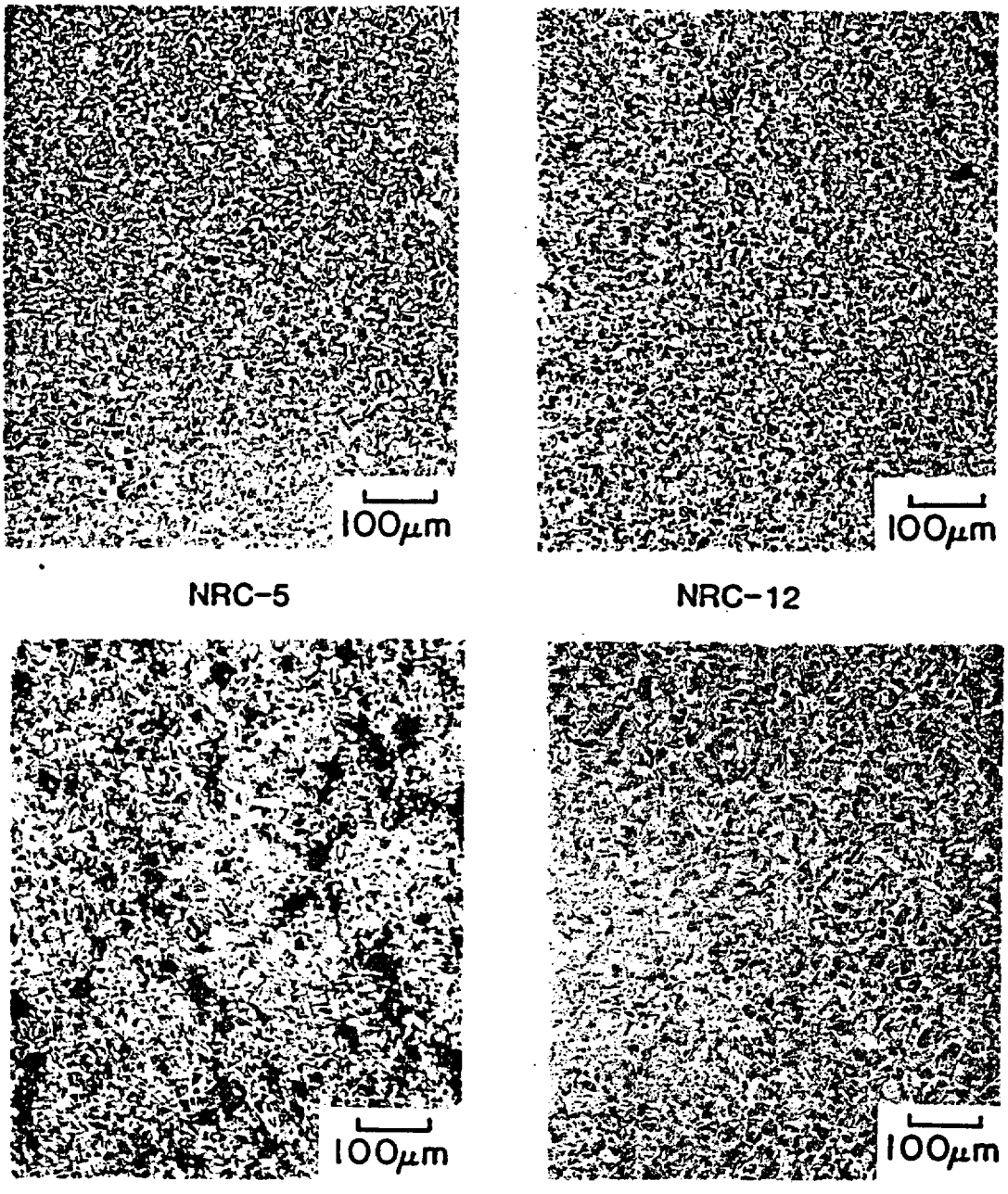

Figure 47b. A microstructural comparison between the experimental steels obtained from the curves of Figure 47a. NRC-15 shows upper bainite (gray) decorated by allotriomorphic ferrite (white) with evidence of austenite grain growth. The others show equiaxed ferrite/pearlite. 2% nital, 100x.

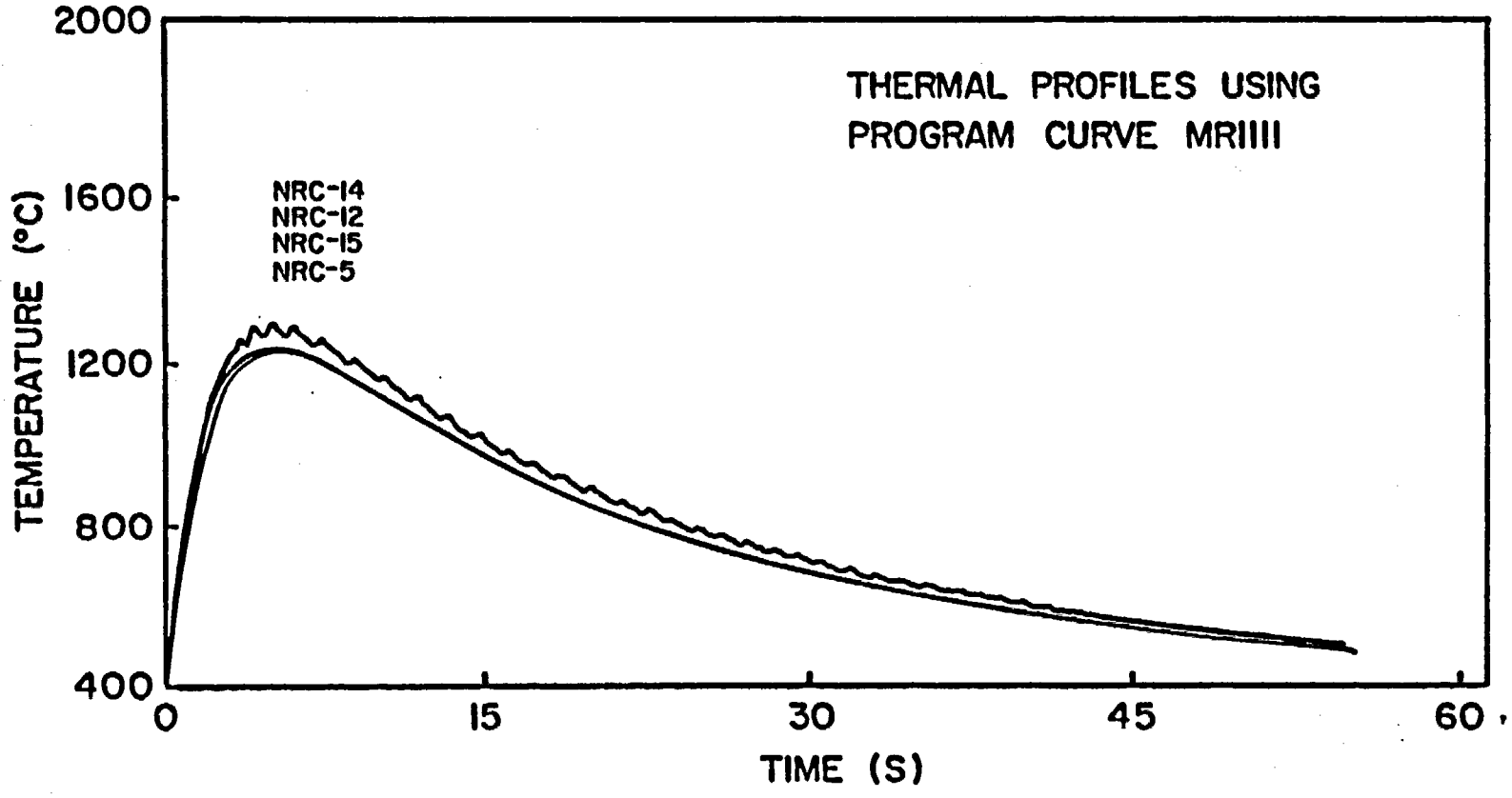

Figure 48a. The resultant thermal profiles on specimens NRC-5, NRC-12, NRC-14, and NRC-15 obtained using MR1111 as a program curve.

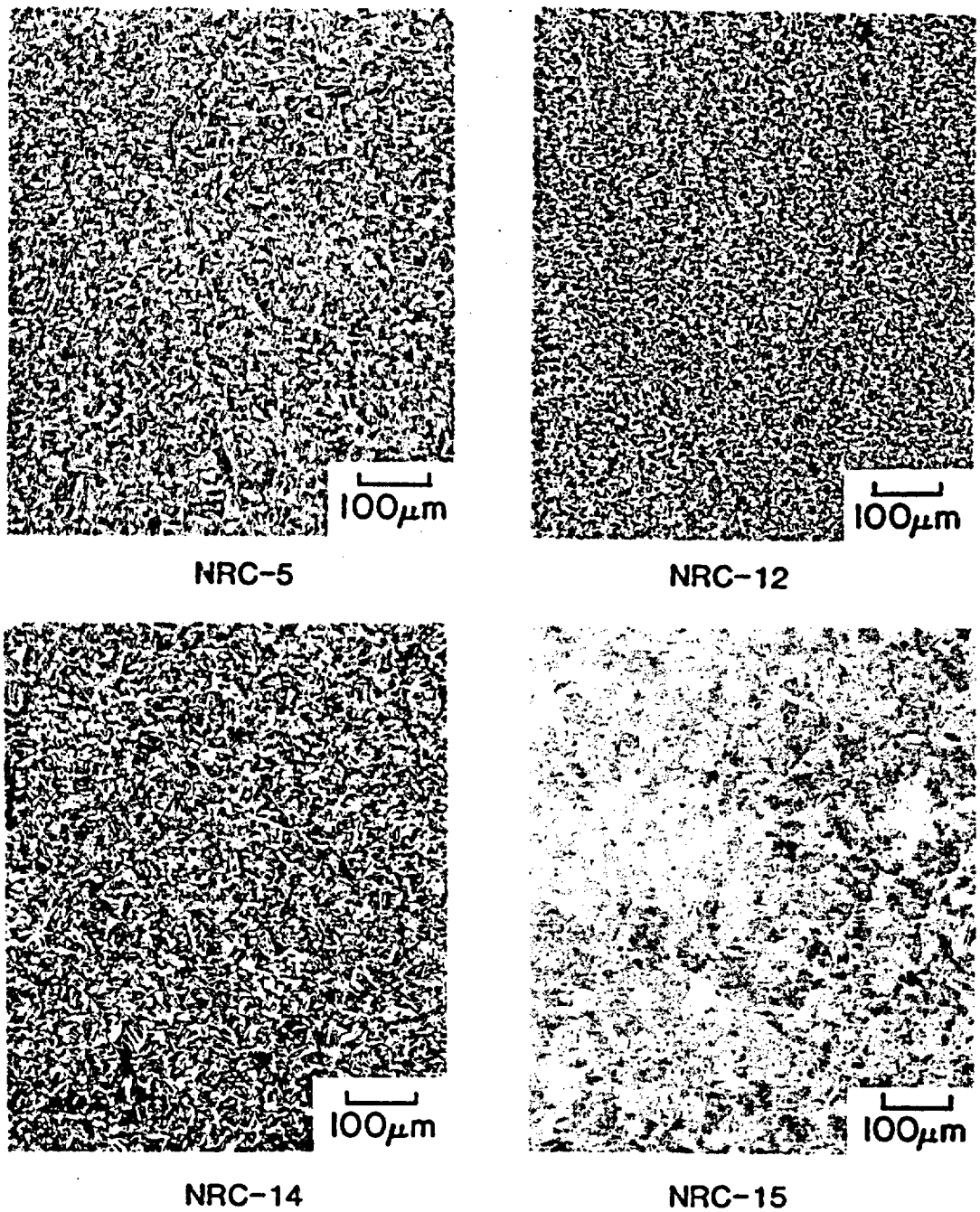

Figure 48b. A microstructural comparison showing NRC-5 and NRC-12 with equiaxed ferrite/pearlite, NRC-14 with acicular and Widmanstatten ferrite, and NRC-15 with upper bainite and allotriomorphic ferrite. The curves that generated these structures are in Figure 48a. 2% nital, 100x.

austenite grains are decorated by white allotriomorphic ferrite).

Figure 49a shows the thermal profiles obtained by using the empirically derived MR111 program curve. NRC-5 and NRC-12 specimens could not be obtained due to a material shortage; however, NRC-14 and NRC-15 were carried out. The peak temperatures obtained were: NRC-14, 1315°C; and NRC-15, 1330°C. The microstructures show (Figure 49b) heavy grain growth with the predominant phase in NRC-15 being upper bainite. NRC-14 shows a great deal of allotriomorphic ferrite, with grain centers being upper bainite. The effects of the chemical variations and cleanliness due to manufacturing have become apparent.

Figure 50a shows the measured thermal profiles on the empirically derived MR11092 program curve. The peak temperatures measured were: NRC-5, 1390°C; NRC-12, 1440°C; NRC-14, 1405°C; and NRC-15, 1460°C. The micrographs (Figure 50b) shown are very different. NRC-5 shows large prior austenite grains with allotrimorphic ferrite and Widmanstatten ferrite decorating the boundaries. There is upper bainite in the grain interiors with some acicular ferrite. NRC-12 shows more ferrite laths throughout the structure than NRC-5 and the upper bainite present is coarse.

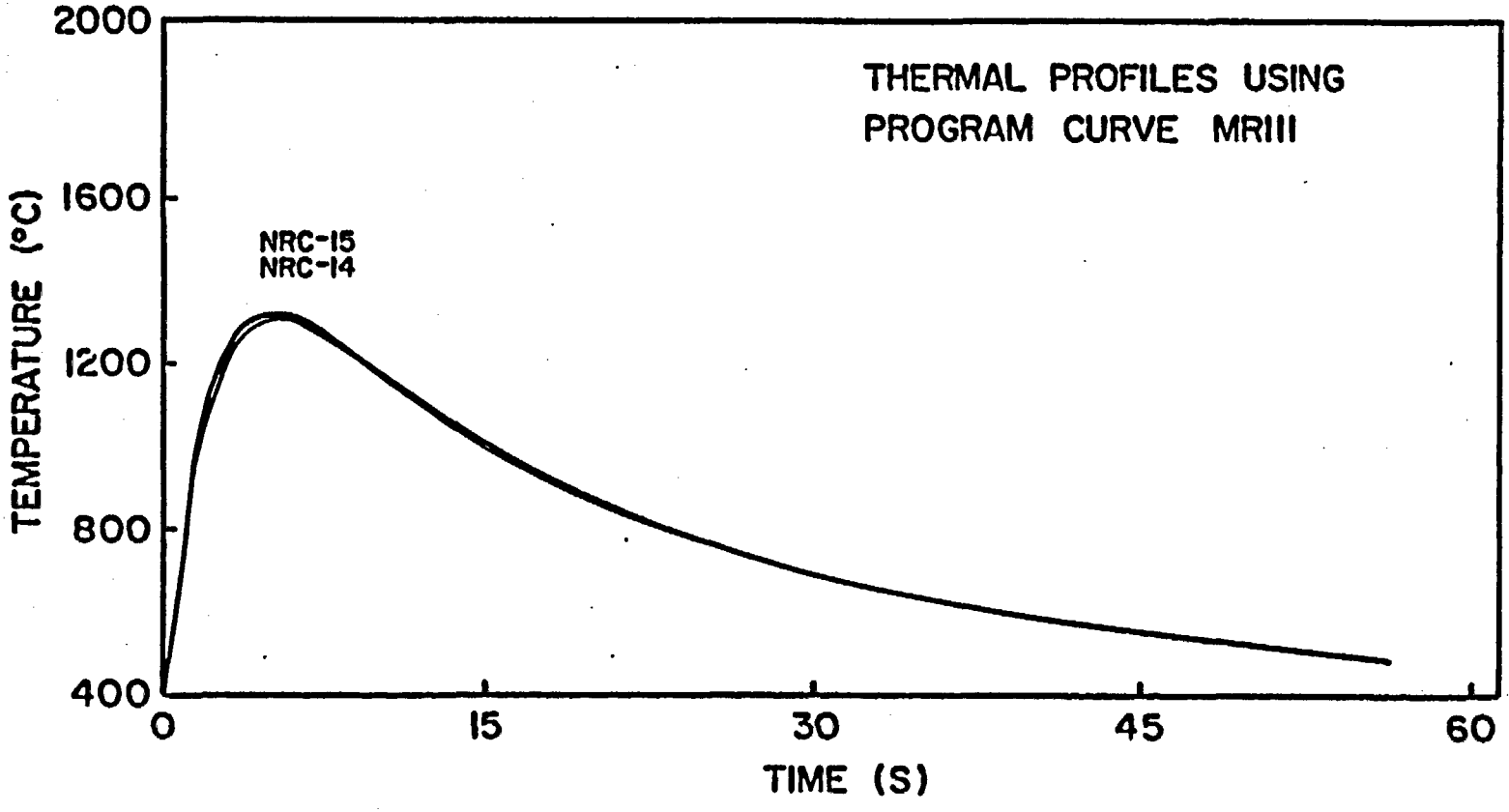

Figure 49a. The resultant thermal profiles on specimens NRC-14 and NRC-15 using MR111 as a program curve.

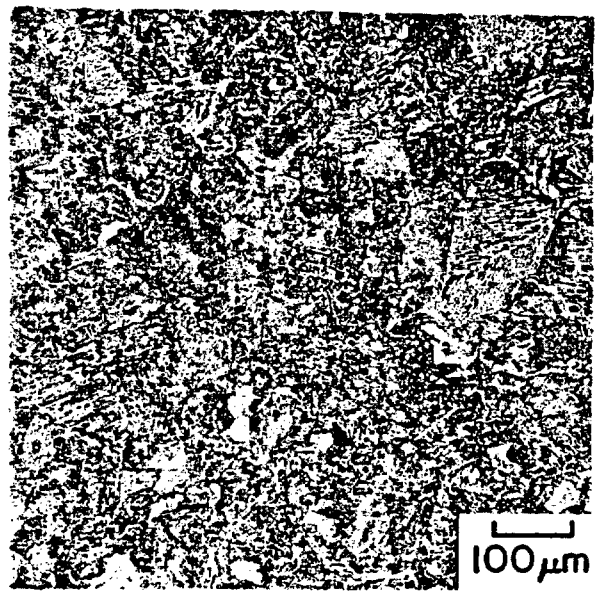

NRC-15

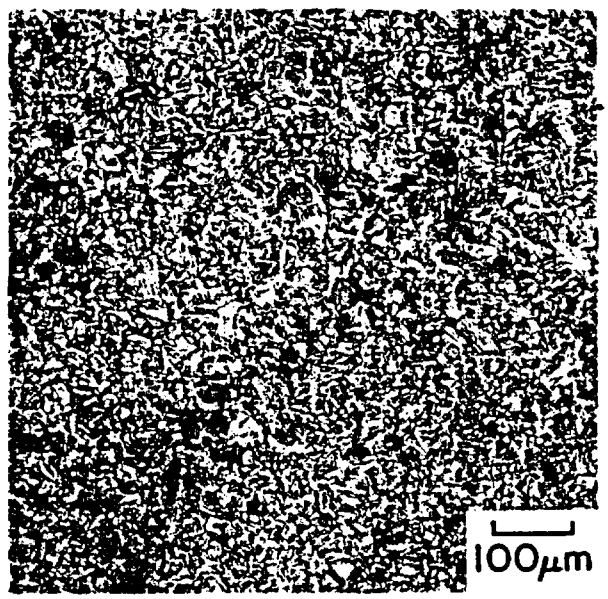

NRC-14

Figure 49b. A microstructural comparison showing NRC-15 with large prior austenite grains and upper bainite as a decomposition phase. NRC-14 with primarily Widmanstatten ferrite and pearlite. The curves that generated these structures are in Figure 49a. 2% nital, 200x.

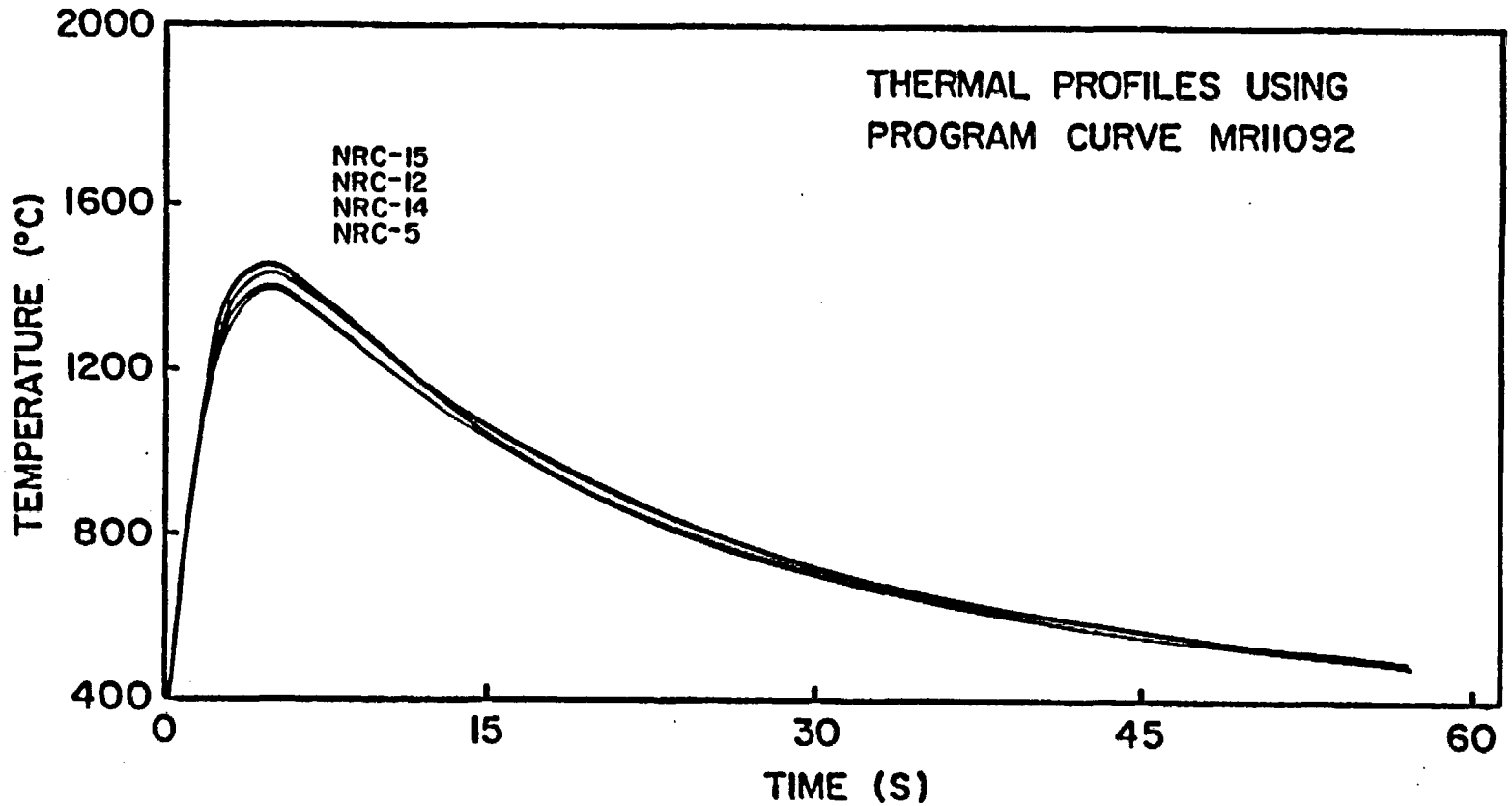

Figure 50a. The resultant thermal profiles on specimens NRC-5, NRC-12, NRC-14, and NRC-15 obtained using MR11092 as a program curve.

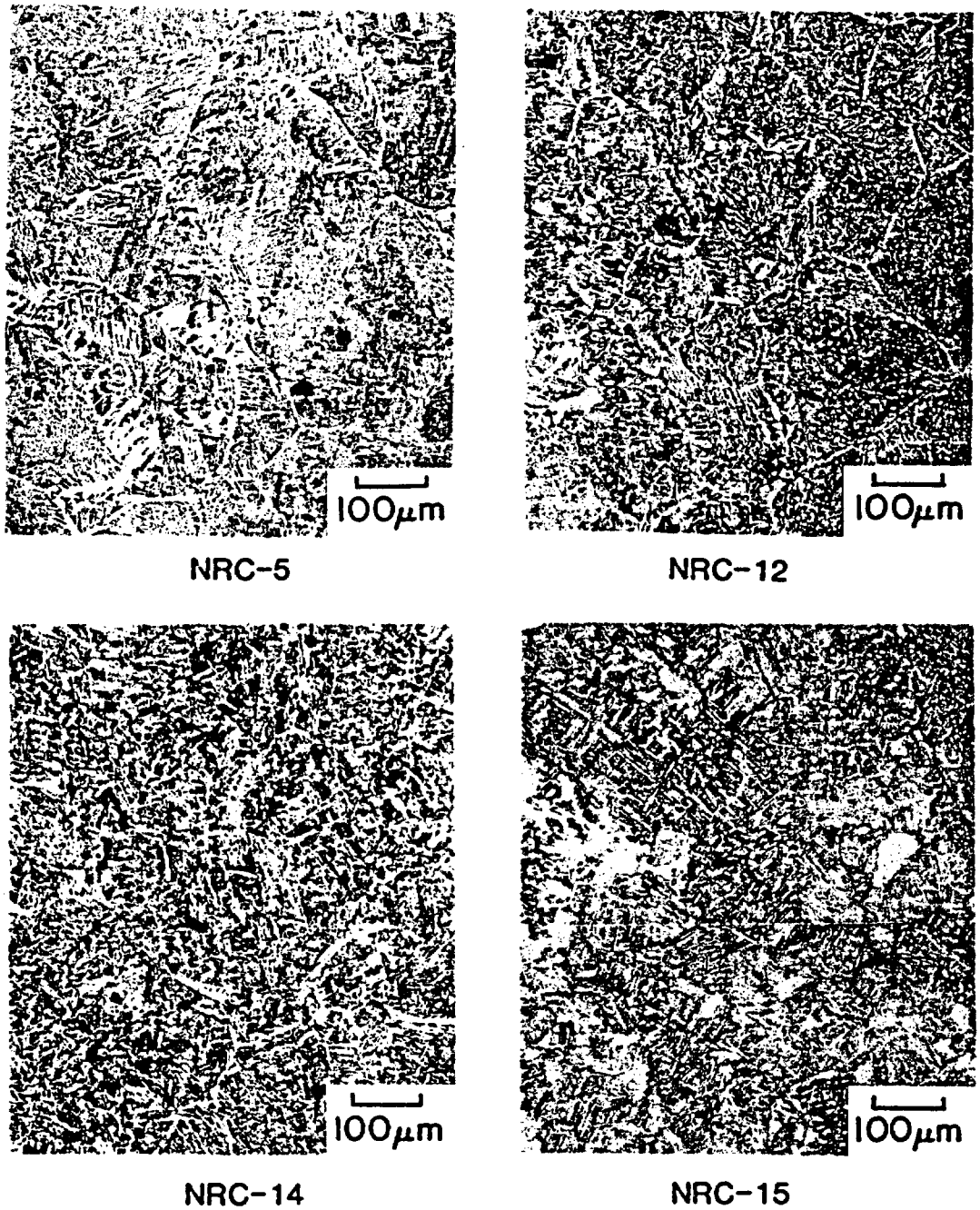

Figure 50b. A microstructural comparison between NRC-5, NRC-12, NRC-14 and NRC-15. All specimens show large prior austenite grains. The curves that generated these structures are shown in Figure 50a. Yorgason's etch, 100x.

NRC-14 shows smaller prior austenite grains than either NRC-12 or NRC-5 with a much coarser ferrite lath structure than either. NRC-15 shows predominantly fine upper bainite, with little or no allotriomorphic ferrite.

The aforementioned comparison proves that the Gleeble 1500 is a viable tool to produce specimens from selected areas of the heat affected zone. This being the case, specimens generated by the Gleeble 1500 can be used for further investigation. It was shown in the actual welds and reconfirmed using Gleeble simulation, that the microstructural changes brought about by alloy cleanliness variations become apparent only when peak temperatures exceed 1100°C. A discussion as to the kinetics and theory behind these microstructural changes is warranted.

3.5 HARDENABILITY THROUGH PROCESSING

As shown in the previous discussion, alloy and cleanliness variations only affect the final room temperature microstructure when peak temperatures exceed 1100°C. The analytical thermal profiles MR1111, MR111, and MR11092 generated specimens which typify regions of

the base plate heat affected zone that reached peak temperatures in excess of 1100°C. An explanation of the basis behind these observed microstructural variations comes from hardenability and nucleation theory.

Several factors affect the hardenability of the heat affected zone during the welding thermal cycle. Not only alloy content, such as percent manganese in solution, but austenite grain size, and number of nuclei for austenite decomposition.

Manganese is an austenite stabilizer, and an increase of manganese in solution pushes the nose of the CCT curve, Figure 29, to longer times (35). For the steels used in this investigation, this means that the austenite will decompose to bainite at high manganese contents and ferrite/pearlite at lower manganese levels, for a given weld thermal cycle where the peak temperature rises above 1100°C.

Grain size effects the hardenability of the heat affected zone with larger grains showing lower order transformation products. It has been shown that a fine dispersion of second phase particles are responsible for pinning austenite boundaries during weld thermal cycling (14). The commonly used precipitates designed to pin

austenite boundaries in microalloyed steels are Ti(C,N), Nb(C,N), AlN, and V(C,N). The grain growth in these steels during the weld thermal cycle, if not retarded, would be large enough to cause martensite formation upon austenite decomposition, where acicular ferrite is the desired structure. Since 80 percent of the grain growth occurs on the heat up cycle during welding, the microalloy precipitate is used as an austenite boundary pinner during this cycle. Eventually, the precipitate dissolves and the boundaries are unimpeded, and grow at a rapid rate. The effectiveness of a carbonitride as a grain boundary pinner is its solubility temperature in austenite. The solubilities of the common precipitates are shown in Figure 51 (14). It can be seen that TiN has the highest solubility temperature and, as such, is the best boundary pinner.

The steels of this investigation have only two possible significant boundary pinning constituents: AlN and Fe_3C. The aluminum nitrides are a result of the deoxidation practice. Aluminum is added as a deoxidant to fully killed steels; however, aluminum nitride, as well as aluminum oxide, forms. The aluminum nitride segregates to the austenite grain boundaries, and act as

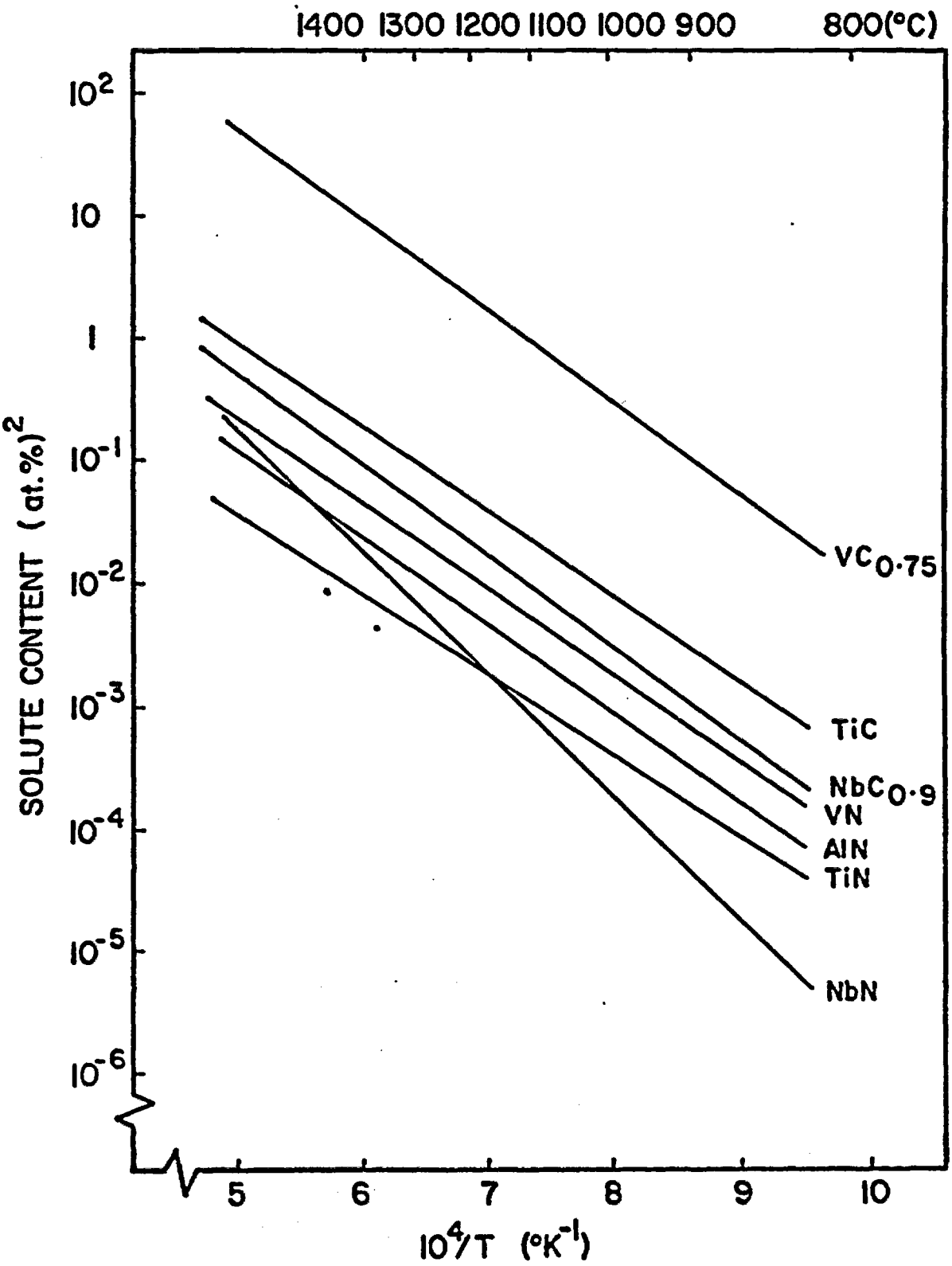

Figure 51. Solubility products of carbides and nitrides in austenite as a function of temperature (14).

obstacles to grain bouondary migration. The AlN solubility temperature is composition dependent at equilibrium conditions as shown in Figure 51. The solubility limits of this figure are not correct for the welding process. Equilibrium is not reached at the heating rates used and particle superheating occurs. Two possibilities become available: particles do not dissolve completely during the welding cycle, but some particle coarsening occurs, or particles completely dissolve. For the steels used in this investigation, no coarsening occurs for AlN, only dissolving. The time for AlN to dissolve at any given heating rate is shown in Figure 52. This means that large grains will form above approximately 1100°C for the heating rates of this welding process. The carbon content of this steel is 0.18 weight percent with an Fe_3C volume fraction of 11.5 percent. The carbides appear only in the pearlite prior to welding, so they do not affect the pinning of austenite grains.

The prior austenite grain size of the specimens thermally cycled by MR11092 was: NRC-15, 250 microns; NRC-14, 200 microns; NRC-12, 292 microns, and NRC-5, 289 microns. NRC-14 is considered a dirty steel, with many

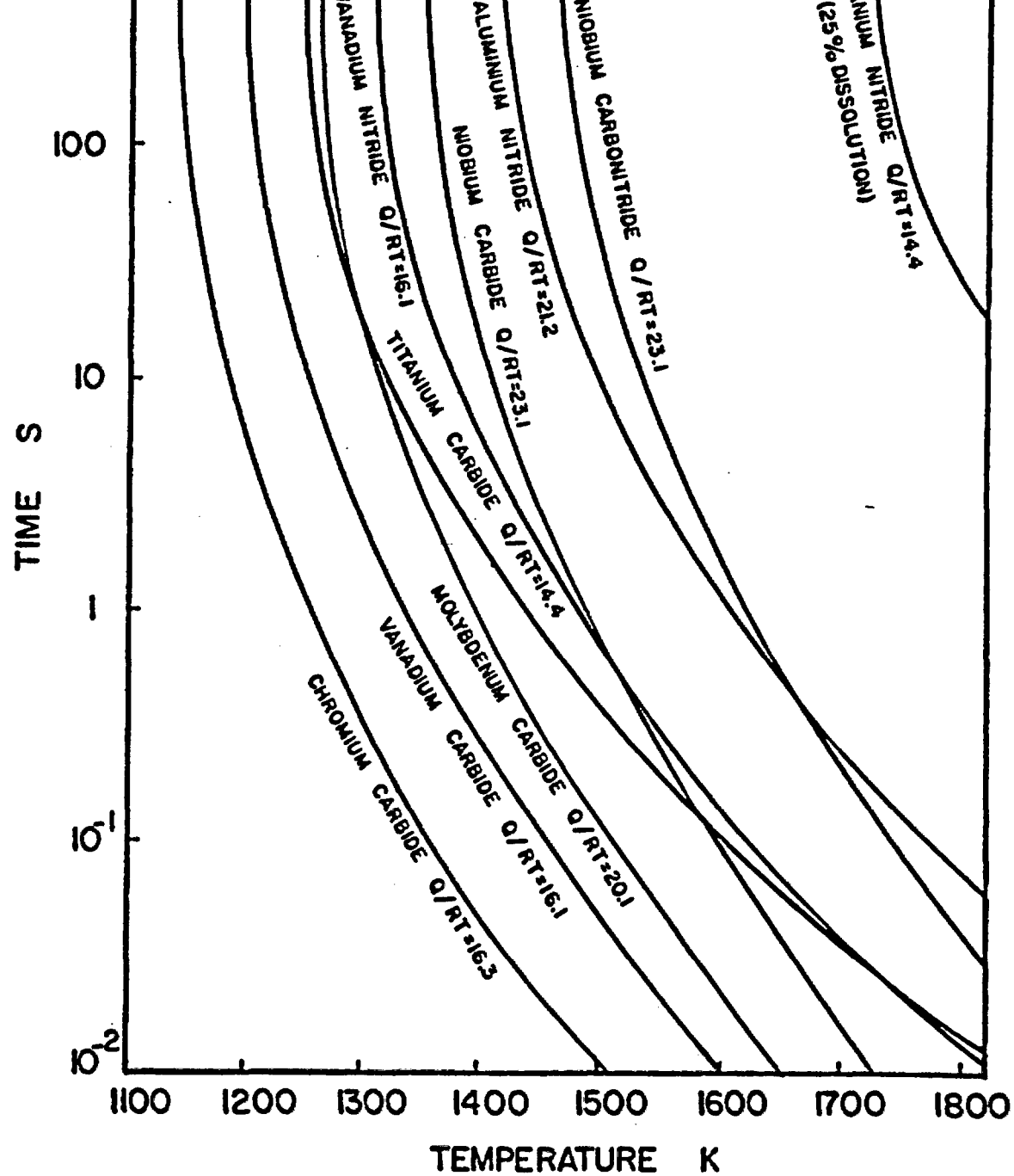

Figure 52. The times of complete dissolution of various carbides and nitrides as a function of temperature (14).

sulfides and oxides which are not normally considered effective austenite boundary pinners, but do act as obstacles to boundary motion. The high inclusion volume fraction in combination with AlN yield a finer prior austenite grain size than either NRC-12, NRC-5, or NRC-15. NRC-5 and NRC-12 both have very nearly the same oxygen content, sulfur content, and aluminum content and, consequently, the same prior austenite grain size.

The prior austenite grain size and the inclusion/matrix interfaces have a significant effect on the austenite decomposition products on cooling from temperatures above 1200°C. Not only do non-metallic inclusions partially affect the grain growth kinetics, but they play a significant role in determining the final austenite decomposition products. Upon heating, grain growth and particle dissolution are the dynamic features. Upon cooling, reprecipitation and nucleation are the dynamic features. The austenite grains have grown to 80 percent of their final size when cooling begins and the austenite decomposition products now depend on available nucleation sites. The non-metallic inclusions, oxides and sulfides, create interfaces for the nucleation of austenite decomposition products.

3.6 NUCLEATION

Nucleation in solids is almost always heterogeneous. Nucleation sites are non-equilibrium defects such as vacancies, dislocations, grain boundaries, stacking faults, inclusions, and free surfaces, all of which increase the free energy of the material (36). If the creation of a nucleus results in the destruction of a defect, some free energy ΔG_d will be removed, reducing the activation barrier. The equation for heterogeneous nucleation is:

$$\Delta G_{HET} = -V (\Delta Gv - \Delta Gs) = A\gamma - \Delta Gd \quad (36)$$

ΔGv = volume free energy of secondary phase

A = area of an interface between primary and secondary phase

γ = interfacial energy between two phases

ΔGs = misfit strain energy per unit volume

ΔGd = free energy due to destruction of a defect

V = volume of second phase

The optimum embryo shape which minimizes total interfacial free energy for an incoherent grain-boundary is two abutted spherical caps as shown in Figure 53. Where $COS\emptyset = \gamma_{\alpha\alpha}/2\gamma_{\alpha\beta}$. The excess free energy associated with the embryo is:

$$\Delta G = -V\Delta Gv = A_{\alpha\beta}\gamma_{\alpha\beta} - A_{\alpha\alpha}\gamma_{\alpha\alpha}$$

where $(A_{\alpha\beta}\gamma_{\alpha\beta} - A_{\alpha\alpha}\gamma_{\alpha\alpha}) = \Delta Gd$

The critical radius of the spherical caps will be $r^* = -2\gamma_{\alpha\beta}/\Delta Gv$. Also

$$\frac{V^*_{HET}}{V^*_{HOM}} = \frac{\Delta G^*_{HET}}{\Delta G^*_{HOM}} = S(\theta) \quad \text{(EQ 2)}$$

V^*_{HET} = critical nucleus size for heterogeneous grain boundary nucleation

V^*_{HOM} = critical nucleus size for homogeneous grain boundary nucleation

ΔG^*_{HET} = activation energy barrier for hetero geneous nucleation

ΔG^*_{HOM} = activation energy barrier for homo-geneous nucleation

$S(\theta)$ = shape factor

$S(\theta) = \frac{1}{2}(2 + \cos\theta)(1 - \cos\theta)^2$

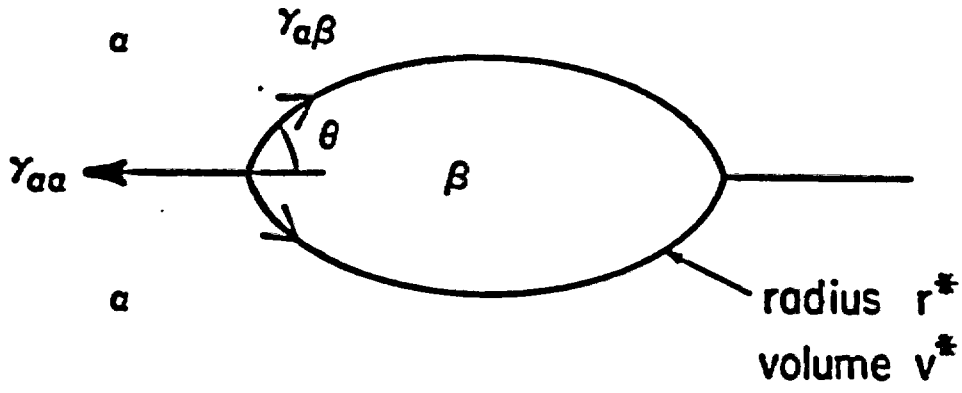

Figure 53. The critical nucleus size (V^*) for grain boundary nucleation.

The potency of a grain boundary as a nucleation site depends on the Cos ϕ; i.e., $\gamma_{\alpha\alpha} / \gamma_{\alpha\beta}$. If this ratio exceeds 2, there is no nucleation barrier (36).

ΔG^*_{HET} can be further reduced by the availability of inclusion/matrix interfaces, because of the high energy inclusion/matrix boundary (36).

The various nucleation sites in order of increasing ΔGd; i.e., decreasing ΔG^* are: 1) homogeneous sites, 2) vacancies, 3) dislocations, 4) stacking faults, 5) grain boundaries and interphase boundaries (inclusions), and 6) free surfaces. Nucleation should always occur on sites near the bottom of the list.

Upon cooling below 820°C, austenite has a thermodynamic desire to decompose to more stable phases. Ferrite will begin to form at the austenite boundaries under equilibrium cooling and will continue to form on cooling until the Al temperature is reached, where the remaining austenite transforms to pearlite. Under nonequilibrium cooling, various structures are possible. Austenite still has its thermodynamic desire to decompose but time is shortened, so at intermediate cooling rates allotrimorphic ferrite is formed at high angle prior

austenite grain boundaries, but these nucleation sites soon become saturated and the next available nucleation site is inclusion/matrix interface boundaries. Ferrite will nucleate here until those sites become saturated. This is seen in Gleeble sample 12-MR11092 where the allotriomorphic ferrite saturated the boundary sites but, due to the undercooling, had no time to grow and more ferrite was nucleated at the inclusion/matrix interfaces.

Lower order nucleation sites become active with the higher degree of undercooling. If very few nucleation sites for ferrite are available or the cooling is high, bainite would form starting from the austenite boundary. Since the undercooling is large, this ferrite would take on a Widmanstatten morphology. As the ferrite lath thickens, the carbon content of the adjacent austenite increases and finally reaches a level where cementite nucleates and grows. This upper bainite is seen in the Gleeble specimen 15-MR11092. There is very little allotriomorphic ferrite and there are few inclusion/ matrix interfaces so bainite is nucleated at the austenite boundaries.

NRC-12 has more inclusion matrix interfaces in combination with high angle grain boundaries than does NRC-15. It is beyond the scope of this research to quantify the amount of nucleation sites, but, as seen by the micrographs of Figure 49, NRC-12 has more high energy nucleation sites than NRC-15.

The type of inclusions as shown by the scanning electron microscope are MnSiO, Al_2O_3 and MnS. The oxygen contents of the steels quoted in Table IV incorporate interstially dissolved oxygen as well as oxide inclusions. The varying oxygen contents of the steels used were controlled in two ways: with a carbon monoxide boil, and by Aluminum additions prior to pouring the molds. The Al_2O_3 oxide was the product of deoxidation prior to final tapping. The amount of Al_2O_3 was controlled by pouring intervals. In the high oxygen steels; (i.e., high Al_2O_3), the ladle was tapped to the molds thirty seconds after the aluminum addition. Al_2O_3 had no time to float into the slag and be removed, and thus became trapped in the steel. In the low oxygen steels, the ladle was tapped into the molds two minutes after the aluminum addition allowing Al_2O_3 to float and be removed. The

$MnSiO_2$ oxide inclusion is also effective in controlling dissolved oxygen through manganese and silicon additions as shown in the introduction. This inclusion type was controlled through alloy additions as previously described. The MnS inclusion is the product of manganese reacting with sulfur. This is desirable because sulfur in the absence of manganese forms an iron sulfide eutectic which causes hot shortness in steels; however, sulfur is best avoided due to its poor corrosion properties and its detriment to impact properties.

The three inclusion types present all have an effect on the austenite decomposition products and austenite grain growth kinetics. Only when peak temperatures exceed 1100°C do these inclusions play a role in austenite decomposition. The inclusion/matrix interface, which provides the best nucleation site for higher order transformation products (ferrite/pearlite) was not investigated and this may be the subject of future work.

The process parameters; alloy chemistry, cleanliness, initial solidification processing, as well as heat treating, and welding must be controlled in order to predict container microstructure. Since microstructure is the key to this performance, the chosen

manufacturing process must control the above variables to insure that the overpack container will meet its design life criteria. With the production process variables discussed in this study, steel can be produced to a predicted microstructure. Further study should utilize the production processes and evaluate which microstructure through the fabrication of mechanical or corrosion test specimens will be susceptible to failure during the service life of the overpack container.

4.0 CONCLUSIONS

1. Centrifugal casting is the most economical process for the production of carbon steel overpack containers for high level nuclear waste disposal.

2. The thermal experience of the heat affected zone for a specific submerged arc welding process can be measured using a Nicolet 4094 digital recording oscilloscope.

3. Rosenthals three dimensional heat transport equation, incorporating alterations in thermal conductivity, can be used to describe the heat affected zone thermal experience of a specific submerged arc welding process on cast and normalized low carbon steel.

4. Chemical composition and alloy cleanliness control the microstructure, by altering austenite decomposition nuclei in the heat affected zone of steel within the ASTM A-216 grade WCA

specification when peak temperatures exceed 1100°C, but show no significant influence when peak temperatures are below 1100°C.

5. Chemical composition and alloy cleanliness variations on steels within the ASTM A-216 grade WCA specification show no influence on microstructure in the as-cast condition, and in the normalized condition.

6. The Gleeble 1500 weld simulator can duplicate the microstructure of specific regions in the heat affected zone of submerged arc welded, cast and normalized low carbon steels.

REFERENCES

1. American Society for Testing and Materials 1977, A216 grade WCA.

2. United States Steel, The Making Shaping and Treating of Steel, Herbick and Held, Pittsburgh, PA., 1971.

3. Wlodawer, R., Directional Solidification of Steel Castings, Pergammon Press, New York.

4. Heine, Loper, and Rosenthal, Principles of Metal Casting, Second Edition, McGraw Hill, New York, 1967.

5. Flinn, R. A., Fundamentals of Metal Casting, Addison Wesley, 1963.

6. Vennard, J. K., and Street, R. L., Elementary Fluid Mechanics, John Wiley & Sons, Inc., 1961.

7. Beeley, P. R., Foundry Technology, Butterworths, London, 1972.

8. Taylor, H. F., Flemings M. C., Wulff J., Foundry Engineering, John Wiley and Sons, Inc. Inc., New York, 1959.

9. Habraken, L. and Brouwer J. L., De Ferri Metallographia, Volume I, W. B. Saunders Co., 1966.

10. Flemmings, M. C., Solidification Processing, McGraw Hill, 1974.

11. American Welding Society, Structural Welding Code, ANSI/AWS D1.1-85, 1985.

12. American Welding Society, Welding Handbook, Seventh Edition, Volume 2, 1978.

13. American Society for Metals, Metal Handbook, Volume 6, Ninth Edition, American Society for Metals, Metals Park, Ohio, 1983.

14. Easterling, K. E., Introduction to the Physical Metallurgy of Welding, Butterworth and Co., London, 1983.

15. Leslie, W. C., The Physical Metallurgy of Steels, McGraw Hill, 1981.

16. Rosenthal, D., "Mathematical Theory of Heat Distribution During Welding and Cutting," Welding Research Supplement, May 1941.

17. American Society for Metals, Metal Handbook, Volume 7, Eighth Edition, American Society for Metals, Metals Park, Ohio.

18. Bethlehem Steel, Modern Steels and Their Properties, Bethlehem Steel Corp.

19. Ashby, M. F., Easterling, K. E., "A First Report on Diagrams for Grain Growth in Weld," Acta Metallurgica, Volume 30, pp. 1969-1978.

20. American Society for Metals, Metals Handbook, Volume 2, Eighth Edition, 1972, Metals Park, Ohio.

21. Brown, E., and Nichting, R., Colorado School Mines, Department of Metallurgical Engineering, Golden, CO. Private Communication, unpublished work, November 1984.

22. Omega, Temperature Measurement Handbook and Encyclopedia, Omega Engineering, Stamford, CT, 1985.

23. Fenton, A. W., " The Traveling Gradient Approach to Thermocouple Research " Specialized Techniques in Thermocouple Thermometry, 1971

24. American Institute of Physics, Tempreature, Its Measurement and Control in Science and Industry, Volume II, 1972.

25. American Society for Testing and Material, Manual on the Use of Thermocouples in Temperature Measurement, ASTM special publication, 470 A, 1974.

26. Analog Devices, Four-Channel, Isolated Thermocouple /mV Conditioners, Pamphlet, Norwood, Massachusetts.

27. Yorgason, R. A., Colorado School of Mines, Department of Metallurgical Engineering, Golden, CO. Private Communication, unpublished work, August 1985.

28. Yorgason, R. A., Colorado School of Mines, Department of Metallurgical Engineering, Golden, CO. Private Communication, September 1985.

29. Kohno, R., Jones, S. B.," An Initial Study of Arc Energy and Thermal Cycles in the Submerged Arc Welding of Steel" Welding Institute Research Report, Dec. 1978.

30. Tsai, C. L., "Modeling of Thermal Behaviors of Metals During Welding," Conference Proceedings, ASM, Metals Park, Ohio, 1982.

31. Touloukian, Y. S., Thermophysical Properties of Matter, Volume 4, Specific Heat, IFI/PLENIUM, 1970.

32. Geiger, G. H., and Poirier, D. R., Transport Phenomena in Metallurgy, Addison-Wesley, 1973.

33. Pokorny, Annick and Jean, De Ferri Metallographia, Volume 3, W. B. Saunders Co., 1967.

34. Atkins, M., Atlas of Continuous Cooling Transformation Diagrams for Engineering Steels, American Society for Metals, 1980.

35. Krauss, G., Principles of Heat Treatment of Steel, ASM, Metals Park, Ohio, 1980.

36. Porter, D. A., and Easterling, K. E., Phase Transformations in Metals and Alloys, Van Nostrand Reinhold Co. Ltd., Berkshire, England, 1982.

APPENDIX A

Basalt. Current design concepts for the BWIP waste package are accurately reflected in SD-BWI-CDR-004 REV 0-0[1] according to M.J. Smith, Rockwell Handford Operations Waste Package Department. That document describes a reference waste package design and 2 alternate designs for each waste form. The Reference Design calls for a carbon steel overpack directly over the waste canister for DHLW and CHLW and of direct placement of SF2 into the overpack. Dimensions of the waste forms and overpack for the Reference Design are given below:

Waste Form Dimensions	DHLW	SF2	CHLW
Diameter, cm	61.0	30.5	32.5
Length, cm	300	385	305
Weight, kg	1932	1908	845
Waste Content per Package, kg	1470	1380	595
Overpack Dimensions			
Inside Diameter, cm	63.5	30.5	35
Wall Thickness, cm	8.7	5.6	5.3
Outside Diameter, cm	80.9	41.7	45.6
Head Thickness, cm	15.0	8.5	8.6
Length, cm	333	405	325
Empty Weight, tonne	5.90	2.19	1.84
Loaded Weight, tonne	7.83	4.17	2.68

The Alternate I waste package design incorporates backfill between the waste form and overpack. Waste form, backfill and overpack dimensions for Alternate I are given below:

Waste Form Dimensions	DHLW	SF2	CHLW
Canister Diameter, cm	61.0	32.4	32.4
Canister Length, cm	300	417	305
Weight, kg	1932	2210	840

Backfill Dimensions			
Inside Diameter, cm	64	36	36
Outside Diameter, cm	94	66	66
Weight, kg	2250	2065	1580
Overpack Dimensions			
Inside Diameter, cm	96.5	68.6	68.6
Wall Thickness, cm	12.4	9.9	8.9
Outside Diameter, cm	121.3	88.4	86.4
Head Thickness, cm	22.3	16.7	15.7
Length, cm	382	488	369
Empty Weight, tonne	15.2	10.2	7.1
Loaded Weight, tonne	19.7	14.0	9.6

The Alternate II waste package design is a self-shielded package with the following features:

Waste Form Features	DHLW	SF2	CHLW
Number of Waste Forms	2	4	3
Waste Form Diameter, cm	61.0	21.5 Sq.	32.5
Waste Form Length, cm	300	410	305
Waste Form Weight, kg	3864	8100	2535
Waste Content per Package, kg	2940	3688	1785

Overpack Features	DHLW	SF2	CHLW
Cross Section Geometry	Rectangle	Square	Triangle
Inside Dimensions (s), cm	63.5 x 127	48	70
Outside Dimensions (s), cm	129.5 x 193	128	146
Length, cm	383	511	400

APPENDIX B

Riser Calculation for Cylindrical Overpack Container.

Assumption:

1) No heat is extracted through the central core.
2) Neglect the riser/casting interface for modulus calculations.
3) Assume dimensions shown in Appendix A and diagram in Figure 1.
4) The riser will be open to the air and placed as schematically shown in Figure 1.

List of Variables:

M_C = Modulus of the casting (cm)
V_C = Volume of casting (cm^3)
A_C = Area of casting (cm^2)
D_{ic} = Inside diameter of casting (cm)
D_{OC} = Outside diameter of casting (cm)
M_R = Modulus of riser (cm)
V_R = Volume of riser (cm^3)
A_R = Area of riser (cm^2)
D_{Ri} = Inside diameter of riser (cm)
D_{Ro} = Outside diameter of riser (cm)
L_C = Length of casting (cm)
L_R = Length of riser (cm)

Calculation:

$$M_C = V_C/A_C$$

$$V_C = \pi(D_{OC}/2)^2 L_C - \pi(D_{ic}/2)^2 L_C$$

The length of the casting used in these calculations should be 363 cm to allow for riser and gate removal.

$$V_C = [(80.9/2)^2 - (63.5/2)^2]\ 363\pi = 716330\ cm^3$$

$A_C = \pi(D_{OC}/2)^2 - \pi(D_{ic}/2)^2 + \pi(D_{OC})(L_C)$

$A_C = \pi[(80.9)/2)^2 - (63.5/2)^2 + (80.9)(363)] = 94232\ cm^2$

$M_C = V_C/A_C = 7.60\ cm$

$M_R = 1.2\ M_C = 9.12$

$V_R = [(D_{RO}/2)^2\ L_R - (D_{Ri}/2)^2\ L_R]\pi$

$A_R = 2\pi[(D_{RO}/2)^2 - (D_{Ri}/2)^2] - \pi[(D_{OC}/2)^2 - (D_{ic})^2] + \pi D_{RO}\ L_{RO}$

Let the height of riser, L_R equal D_{RO}.

$V_R = \pi[D_{RO}^2/4\ D_{RO} - D_{Ri}^2/4\ D_{RO}]$

$A_R = \pi(3/2\ D_{RO}^2 - 1/2\ D_{Ri}^2 - 628)$

$M_R = V_R/A_R$

$$M_R = \frac{[D_{RO}^3 - D_{Ri}^2\ D_{RO}]}{6D_{RO}^2 - 2D_{Ri}^2 - 2513}$$

Solving iteratively and letting $D_{Ri} = D_{ic}$:

$D_{Ri} = 88.1\ cm = L_R$

This is difficult to mold and feeding is poor with the riser offset. It should appear in the middle of the section to be fed as shown in Figure 1. More selective iterations of the equation for M_R yields the following results:

Riser dimensions	D_{RO}(cm)	D_{Ri}(cm)	L_R(cm)
	85	59.5	85

APPENDIX C

COLORADO SCHOOL OF MINES
Department of Metallurgical Engineering

MT 300 FOUNDRY METALLURGY Dr. Frost

CHARGE CALCULATION FOR STEEL MAKING

This calculation is an itterative method of determining the charge weights of melt stock, pig iron, and ferro alloys to give a specific steel composition. The charge calculation sheet provides for two itterations which will give sufficient accuracy for most steel charge calculations. The calculation sheet also provides a vehicle for record keeping. Space is provided at the top of the sheet for recording the chemical analysis of all charge components, and the overall sheet format provides a good record of the charge calculation. Any calculations such as the solution of the simultaneous equations for the carbon balance should be performed on the reverse side of the sheet, so that they will be included in the record.

In some cases one or more of the charge components will contain large amounts of a secondary element. That is, an element which the particular alloy was not intended to provide. For example, ferromanganese usually contains carbon as a secondary element. In such cases the two itterations provided on the sheet may not give sufficient accuracy, and three or more successive approximations may be required. These can be easily performed using additional charge calculation sheets as described in Part E below.

A. Charge Requirements:

Determination of the charge requirement includes conversion of the desired chemistry to weights of the various elements in the alloy, and accounting for elements contained in the scrap and expected losses during melting.

1. Enter the analyses of the various charge components at the top of the sheet.

2. Enter the total charge weight (line 1), the desired alloy analysis (line 2), and the expected losses during melting (line 3). The expected losses are based on experience or on prior heat records.

3. Add the expected losses to the desired analysis to calculate the charge analysis (line 4).

4. Multiply the charge analysis for each element (decimal fraction) by the total charge weight to determine the charge weight for each element (line 5). NOTE: The chemical analyses are listed in weight % for convenience, but decimal fractions should be used for all calculations.

5. Enter the scrap weight (line 6), and determine the weights of the alloy elements contained in the scrap (line 7).

6. Subtract the weights of the elements in the scrap (line 7) from the charge weights (line 5) to determine the calculated charge weights of the elements (line 8). The "Calculated Charge Weights of the Elements" line represents the weights of the elements that must come from the bar stock, the pig iron, or from the ferro alloys.

B. First Approximation to the Charge:

The first approximation to the charge is made by assuming that 100% of each alloy element will be provided by its respective ferro alloy, and by using a carbon balance to determine the relative weights of bar stock and pig iron.

7. Divide the charge weight of each element except carbon (line 8) by its ferro alloy purity to determine the initial estimate of the ferro alloy charge weights. Enter the ferro alloy weights in Column II. (The alloy purities come from the table at the top of the page. Use decimal fractions for the calculations.)

8. Total the weights of the ferro alloys (line 20), and enter this total in the blank space "Calc. Alloy" in the calculation at the bottom right hand corner of the page.

9. The calculation at the bottom of the page is a carbon balance to determine the first estimate of the weights of pig iron and bar stock to provide the right carbon analysis for the alloy. First, the combined weight of pig iron plus bar stock (W) is calculated by subtracting the weights of scrap and ferro alloys from the total charge weight. The weight of bar stock (X) and the weight of pig iron (Y) are then calculated using a carbon balance. Solve the simultaneous equations and enter the weights of pig iron and bar stock in the spaces provided at the bottom and at the top of Column II. Use the reverse side of the sheet for calculations. Column II represents the first approximation to the charge weights.

C. Calculation of the Final Charge:

The final charge in Column I is a refinement of the approximate charge in Column II. It is designed to account for the fact that many elements occur in several of the charge alloys. For instance, carbon occurrs in the bar stock, pig iron, ferro manganese, and in the ferro chromium. The first approximation was based on the assumption that 100% of each element would be provided from its ferro alloy. The amount of the element present in other charge components would, therefore, represent an excess or overcharge. The

total amount of each element from all sources is determined using the table to the right of Column II. The residual or excess amount of each element or equivalent amount of ferro alloy are calculated on lines 21 and 22. These values are used to correct the first approximation charges in Column II to give the final charge weights in Column I.

10. Use the charge weights in Column II and the alloy chemistries at the top of the page to calculate the weights of the elements present in each alloy, and fill in the table to the right of Column II. The enclosed boxes represent the weight of each element present in its own ferro alloy.

11. Determine the excess or residual amount of each alloy. Total the weights present in the table for each element (line 20 at the bottom of the table), and subtract the required charge weight (line 8) to give the residual amount of each element (line 21).

12. Convert the residual element weights to equivalent ferro alloy weights. Divide the residual element weight (line 21) by the purity (decimal fraction of the element contained) of the respective ferro alloy at the top of the page, and enter the excess ferro alloy weight on line 22.

13. Correct the charge weights in Column II by subtracting the excess ferro alloy weights (line 22), and enter the final charge weights in Columnn I. Adjust the weight of the pig iron in the same manner to account for excess carbon that occurs in ferro alloys such as FeMn.

14. Total the excess ferro alloy weight (line 22), and enter the total on line 23. This is equal to the total weight of adjustments made to the ferro alloys and the pig iron. Add this total excess ferro alloy weight to the weight of the bar stock in Column II, and enter the final charge weight of bar stock in Column I.

15. Enter the scrap weight (line 6) on line 9 of Column I.

16. Total the final charge weights in Column I and enter on line 19. This should equal the total charge weight called for on line 1.

D. Checking the Accuracy of the Calculated Charge:

The accuracy of the final charge in Column I may be checked using a second charge calculation sheet. Enter the final charge weights from Column I of the first sheet in Columnn II of the second sheet. Multiply the charge weights by the respective analyses and fill in the table with the weights of every element contained in each of the charge components. The total charge weight of each element should equal or be close to the required charge weight on line 8 of the first sheet. If the charge weights are not sufficiently accurace, then a third itteration may be necessary (see E below).

E. Third Itteration to Refine the Charge Calculation:

A third refinement of the charge calculation is sometimes required where large amounts of secondary elements are present in one or more of the charge components. The third refinement is made using a second charge calculation sheet.

1. Copy the calculated charge weights of the elements from line 8 on the first sheet to line 8 on the second sheet.

2. Copy the charge from Column I of the first sheet to Column-II of the second sheet, and calculate the weights of the elements present in the various charge components to fill out the table to the right of Column II as described in Part D above.

3. Total the charge weights for each element in the table and place the totals on line 20.

4. Subtract the calculated charge weights on line 8 from the total charge weights on line 20, and place the result on line 21. A positive value on line 21 indicates an overcharge, and a negative value indicates an undercharge.

5. Convert the element weights on line 21 to equivalent ferro alloy weights by dividing by the decimal purity of the ferro alloy, and place the result on line 22. Correct for undercharges or overcharges by adding or subtracting the ferro alloy weights on line 22 from the charge weights in Column II, and place the final charge weights in Column I.

6. Add the ferro alloy corrections on line 22 (accounting for the signs), and enter the total on line 23. If the sign on the total is (+) more corrections were made for overcharging than for undercharging, and the total on line 23 should be added to the bar stock weight. If the sign is (-) more corrections were made for undercharging, and the total should be subracted from the bar stock weight.

CHEMICAL ANALYSIS	C	Mn	Si	Cr	Mo	Ni
BAR STOCK ANALYSIS (%)						
PIG IRON ANALYSIS (%)						
FeMn (%)						
FeSi (%)						
FeCr (%)						
FeMo (%)						
Ni (%)						

TOTAL CHARGE Wt.	C	Mn	Si	Cr	Mo	Ni
DESIRED ANALYSIS (%)						
EXPECTED LOSSES (%)						
CHARGE ANALYSIS (%)						
CHARGE Wt. ELEMENTS						
SCRAP Wt.						
ELEMENTS IN SCRAP						
ELEMENTS CALCULATED						

(I) CHARGE WEIGHT ALLOY	SCRAP	(II) CALC. FERRO ALLOY WEIGHT (Kg)	C	Mn	Si	Cr	Mo	Ni
	BAR	X=						
	PIG	Y=						
	FeMn							
	FeSi							
	FeCr							
	FeMo							
	Ni							
	TOTAL							

	C	Mn	Si	Cr	Mo	Ni
RESIDUAL ELEM. IN ALLOYS						
ELEM. CONV. TO FERROALLOY						
TOTAL EXCESS FERROALLOY		ADD TO Wt. OF BAR STOCK				

HEAT No._____ Carbon Balance
ALLOY_____
MELTER_____
DATE_____

X= Wt. of bar stock
Y= Wt. of pig iron
C= Calc. wt. of carbon
W= (1)_____ - (2)_____ - (19)_____
total wt. scrap calc. alloy

X + Y = W X=_____

APPENDIX B - QAD-CSM-1 - STEELMAKING MELT LOG

Heat Number____________________ Date____________________

Alloy Type ____________________ Melter____________________

Melt Log	Time	Temp	Comments
Power On			

Charge	Lot	Weight
Bar		
Scrap		
Pig		
Carbon		
FeMn		
FeSi		
FeCr		
FeMo		
Ni		
Al		

Element	Desired	Charge
C		
Mn		
Si		
Cr		
Mo		
Ni		
Al		

Elem	Chem	Charge	Loss
C			
Mn			
Si			
Cr			
Mo			
Ni			
Al			

Heat Size____________________

Total Molds____________________

Total Castings____________________

Ladle____________________

Hot Top____________________

Furnace Number____________________

Lining Type____________________

Number of Heats____________________

Condition____________________

Other____________________

Remarks:

APPENDIX D

```
10 CLS : LOCATE 9,15 : PRINT "THIS IS TCONV.BAS A TEMPERATURE CONVERSION PROGRAM
"
12 LOCATE 15,22: PRINT "   DO YOU NEED INSTRUCTIONS (Y/N)?" : GOSUB 136
14 IF A$ ="Y" OR A$ ="y" THEN GOSUB 144
16 LOCATE 1,1,0
18 KEY OFF : OPTION BASE 1 :DEFINT A-Z : DEFSNG N: DEFDBL A,T
20 DIM N(11),D(7940),PD(793)
22 REM ------------------------------------------------------------------
24 CLS : LOCATE 11,28 : PRINT "CHOOSE THERMAL COUPLE TYPE"
26 PRINT TAB(35) "<1> TYPE R":PRINT TAB(35) "<2> TYPE K"
28 PRINT TAB(35) "<3> TYPE T":PRINT TAB(35) "<4> TYPE E"
30 PRINT TAB(35) "<5> TYPE J":PRINT TAB(35) "<6> TYPE S"
32 PRINT TAB(35) "<7> TYPE C"
34 LOCATE 25,28 : PRINT  "PRESS THE APPROPRIATE NUMBER"
36 GOSUB 138 : CLS : LOCATE 12,30 : PRINT "INTIALIZING"
38 IF VAL(A$) <1 OR VAL(A$)>7 THEN 24
40 FOR K = 1 TO VAL(A$) : READ A0,A1,A2,A3,A4,A5,A6,A7,A8,A9:NEXT K
42 REM ------------------------------------------------------------------
44 CLS : LOCATE 12,1 : PRINT "WHICH DISK WILL THE DATA FILES BE READ OFF OF?"
46 GOSUB 136 : DR$=A$
48 CLS : LOCATE 12,1 : PRINT "WHICH DISK WILL THE DATA FILES BE STORED ON?"
50 GOSUB 136 : DS$=A$
52 CLS : LOCATE 12,1 : PRINT"WAS THE ISOLATION AMPLIFIER USED (Y/N)?"
54 GOSUB 136 : IF A$="N" OR A$="n" THEN AMP = 1! : GOTO 58
56 LOCATE 13,1 :INPUT "enter the iso-amp constant";AMP
58 CLS : FILES DR$+":*.NOR"
60 PRINT CHR$(13)"THESE ARE THE FILES AVAILABLE TO WORK WITH"CHR$(13)CHR$(13)
62 INPUT "ENTER THE FILE TO BE CONVERTED <EXLUDE EXTENSION!>";F$
64 REM ------------------------------------------------------------------
66 CLS : LOCATE 12,30 : PRINT "LOADING ";F$
68 BLOAD DR$+":"+F$+".NOR",VARPTR(N(1))
70 BLOAD DR$+":"+F$+".DAT",VARPTR(D(1))
72 REM ------------------------------------------------------------------
74 CLS : LOCATE 12,29 : PRINT "ELIMINATING POINTS"
76 I=-9
78 FOR J = 1 TO 793 : I = I+10 : PD(J) = D(I): NEXT J
80 ERASE D : DIM T(793)
82 REM ------------------------------------------------------------------
84 CLS : LOCATE 12,28  : PRINT "CALCULATING TEMPERATURES"
86 FOR J = 1 TO 793
88       T(J) =  ( PD(J) - N(7) ) * N(5)/AMP
90       T(J) = A0+A1*T(J)+A2*T(J)^2+A3*T(J)^3+A4*T(J)^4+A5*T(J)^5+A6*T(J)^6
                +A7*T(J)^7+A8*T(J)^8+A9*T(J)^9
92 NEXT J
94 REM ------------------------------------------------------------------
96 CLS : LOCATE 11,18: PRINT "SAVING TEMPERATURE FILE ";F$;".TMP ON DISK ";DS$
98 BSAVE DS$+":"+F$+".TMP",VARPTR(T(1)),6344
100 CLS : LOCATE 5,1 : PRINT "      DISK ";DR$;" FILES:"
102 FILES DR$+":*.NOR"
104 PRINT :PRINT"-----------------------------------"CHR$(13)
106 PRINT "      DISK ";DS$;" FILES:"
108 FILES DS$+":*.TMP"
110 REM-----------------------------------------------------------------
112 LOCATE 25,25 : PRINT "OUTPUTING TEMPERATURES TO PRINTER"
114 LPRINT CHR$(10) "    TEMPERATURES IN CELSIUS FOR ";F$  CHR$(10),CHR$(10)
116 FOR J = 1 TO 75
118      LPRINT USING "#######.#";T(J),T(J+75),T(J+150),T(J+225),T(J+300),
                                  T(J+375),T(J+450),T(J+525),T(J+600),T(J+675)
```

```
120 NEXT J
122 LPRINT " ---------------------------- "
124 FOR J = 750 TO 771
126       LPRINT USING "#######.#";T(J),T(J+21)
128 NEXT J
130 LOCATE 25,25 : PRINT "ANY MORE FILES TO BE CONVERTED?(Y/N)"
132 GOSUB 138 : IF A$ ="N" OR A$ ="n" THEN STOP
134 CLEAR : RESTORE
136 GOTO 16
138 REM ------------------------------------------------------------------
140 A$ = INKEY$ : IF A$ = "" THEN 140
142 RETURN
144 REM ------------------------------------------------------------------
146 CLS : LOCATE 8,1
148 PRINT "This program is used for converting retrieved Nicolet data into tempe
ratures."
150 PRINT "You should have files on a disk which where created by the RETREIVE.B
AS"
152 PRINT "program.  Insert this disk in one drive.  Insert another formated dis
k in"
154 PRINT "the other drive for the temperature files to be stored on.  This prog
ram"
156 PRINT "assumes you have used a thermal couple and an isolation amplifier.  S
o you"
158 PRINT "must know the thermal couple type and the amplifier constant to use t
his program."
160 LOCATE 25,30 : PRINT "PRESS ANY KEY"
162 A$ = INKEY$ : IF A$ = "" THEN 162
164 RETURN
165 REM ***************** THERMAL COUPLE DATA ************************************
166 REM ********** TYPE R DATA
168 DATA .263632917,179075.491,-48840341.37,1.90002D10,-4.82704D12,7.6209D14,-7.
20026D16,3.71496D18,-8.03104D19,0.0
170 REM ********** TYPE K DATA
172 DATA .226584602,24152.109,67233.4248,2210340.682,-860963914.9,4.83506D10,-1.
18452D12,1.3869D13,-6.33708D13,0.0
174 REM ********** TYPE T DATA
176 DATA .100860910,25727.94369,-767345.8295,78025595.81,-9247486589,6.97688D11,
-2.66192D13,3.94078D14,0.0,0.0
178 REM ********** TYPE E DATA
180 DATA .104967248,17189.45262,-282639.085,12695339.5,-448703084.6,1.10866D10,-
1.76807E11,1.71842D12,-9.19278D12,2.06132D13
182 REM ********** TYPE J DATA
184 DATA -.048868252,19873.14503,-218614.5353,11569199.78,-264917531.4,201844131
4.,0.0,0.0,0.0,0.0
186 REM ********** TYPE S DATA
188 DATA .927763167,169526.515,-31568363.94,8990730663,-1.63565D12,1.88027D14,-1
.37241D16,6.17501D17,-1.56105D19 ,1.69535D20
190 REM ********** TYPE C DATA
```